8-2016

Analytical methods for gravity-assist tour design

Nathan J. Strange
Purdue University

Graduate School Form
30 Updated 12/26/2015

PURDUE UNIVERSITY
GRADUATE SCHOOL
Thesis/Dissertation Acceptance

This is to certify that the thesis/dissertation prepared

By Nathan J. Strange

Entitled

Analytical Methods for Gravity-Assist Tour Design

For the degree of Doctor of Philosophy

Is approved by the final examining committee:

James M. Longuski
Chair

Kathleen C. Howell

William A. Crossley

Ephraim Fischbach

To the best of my knowledge and as understood by the student in the Thesis/Dissertation Agreement, Publication Delay, and Certification Disclaimer (Graduate School Form 32), this thesis/dissertation adheres to the provisions of Purdue University's "Policy of Integrity in Research" and the use of copyright material.

Approved by Major Professor(s): James M. Longuski

Approved by: Weinong Wayne Chen 6/29/2016

Head of the Departmental Graduate Program Date

ANALYTICAL METHODS FOR GRAVITY-ASSIST TOUR DESIGN

A Dissertation

Submitted to the Faculty

of

Purdue University

by

Nathan J. Strange

In Partial Fulfillment of the

Requirements for the Degree

of

Doctor of Philosophy

August 2016

Purdue University

West Lafayette, Indiana

Dedication

To my Dad: for teaching me how to be quiet and absorb the world around me.

To my Mom: for teaching me that I am limited only by my imagination.

To my Wife: for making my dreams and her dreams our dreams.

To my Children: this is what happens when you think it would be cool to be called "Dr. Strange" and none of the people above talk you out of it.

ACKNOWLEDGMENTS

I would like to start by thanking my advisor, Prof. James Longuski for his guidance and mentorship. Prof. Longuski introduced me to this fascinating research topic and gave me the tools to investigate it. I would also like to thank the members of my doctoral committee: Professors Kathleen Howell, William Crossley, and Ephraim Fischbach. I am very grateful for their excellent instruction in the wizarding ways of astrodynamics, optimization, and gravitation.

I have benefited from excellent research collaborations on the topics covered by this dissertation with Brent Buffington, Stefano Campagnola, Ryan Russell, Damon Landau, Aline Zimmer, Nitin Arora, Aron Wolf, John Smith, Andy Heaton, Anastassios Petropoulos, Gene Bonfiglio, Jennie Johannesen, and Jon Sims. They are a fun group of space cadets to know and explore the Solar System with.

The research described in this dissertation was carried out at Purdue University and the Jet Propulsion Laboratory, California Institute of Technology, under contract with the National Aeronautics and Space Administration. It has only been possible because of the stimulating research environment both at JPL and Purdue. Discussions about difficult problems posed by my colleagues at the laboratory have been a great source of inspiration. In particular, discussions with Jan Ludwinski, Jerry Jones, Trina Ray, Candy Hansen, Kim Reh, Tom Spilker, John Elliott, John Brophy, Brian Muirhead, and Brent Sherwood have provided motivation for much of this research.

TABLE OF CONTENTS

Page

LIST OF TABLES

LIST OF FIGURES

NOMENCLATURE

Variables

α	pump angle
α_e	pump angle for v_e
γ	flight path angle
δ	flyby bending angle
ΔV	change in velocity
ζ	incline angle
θ	b-plane angle
η	angle from asc. node $(f + \omega)$
κ	crank angle
λ	right ascension or longitude
μ	gravitational parameter
ξ	twist angle
τ	time wrt periapsis
ϕ	declination or latitude
Ω	longitude of the ascending node
ω	argument of periapsis
a	semi-major axis
B	impact parameter
C_{Tiss}	Tisserand Parameter
E	eccentric anomaly
e	eccentricity
$\mathcal{E}$	two-body specific energy
f	true anomaly
f_∞	true anomaly of asymptote

H	hyperbolic anomaly
h	specific angular momentum
I	inclination wrt cb pole
i	inclination wrt ga-body orbit
J	Jacobi Integral
J_C	Jacobi Constant
K	Kinetic Energy
k_{ei}	exterior (+1) / interior (-1) leveraging switch
k_{io}	inbound (-1) /outbound (+1) switch
L	Lagrangian
L_{enc}	longitude of encounter
L_m	rev number of maneuver
M	integer number of spacecraft orbits
M_a	number of spacecraft apoapses
N	number of ga-body orbits
N_a	N counted by crossing s/c line of apsides
N_e	N counted by crossing s/c L_{enc}
p	semi-latus rectum
r	distance from center of body
r_a	apoapsis radius wrt central body
r_{asc}	radius of asc. node crossing wrt cb
r_{dsc}	radius of desc. node crossing wrt cb
r_{enc}	radius wrt central body at encounter
r_{la}	radius of leveraging apse wrt cb
r_p	periapsis radius wrt central body
r_{pfb}	periapsis radius wrt ga-body
R_S	Saturn radius, 60330 km.
r_{va}	radius of vacant apse wrt cb
r_{vac}	radius of vacant node crossing wrt cb

s	non-dimensional radius
T	orbit period
T_c	circular orbit period at r_{enc}
t	time
tof	time of flight between encounters
U	potential energy
v	velocity
v_∞	hyperbolic excess velocity wrt ga-body
v_a	velocity at apoapsis wrt cb
v_c	circular velocity wrt cb at r_{enc}
v_e	local escape velocity wrt cb
v_i	hyperbolic excess velocity wrt cb
v_p	velocity at periapsis wrt cb
v_{pfb}	velocity at periapsis wrt ga-body
y	non-dimensional time offset
Subscripts / Superscripts	
x'	x before flyby or maneuver
x''	x after flyby or maneuver
x_{cb}	x pertains to central body
x_{enc}	x for spacecraft orbit wrt central body *at encounter*
x_{fb}	x for spacecraft orbit wrt gravity-assist body
x_{ga}	x for gravity-assist body orbit wrt central body
x_{IO}	pertains to Inbound to Outbound transfer
x_{OI}	pertains to Outbound to Inbound transfer
x_{sc}	x for spacecraft orbit wrt central body
Vectors	
$\vec{x}$	a vector
$\hat{x}$	a unit vector
x	a vector magnitude

ABSTRACT

Strange, Nathan J. Ph.D., Purdue University, August 2016. Analytical Methods for Gravity-Assist Tour Design. Major Professor: James M. Longuski.

This dissertation develops analytical methods for the design of gravity-assist spacecraft trajectories. Such trajectories are commonly employed by planetary science missions to reach Mercury or the Outer Planets. They may also be used at the Outer Planets for the design of science tours with multiple flybys of those planets' moons. Recent work has also shown applicability to new missions concepts such as NASA's Asteroid Redirect Mission.

This work is based in the theory of patched conics. This document applies rigor to the concept of pumping (i.e. using gravity assists to change orbital energy) and cranking (i.e. using gravity assists to change inclination) to develop several analytic relations with pump and crank angles. In addition, transformations are developed between pump angle, crank angle, and v-infinity magnitude to classical orbit elements. These transformations are then used to describe the the limits on orbits achievable via gravity assists of a planet or moon. This is then extended to develop analytic relations for all possible ballistic gravity-assist transfers and one type of propulsive transfer, v-infinity leveraging transfers.

The results in this dissertation complement existing numerical methods for the design of these trajectories by providing methods that can guide numerical searches to find promising trajectories and even, in some cases, replace numerical searches altogether. In addition, results from new techniques presented in this dissertation such as Tisserand Graphs, the V-Infinity Globe, and Non-Tangent V-Infinty Leveraging provide additional insight into the structure of the gravity-assist trajectory design problem.

CHAPTER 1. INTRODUCTION

The technique of gravity-assists has been employed with great success in missions such as Galileo, Cassini, Dawn, and the Voyagers. Since Mariner 10 flew the first gravity-assist tour between two planets, improvements to computer technology have reduced the time needed to find trajectories, and this has enabled ever more complex designs. However, each new mission concept raises the bar for new science in future missions, and these new missions often demand more complex designs than can be enable by increased computer performance alone.

Gravity-assist trajectories are typically found using time-consuming, broad numerical searches across the billions to trillions of combinations of gravity-assist flybys that could constitute a gravity-assist tour. However, due to the numerical nature of these searches, it is still all too easy for a search to step over a promising trajectory. Because of this, a trajectory analyst is never really sure if a given mission's objective cannot be achieved or if the search just missed the solution, and, consequently, it is often unclear when a mission concept being considered is actually infeasible or just one more all-nighter away from working.

The analytical gravity-assist design techniques in this dissertation offer new tests of the feasibility or infeasibility of a given trajectory concept. These techniques can also be used to guide numerical techniques to find the promising trajectories. Such methods may allow trajectory analysts to both work more efficiently and produce better designs.

Several techniques from this research have been applied with great success in the design of both Cassini extended missions, the Europa Orbiter and Europa Clipper studies, the Titan Saturn System Mission (TSSM) study, the Enceladus Life Finder (ELF) mission concept, and the identification of candidate asteroids for the Asteroid Redirect Mission concept.

1.1 Approach and Terminology

Trajectory design for early planetary missions relied heavily on analytical methods and approximations as the computer technology in the 1960s and 1970s made high-fidelity numerical simulations cumbersome and broad searches infeasible. As computer technology advanced, trajectory designers began adding higher fidelity force models earlier into the design process. In the 1990s, computer technology enabled a transition from just accounting for complex force models in numerical simulations to the ability to exploit those models to improve the mission design. Missions such as Genesis and Dawn would not have been possible without this improvement in computer capability and also the associated improvements to numerical methods for trajectory design.

Today, we no longer need to rely on analytical methods to fit a problem within the capabilities of our computers. Full force model equations of motion for a spacecraft can be readily integrated with even the most basic modern computer. Therefore, instead of using analytical methods to replace high fidelity simulations, they are most useful in guiding these simulations and in helping to give one insight into a trajectory design problem.

In this dissertation, the first goal in making simplifying assumptions will be to develop methods independent of body ephemerides and any particular epoch wherever possible. Next, the focus will be to make the methods independent of the orbit orientation where possible. To help meet both of these goals, we may assume that the gravity-assist bodies used in a tour are in circular orbits and mutually coplanar. All of the major planets are in roughly coplanar orbits, and every planet except Mercury is in an approximately circular orbit. All of the planetary moons larger than Saturn's Hyperion (average diameter of 270 km) are in nearly circular orbits, and, with the exception Saturn's Iapetus, all moons larger than Neptune's Nereid (average diameter 340 km) are in mutually coplanar orbits.

A close encounter of a planet or moon that modifies a spacecraft trajectory will be referred to as a *gravity assist*. The planet or moon in this flyby will be called a *gravity-assist body*. The Sun or planet that the gravity-assist body orbits will be called the *central body*. A trajectory that employs multiple gravity assists is a *gravity-assist tour*.

1.2 Historical Background

The theoretical basis for gravity assists and the method of patched conics had its genesis is the work of François Félix Tisserand in 1889 [1–3] when he was studying comets that were passing near to Jupiter. Tisserand had planned to study binary stars, but his new telescope had a defective mount and couldn't be used as he had originally planned. But, fortunately for future astrodynamicists, the mount was stable enough for observations of Jupiter, Saturn, and comets. This led him down the path to discovering an approximation of the Jacobi integral that he used to prove some thought-to-be-newly-discovered comets were actually known comets whose orbits had been perturbed by a Jupiter flyby. This quantity is now called *Tisserand's Parameter* and was key to the early development of gravity-assist spacecraft trajectories [2].

In the early 1960s, Krafft Ehricke [4] and Michael Minovitch, [5] began looking at the concept of using planetary gravity assist for spacecraft trajectories. Although there are earlier examples of the idea of the gravity assist for spacecraft trajectories dating back to the early 1900s [2], Ehricke and Minovitch were the first to introduce the idea to NASA. Later, Gary Flandro [6] was able to use these concepts to design the "Grand Tour" of the Outer Planets that was later flown by the two Voyager spacecraft.

In the 1970s, researchers at JPL began to apply gravity-assist techniques to design tours of planetary moon systems. In 1973, Beckman [7] coined the term orbit *pumping* for using flybys to change orbit energy and orbit *cranking* for using flybys to change inclination. A seminal paper by Uphoff et al. [8] presented several innovative new

techniques that were developed for what would later become the Galileo mission. The later development of the Cassini-Huygens mission to Saturn in the 1990s, provided additional insight into tour design techniques [9, 10].

In the 1990s, new capability for gravity-assist trajectory design was developed at Purdue. Most notably for the research in this dissertation: Williams and Longuski [11–13] investigated using broad numerical searches with the Automated STOUR tour design software for automated tour design, and Sims, Longuski, and Staugler [14] introduced additional theory to describe maneuvers that change flyby v-infinity in gravity-assist tours. This technique is called *V-Infinity Leveraging* (a term first introduced by Longuski) and is explored in Chapter 4.

1.3 New Work in This Dissertation

This section provides an overview of this document highlighting new results.

Chapter 2: V-Infinity Relations

This chapter builds upon the work of Uphoff et al. [8] to more formally define pump and crank angles. This then allows relations in § 2.1.4 and § 2.3 for transforming between pump/crank and classical orbit elements. Section 2.5.4 then provides relations that describe how flybys can cause changes in pump and crank.

The v-infinity magnitude relations in this chapter were first presented in a conference paper by Strange and Sims in 2001, [15] and the pump and crank angle definition and relations (including § 2.1.4, § 2.3, and § 2.5.4) were first presented by Strange at a JPL seminar [16] in 2006.

Chapter 3: Ballistic Gravity-Assist Transfers

This chapter applies the relations from Chapter 2 to develop new relations and techniques to describe the various ballistic gravity-assist transfers identified by Uphoff

et al. [8] The formulae for finding non-resonant and backflip same-body transfers in § 3.1.2 and § 3.1.3 were first presented in conference paper by Strange and Sims [15] in 2001. Equation 3.23 is an especially significant result in this section, as the relationship between v-infinity and inclination for same-body transfers had not been previously identified, and the discovery of this relation has made it significantly easier to numerically converge these transfers. The inclination relation for different body backflips in § 3.2.2 is first presented in this dissertation, but derives from the vacant node relations first presented by Strange in 2003 [17].

The graphical methods presented in this chapter are also new work from this research effort. The Tisserand Graphs in § 3.2.1 were presented in a 2002 journal article by Strange and Longuski [18]. Although a similar method was developed by Labunsky et al. [19] and published in a 1998 book, the Tisserand Graphs were the first application of this kind of graphical method to the gravity-assist pathfinding problem. This graphical method was able to find gravity-assist trajectories that could not be found by numerical searches alone [20]. The V-infinity Globe in § 3.1.4 was first presented in a 2007 conference paper by Strange, Russell, and Buffington [21]. Although previous work had plotted contours of constant orbit period or inclination on the v-infinity sphere, this paper was the first to relate this sphere to pump and crank angles and to plot tour designs on the v-infinity sphere.

Chapter 4: V-Infinity Leveraging

This chapter looks at V-Infinity Leveraging Transfers (VILTs). These transfers change a spacecraft's v_∞ when a gravity assist from another body isn't available to do it for free. A small leveraging maneuver can translate into a change in v_∞ ten or more times larger than the maneuver. As the bending provided by a flyby is a function of the flyby v_∞, leveraging maneuvers provide an economical way to influence the efficacy of a flyby. Previous work [14, 15, 22–24] in VILTs had largely focused on *tangent leveraging*, i.e. leveraging where the v_∞ vector is tangent to the gravity-assist

body's velocity vector at one end of the transfer. This chapter presents work by Strange, Campagnola, and Russell [24, 25] in 2009 that looked at non-tangent VILTs and developed analytic expressions for finding both tangent and non-tangent VILTs. This chapter also includes an example application of this theory to the problem of reducing the orbit insertion ΔV for an Enceladus orbiter or lander mission.

Chapter 5: Asteroid Redirection

This chapter applies the theory developed in Chapters 2 and 3 to the problem of identifying asteroids suitable for redirection into orbits more accessible by human exploration spacecraft or onto Earth-Mars Cyclers. The methods presented in this chapter were used to find the initial asteroid targets for the Asteroid Redirect Mission concept during the initial 2011 study by the Keck Institute for Space Studies (KISS) [26, 27]. This work was presented in 2014 [28] and 2015 [29] conference papers.

Chapter 6: Uranus Tour Design

This chapter addresses the problem of designing the initial inclination reduction sequence for Uranian gravity-assist tours. For most arrival dates, missions to Uranus will have highly inclined ($60^\circ - 80^\circ$) initial capture orbits. This high inclination causes tours to begin with high v-infinity relative to the satellites ($5 - 8$ km/s), which makes design of a gravity-assist tour with the relatively small Uranian moons difficult. This chapter examines using an apo-twist maneuver [30–32] on the initial capture orbit in concert with using multiple flybys to change inclination. It then identifies the best combination of flybys and maneuvers to reduce this inclination in a given length of time. This work was presented in a conference paper in 2013 [33].

CHAPTER 2. V-INFINITY RELATIONS

This chapter will develop analytic relations that will be used in subsequent chapters. The goal in these derivations will be to choose simplifying assumptions where possible so as to facilitate trade space exploration when designing a mission that employs gravity assists. After these relations are used to identify the most promising regions of the trade space, numerical methods can be used both to assess the validity of these simplifying assumptions and to generate a high-fidelity solution with the appropriate force model.

The starting simplification for this analysis is to model a gravity-assist trajectory as a sequence of zero-sphere-of-influence patched conics. That is, flyby trajectories will be modeled as two-body hyperbolic orbits of the gravity-assist body, and the trajectories relative to the central body will be modeled as two-body Keplerian orbits with instantaneous impulses at the flybys. Relative to the central body, the trajectory will be assumed to go through the center of the gravity-assist body, and relative to the gravity-assist body the trajectories will be assumed to come from and go to infinity.

When looking at the orbit elements in these two different reference frames, subscripts (as described in the notation section) will be used to distinguish between qualities taken in different reference frames. The *cb* subscript will describe a quality pertinent to the central body, the *ga* subscript will describe a quality pertinent to the gravity-assist body, the *sc* subscript will denote a quantity describing the patched-conic approximated spacecraft orbit relative to the central body, and the *fb* subscript will denote a quantity describing the patched-conic approximated spacecraft orbit relative to the gravity-assist body.

In the patched-conic assumption, the spacecraft's velocity relative the central body ($\vec{v}_{sc}$) before or after a flyby is given by the vector sum of the gravity-assist body

velocity ($\vec{v}_{ga}$) and the spacecraft's v-infinity ($\vec{v}_{\infty}$) with respect to the gravity-assist body. This sum is shown both in Eqn. 2.1 and Fig. 2.1.

$$\vec{v}_{sc} = \vec{v}_{ga} + \vec{v}_{\infty} \tag{2.1}$$

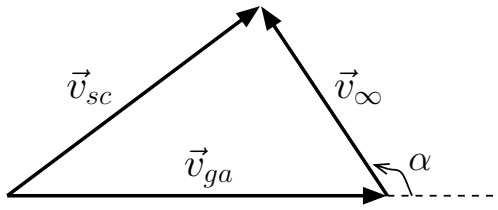

Figure 2.1: Gravity-assist vector diagram

The patched-conic model treats the gravity assist as an instantaneous rotation of the $\vec{v}_{\infty}$ vector. A flyby cannot change the $\vec{v}_{\infty}$ magnitude, only its direction. This provides an important constraint that we may understand better if we represent the $\vec{v}_{\infty}$ in polar coordinates with the pump (α) and crank (κ) angles (described below) that describe the possible rotations of the $\vec{v}_{\infty}$ vector.

We may also use Fig. 2.1 to map a given $\vec{v}_{\infty}$ to an orbit relative to the central body, and can then understand how a flyby may be used to change that orbit. To understand how much change a given flyby may impart, we use the bending angle (δ) to quanitfy how much rotation may be accomplished by a single flyby. We may then both describe constraints on the sorts of orbits relative the central body that could be achieved from multiple flybys and design sequences of flybys to achieve any allowable orbit transformation.

2.1 The V-Infinity Vector

Many of the relations in this chapter will derive from the $\vec{v}_{\infty}$ vector as expressed in Fig. 2.1. The following section develops many of these relations and will allow us to map a given $\vec{v}_{\infty}$ to the related orbit relative to the central body.

2.1.1 Pump Angle

The α angle from Fig. 2.1 is referred to as the the *pump angle* and describes the energy of the spacecraft relative to the central body. We may apply the law of cosines to Fig. 2.1 to develop the following relation between the pump angle to the velocity magnitudes:

$$v_{sc}^2 = v_\infty^2 + v_{ga}^2 + 2v_\infty v_{ga}\cos(\alpha) \tag{2.2}$$

The pump angle is strictly positive, so Eqn. 2.2 fully defines it.

Notice, since we know v_{ga} from the ephemeris of the gravity-assist body, that v_{sc} is a function of v_∞ and α. *Vis viva* then relates v_{sc} directly to a_{sc} (or v_i, the v-infinity with respect to the central body for a hyperbolic orbit):

$$v_{sc}^2 = \mu_{cb}\left(\frac{2}{r_{enc}} - \frac{1}{a_{sc}}\right) \tag{2.3}$$

$$v_{sc}^2 = \frac{2\mu_{cb}}{r_{enc}} + v_i^2 \tag{2.4}$$

Here r_{enc} is the "radius of encounter", the distance from the gravity-assist body to the central body at the time of the flyby. These equations can be written in form suggestive of canonical units (i.e., a non-dimensionalization where μ_{cb} and r_{enc} are both one) by dividing by the square of the local circular velocity (v_c):

$$\left(\frac{v_{sc}}{v_c}\right)^2 = 2 - \frac{r_{enc}}{a_{sc}} \tag{2.5}$$

$$\left(\frac{v_{sc}}{v_c}\right)^2 = 2 + \left(\frac{v_i}{v_c}\right)^2 \tag{2.6}$$

where v_c is given by:

$$v_c = \sqrt{\frac{\mu_{cb}}{r_{enc}}} \tag{2.7}$$

and could be set equal to one for canonical units.

This then allows us to write a_{sc} in canonical form as:

$$\frac{r_{enc}}{a_{sc}} = 2 - \frac{1}{v_c^2}\left[v_\infty^2 + v_{ga}^2 + 2v_\infty v_{ga}\cos(\alpha)\right] \tag{2.8}$$

Since $\pi \geq \alpha \geq 0$, we may bound a_{sc} for all achievable orbits with a given v_∞:

$$2 - \frac{1}{v_c^2}\left[v_\infty^2 + v_{ga}^2 - 2v_\infty v_{ga}\right] \leq \frac{r_{enc}}{a_{sc}} \leq 2 - \frac{1}{v_c^2}\left[v_\infty^2 + v_{ga}^2 + 2v_\infty v_{ga}\right] \tag{2.9}$$

For elliptical and circular orbits, the semi-major axis is directly related to the orbit period (for an ellipse) by Kepler's third law:

$$a_{sc}^3 = \mu_{cb}\left(\frac{T_{sc}}{2\pi}\right)^2 \tag{2.10}$$

Which we may also re-write in canonical form using the local circular orbit period (T_c) to:

$$\left(\frac{a_{sc}}{r_{enc}}\right)^3 = \left(\frac{T_{sc}}{T_c}\right)^2 \tag{2.11}$$

where T_c is given by:

$$T_c = 2\pi\sqrt{\frac{r_{enc}^3}{\mu_{cb}}} \tag{2.12}$$

and would be simply 2π in canonical units. This then allows us to write:

$$\frac{T_{sc}}{T_c} = \left(2 - \frac{1}{v_c^2}\left[v_\infty^2 + v_{ga}^2 + 2v_\infty v_{ga}\cos(\alpha)\right]\right)^{-\frac{3}{2}} \tag{2.13}$$

So, if we know the v_∞ magnitude, the pump angle gives us the orbit period (or v_i). Since orbit period and semi-major axis are an expression of the orbit energy, α is also a measure of the energy relative to the central body. This relationship is independent of inclination (i_{sc}), i.e. $\vec{v}_{sc}$, can rotate around $\vec{v}_{ga}$ without changing Fig. 2.1 or Eqn. 2.2.

The pump angle also determines whether the spacecraft's orbital velocity is in the same direction as the gravity-assist body's orbit or not. The following sections will define spacecraft orbit parameters in reference to the gravity-assist body's orbit. Therefore, the term *prograde* would denote $\vec{v}_{sc}$ in the same direction as the gravity-asist body's orbital motion[1] and *retrograde* the opposite direction. By inspection from Fig. 2.1:

$$\text{if prograde:} \quad v_{ga} > -v_\infty \cos(\alpha) \tag{2.14}$$

$$\text{if retrograde:} \quad v_{ga} < -v_\infty \cos(\alpha) \tag{2.15}$$

When $v_{ga} = v_\infty \cos(\alpha)$ the spacecraft orbit is rectilinear and neither prograde nor retrograde as it is headed on a straight line either away from or towards the central body.

2.1.2 Crank Angle

In order to understand how orbit inclination is related to the direction of the $\vec{v}_\infty$, we need to introduce the other angle from our set of spherical coordinates, crank (κ). The *crank angle* is a measure of the rotation of the plane described by the triangle of $\vec{v}_{sc}$, $\vec{v}_{ga}$, and $\vec{v}_\infty$. I.e., the crank angle is the rotation of Fig. 2.1 relative to the plane of the gravity-assist body's orbit. The crank angle and it's relation to this v-infinity triangle is illustrated in Fig. 2.2. Here we see that the pump and crank angles are sufficient to describe the sphere of possible $\vec{v}_\infty$ directions.

[1]For gravity-assist tours using Neptune's moon Triton, this definition means that a "prograde" orbit would be retrograde with respect to Neptune's pole.

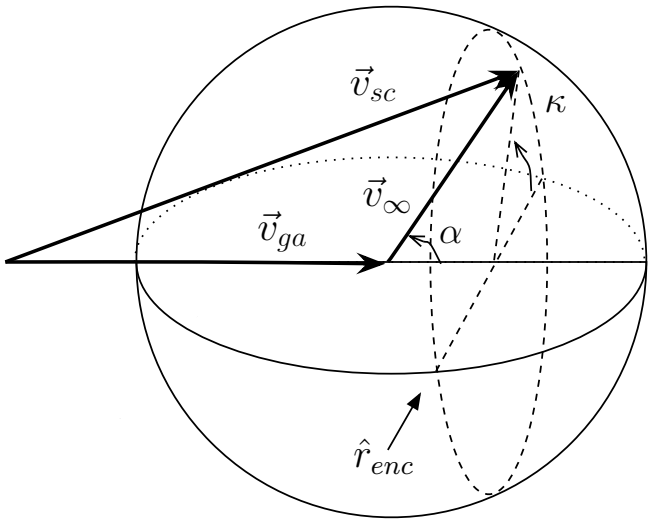

Figure 2.2: v_∞ sphere showing crank and pump angles

First, let's define a reference frame from the gravity-assist body's orbit tied to the direction of $\vec{v}_{ga}$, the $\hat{q}_i$-frame[2] as follows:

$$\hat{q}_3 = \hat{v}_{ga} \tag{2.16}$$

$$\hat{q}_2 = \hat{v}_{ga} \times \hat{r}_{enc} \tag{2.17}$$

$$\hat{q}_1 = \hat{q}_2 \times \hat{q}_3 \tag{2.18}$$

Next we define the $\hat{c}_i$-frame which is tied to the plane of Fig. 2.1, with $\hat{c}_2$ in the same direction as $\hat{q}_2$:

$$\hat{c}_3 = \hat{v}_{ga} \tag{2.19}$$

$$\hat{c}_2 = \hat{v}_{ga} \times \hat{v}_{sc} \tag{2.20}$$

$$\hat{c}_1 = \hat{c}_2 \times \hat{c}_3 \tag{2.21}$$

Then, as in Fig. 2.3, we define the crank angle (κ) as the angle from $\hat{q}_1$ to $\hat{c}_1$. This results in the following transformation between the $\hat{q}_i$ and $\hat{c}_i$ frames:

[2]By the convention in the notation section, $\hat{v}_{ga}$ is a unit vector in the direction of $\vec{v}_{ga}$.

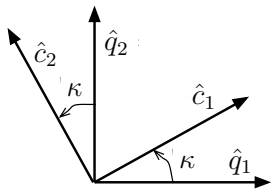

Figure 2.3: $\hat{q}_i \leftrightarrow \hat{c}_i$

$$\hat{q}_1 = \cos(\kappa)\hat{c}_1 - \sin(\kappa)\hat{c}_2 \tag{2.22}$$

$$\hat{q}_2 = \sin(\kappa)\hat{c}_1 + \cos(\kappa)\hat{c}_2 \tag{2.23}$$

$$\hat{c}_1 = \cos(\kappa)\hat{q}_1 + \sin(\kappa)\hat{q}_2 \tag{2.24}$$

$$\hat{c}_2 = -\sin(\kappa)\hat{q}_1 + \cos(\kappa)\hat{q}_2 \tag{2.25}$$

$$\hat{c}_3 = \hat{q}_3 \tag{2.26}$$

In the $\hat{c}_i$-frame it is straightforward to write the components of $\vec{v}_\infty$ from Fig. 2.1:

$$\vec{v}_\infty = v_\infty \sin(\alpha)\hat{c}_1 + v_\infty \cos(\alpha)\hat{c}_3 \tag{2.27}$$

Which, in the $\hat{q}_i$-frame is then:

$$\vec{v}_\infty = v_\infty \sin(\alpha)\cos(\kappa)\hat{q}_1 + v_\infty \sin(\alpha)\sin(\kappa)\hat{q}_2 + v_\infty \cos(\alpha)\hat{q}_3 \tag{2.28}$$

To get to inclination from here, we will need to write the components of $\vec{v}_{sc}$ and then use Eqn. 2.1 to write another equation for $\vec{v}_\infty$. To that end, we need to introduce two additional reference frames tied to the position vector at the flyby ($\vec{r}_{enc}$): a $\hat{p}_i$-

frame in the gravity-assist body's orbit plane, and a $\hat{s}_i$-frame in the spacecraft's orbit plane.

$$\hat{p}_1 = \hat{r}_{enc} \tag{2.29}$$

$$\hat{p}_3 = \hat{r}_{enc} \times \hat{v}_{ga} \tag{2.30}$$

$$\hat{p}_2 = \hat{p}_3 \times \hat{p}_1 \tag{2.31}$$

$$\hat{s}_1 = \hat{r}_{enc} \tag{2.32}$$

$$\hat{s}_3 = \hat{r}_{enc} \times \hat{v}_{sc} \tag{2.33}$$

$$\hat{s}_2 = \hat{s}_3 \times \hat{s}_1 \tag{2.34}$$

Then, at the time of the flyby, the location of both the spacecraft and the gravity assist body with respect to the central body can now be described as:

$$\vec{r}_{enc} = r_{enc}\hat{s}_1 = r_{enc}\hat{p}_1 \tag{2.35}$$

and we get the following conversions between these reference frames:

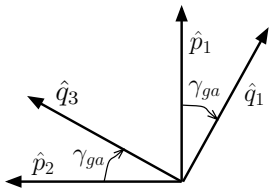

Figure 2.4: $\hat{p}_i \leftrightarrow \hat{q}_i$

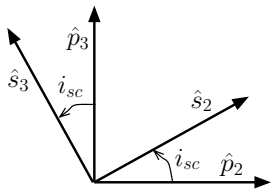

Figure 2.5: $\hat{p}_i \leftrightarrow \hat{s}_i$

$$\hat{p}_1 = \cos(\gamma_{ga})\hat{q}_1 + \sin(\gamma_{ga})\hat{q}_3 \tag{2.36}$$

$$\hat{p}_2 = -\sin(\gamma_{ga})\hat{q}_1 + \cos(\gamma_{ga})\hat{q}_3 \tag{2.37}$$

$$\hat{p}_3 = \hat{q}_2 \tag{2.38}$$

$$\hat{q}_1 = \cos(\gamma_{ga})\hat{p}_1 - \sin(\gamma_{ga})\hat{p}_2 \tag{2.39}$$

$$\hat{q}_3 = \sin(\gamma_{ga})\hat{p}_1 + \cos(\gamma_{ga})\hat{p}_2 \tag{2.40}$$

$$\hat{p}_1 = \hat{s}_1 \tag{2.41}$$

$$\hat{p}_2 = \cos(i_{sc})\hat{s}_2 - \sin(i_{sc})\hat{s}_3 \tag{2.42}$$

$$\hat{p}_3 = \sin(i_{sc})\hat{s}_2 + \cos(i_{sc})\hat{s}_3 \tag{2.43}$$

$$\hat{s}_2 = \cos(i_{sc})\hat{p}_2 + \sin(i_{sc})\hat{p}_3 \tag{2.44}$$

$$\hat{s}_3 = -\sin(i_{sc})\hat{p}_2 + \cos(i_{sc})\hat{p}_3 \tag{2.45}$$

Note that the above transformations have defined the inclination as the angle between the spacecraft orbit and the plane of the gravity-assist body's orbit. (If inclination in another coordinate system is desired, additional transformations would be needed.) In addition, although inclination is traditionally defined as a strictly positive angle, the transformations above require inclination to allow negative values. Both of these assumptions were not made merely to simplify the above transformations, but because they allow useful insight into geometric restrictions on the spacecraft orbit that will be discussed in § 2.2.1.

Now we write each velocity vector from Fig. 2.1 in the $\hat{p}_i$-frame:

$$\begin{aligned}\vec{v}_{ga} &= v_{ga}\hat{q}_3 \\ &= v_{ga}\sin(\gamma_{ga})\hat{p}_1 + v_{ga}\cos(\gamma_{ga})\hat{p}_2\end{aligned} \tag{2.46}$$

$$\begin{aligned}\vec{v}_{sc} &= v_{sc}\sin(\gamma_{sc})\hat{s}_1 + v_{sc}\cos(\gamma_{sc})\hat{s}_2 \\ &= v_{sc}\sin(\gamma_{sc})\hat{p}_1 + v_{sc}\cos(\gamma_{sc})\cos(i_{sc})\hat{p}_2 + v_{sc}\cos(\gamma_{sc})\sin(i_{sc})\hat{p}_3\end{aligned} \tag{2.47}$$

We may write $\vec{v}_\infty$ in the $\hat{p}_i$-frame either from Eqn. 2.1:

$$\begin{aligned}\vec{v}_\infty &= \vec{v}_{sc} - \vec{v}_{ga} \\ &= [v_{sc}\sin(\gamma_{sc}) - v_{ga}\sin(\gamma_{ga})]\hat{p}_1 + [v_{sc}\cos(\gamma_{sc})\cos(i_{sc}) - v_{ga}\cos(\gamma_{ga})]\hat{p}_2 \\ &\quad + v_{sc}\cos(\gamma_{sc})\sin(i_{sc})\hat{p}_3\end{aligned} \tag{2.48}$$

or from Eqn. 2.28:

$$\begin{aligned}\vec{v}_\infty = v_\infty[&\sin(\alpha)\cos(\kappa)\cos(\gamma_{ga}) + \cos(\alpha)\sin(\gamma_{ga})]\hat{p}_1 + v_\infty[\cos(\alpha)\cos(\gamma_{ga}) \\ &- \sin(\alpha)\cos(\kappa)\sin(\gamma_{ga})]\hat{p}_2 + v_\infty\sin(\alpha)\sin(\kappa)\hat{p}_3\end{aligned} \tag{2.49}$$

By combining Eqn. 2.48 and Eqn. 2.49, we get three equations from each of the $\hat{p}_i$:

$$v_{sc}\sin(\gamma_{sc}) - v_{ga}\sin(\gamma_{ga}) = v_\infty\sin(\alpha)\cos(\kappa)\cos(\gamma_{ga}) + v_\infty\cos(\alpha)\sin(\gamma_{ga}) \tag{2.50}$$

$$\begin{aligned}v_{sc}\cos(\gamma_{sc})\cos(i_{sc}) - v_{ga}\cos(\gamma_{ga}) = \\ v_\infty\cos(\alpha)\cos(\gamma_{ga}) - v_\infty\sin(\alpha)\cos(\kappa)\sin(\gamma_{ga})\end{aligned} \tag{2.51}$$

$$v_{sc}\cos(\gamma_{sc})\sin(i_{sc}) = v_\infty\sin(\alpha)\sin(\kappa) \tag{2.52}$$

From Eqn. 2.52:

$$\sin(i_{sc}) = \frac{v_\infty \sin(\alpha)\sin(\kappa)}{v_{sc}\cos(\gamma_{sc})} \tag{2.53}$$

Since pump is strictly positive, i_{sc} will have the same sign as κ if the spacecraft is in a prograde orbit (i.e. $\cos(\gamma_{sc})$ positive) or the opposite sign if the orbit is retrograde.

In the case of $\gamma_{ga} = 0$, Eqn. 2.50 and Eqn. 2.51 simplify to:

$$v_{sc}\sin(\gamma_{sc}) = v_\infty \sin(\alpha)\cos(\kappa) \tag{2.54}$$

$$v_{sc}\cos(\gamma_{sc})\cos(i_{sc}) - v_c = v_\infty \cos(\alpha) \tag{2.55}$$

From Eqn. 2.54:

$$\sin(\gamma_{sc}) = \frac{v_\infty}{v_{sc}} \sin(\alpha)\cos(\kappa) \tag{2.56}$$

$$\cos(\gamma_{sc}) = \frac{1}{v_{sc}} \sqrt{v_{sc}^2 - \left(v_\infty \sin(\alpha)\cos(\kappa)\right)^2} \tag{2.57}$$

Plugging this into Eqn. 2.53 and combining with Eqn. 2.2 yields the following expression relating crank and inclination:

$$\sin(i_{sc}) = \frac{\sin(\alpha)\sin(\kappa)}{\sqrt{\left(\frac{v_c}{v_\infty}\right)^2 + 2\frac{v_c}{v_\infty}\cos(\alpha) + \left(1 - \sin^2(\alpha)\cos^2(\kappa)\right)}} \tag{2.58}$$

Since $0 \leq |i_{sc}| \leq \frac{\pi}{2}$ for prograde orbits and $\frac{\pi}{2} \leq |i_{sc}| \leq \pi$ for retrograde orbits, we know the quadrant of i_{sc} based on whether the orbit is prograde or retrograde.

Equation 2.55 may be combined with Eqn. 2.53 to yield the following convenient expression for converting from inclination to crank:

$$\sin(\kappa) = \tan(i_{sc}) \left(\frac{v_c/v_\infty + \cos(\alpha)}{\sin(\alpha)} \right) \tag{2.59}$$

To resolve quadrant ambiguities above, note from Eqn. 2.54 that $\cos(\kappa)$ is negative for inbound flybys (i.e. $\gamma_{sc} < 0$) and is positive for outbound flybys. Equation 2.59 also shows that inclination and crank have the same sign for prograde orbits and opposite signs for retrograde orbits.

Bounds on Inclination

From Eqn. 2.53, we see that the maximum orbit inclination is achieved when crank is $\pm\pi/2$. Plugging that into Eqn. 2.59, we get the following constraint on the inclinations achievable with gravity assists for a given pump angle and v_∞:

$$|\tan(i_{sc})| \leq \frac{\sin(\alpha)}{v_c/v_\infty + \cos(\alpha)} \tag{2.60}$$

Equation 2.60 is a driving design constraint in cases where a tour must achieve high inclinations for science objectives, such as for the Cassini-Huygens mission, or where tours must start with high inclinations, such as Uranus missions.

2.1.3 V-Infinity Magnitude

To find the v_∞ from the spacecraft orbit, we start with Eqn. 2.48 squared:

$$v_\infty^2 = v_{sc}^2 + v_{ga}^2 - 2v_{sc}v_{ga}[\sin(\gamma_{sc})\sin(\gamma_{ga}) + \cos(\gamma_{sc})\cos(\gamma_{ga})\cos(i_{sc})] \tag{2.61}$$

Orbital angular momentum will give us γ_{sc} for use in Eqn. 2.61. We may write the specific angular momentum by the cross product:

$$\vec{h}_{sc} = \vec{r}_{enc} \times \vec{v}_{sc} = h_{sc}\hat{s}_3 = r_{enc}v_{sc}\cos(\gamma_{sc})\hat{s}_3 \tag{2.62}$$

or from the solution to the two-body problem:

$$h_{sc} = \sqrt{\mu_{cb}a_{sc}(1-e_{sc}^2)} \tag{2.63}$$

Combining Eqn. 2.62 with Eqn. 2.63 gives:

$$\cos(\gamma_{sc}) = \frac{\sqrt{\mu_{cb}a_{sc}(1-e_{sc}^2)}}{r_{enc}v_{sc}} = \frac{v_c}{v_{sc}}\sqrt{\frac{a_{sc}}{r_{enc}}(1-e_{sc}^2)} \tag{2.64}$$

The sign of γ_{sc} in Eqn. 2.64 may be determined by noting whether the flyby occurs before periapsis (i.e. *inbound*) or after periapsis (i.e. *outbound*) of the orbit relative the central body. For inbound flybys $\gamma_{sc} < 0$ and for outbound flybys $\gamma_{sc} > 0$. When $\gamma_{sc} = 0$ the flyby occurs at either periapsis (if $a_{sc} < r_{enc}$) or apoapsis (if $a_{sc} > r_{enc}$).

Now if we set $\gamma_{ga} = 0$ and $v_{ga} = v_c$, we may write Eqn. 2.61 as:

$$\left(\frac{v_\infty}{v_c}\right)^2 = \left(\frac{v_{sc}}{v_c}\right)^2 + 1 - 2\cos(i_{sc})\sqrt{\frac{a_{sc}}{r_{enc}}(1-e_{sc}^2)} \tag{2.65}$$

Now, if we combine with Eqn. 2.5, we get:

$$\left(\frac{v_\infty}{v_c}\right)^2 = 3 - \frac{r_{enc}}{a_{sc}} - 2\cos(i_{sc})\sqrt{\frac{a_{sc}}{r_{enc}}(1-e_{sc}^2)} \tag{2.66}$$

2.1.4 Pump and Crank from Orbit Elements

If we assume the gravity-assist body to be in a circular orbit, Eqn. 2.66 and Eqn. 2.5 yield v_∞ magnitude from a_{sc} and e_{sc}. Then we use Eqn. 2.2 and Eqn. 2.5 to solve for α:

$$\cos(\alpha) = \frac{1}{2}\left[\frac{v_c}{v_\infty}\left(1 - \frac{r_{enc}}{a_{sc}}\right) - \frac{v_\infty}{v_c}\right] \tag{2.67}$$

We then use Eqn. 2.59 for κ:

$$\sin(\kappa) = -\tan(i_{sc})\left(\frac{v_c/v_\infty + \cos(\alpha)}{\sin(\alpha)}\right) \tag{2.68}$$

Since α is strictly positive, there are no quadrant ambiguities to worry about in Eqn. 2.67. In Eqn. 2.68, $-\pi/2 \leq \kappa \leq \pi/2$ for inbound encounters and $\pi/2 \leq \kappa \leq 3\pi/2$ for outbound.

2.2 Orbit Orientation

So far we haven't uncovered any connection between the $\vec{v}_\infty$ and orbit orientation as v_∞, α, and κ depend only on a_{sc}, e_{sc}, and i_{sc} and not on any of the orientation related orbit elements. To find the connections to orbit orientation we must investigate the geometric constraints that arise because the gravity-assist must occur at the intersection of the spacecraft orbit and the gravity-assist body's orbit.

2.2.1 Node Crossings

As discussed in § 2.1.2, the i_{sc} inclination is defined as the angle between the spacecraft orbit and the plane of the gravity-assist body's orbit. This means that the gravity-assist will always be on the spacecraft's line of nodes. One node crossing will be at the encounter with the gravity-assist body, and the other I will call the *vacant*

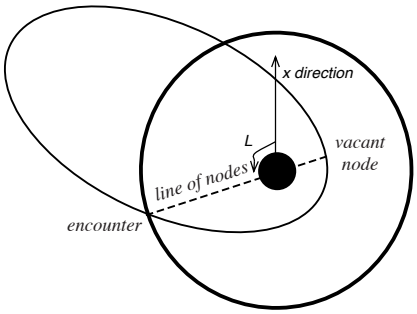

Figure 2.6: Longitude of Encounter

node. By changing the $\vec{v}_\infty$ we can control this vacant node crossing to target other flyby bodies or avoid planetary rings.

Figure 2.6 defines the *longitude of encounter*, L_{enc}, as the angle between the encounter node crossing and some reference direction. If we assume that the gravity-assist body is in a ciricular orbit, then L_{enc} is all the information that we need of the gravity-assist body's position to fully determine the relationship between the spacecraft's orbit and its $\vec{v}_\infty$.

If the spacecraft's longitude of the ascending node, Ω_{sc}, is measured with respect to the same reference direction, the relationship between L_{enc} and Ω_{sc} is simply:

$$\Omega_{sc} = \begin{cases} L_{enc} & \text{if enc. at asc. node} \\ L_{enc} \pm \pi & \text{if enc. at desc. node} \end{cases} \tag{2.69}$$

In Fig. 2.2 we see that for positive values of crank, the $\vec{v}_{sc}$ is rising with respect to the gravity-assist body's orbit, and it is falling for negative crank. Therefore positive crank values correspond to encounters at the ascending node of the spacecraft orbit and negative values correspond to descending node encounters.

The argument of periapsis, as shown in Fig. 2.7, describes the orientation of the spacecraft orbit relative to the line of nodes. Since the flyby is at the node crossing, the true anomaly of the encounter, f_{enc} is given by:

$$f_{enc} = \begin{cases} -\omega_{sc} & \text{if enc. at asc. node} \\ \pi - \omega_{sc} & \text{if enc. at desc. node} \end{cases} \tag{2.70}$$

where ω_{sc} is the argument of periapsis of the spacecraft orbit.

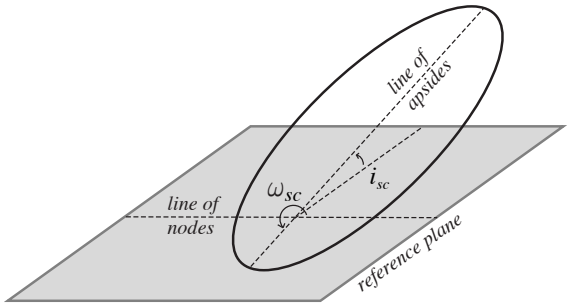

Figure 2.7: Argument of Periapsis

We may then substitute f_{enc} into the conic equation for a two-body orbit:

$$r_{enc} = \frac{a_{sc}(1 - e_{sc}^2)}{1 + e_{sc}\cos(f_{enc})} \tag{2.71}$$

and then combine with Eqn. 2.70:

$$r_{enc} = \frac{a_{sc}(1 - e_{sc}^2)}{1 \pm e_{sc}\cos(\omega_{sc})} \tag{2.72}$$

and then solve for the argument of periapsis:

$$\text{if at ascending node:} \quad \cos(\omega_{sc}) = \frac{1}{e_{sc}}\left[\frac{a_{sc}}{r_{enc}}(1 - e_{sc}^2) - 1\right] \tag{2.73}$$

$$\text{if at descending node:} \quad \cos(\omega_{sc}) = \frac{1}{e_{sc}}\left[1 - \frac{a_{sc}}{r_{enc}}(1 - e_{sc}^2)\right] \tag{2.74}$$

Since f_{enc} will be negative for an inbound flyby and positive outbound and since $\cos(\kappa)$ is also negative for inbound flybys and positive inbound, then:

$$\text{sign}(\omega_{sc}) = \text{sign}(f_{enc}) = \text{sign}(\cos(\kappa)) \tag{2.75}$$

We may also solve the conic equation for the radius of the node crossing opposite the flyby. If we do this with Eqn. 2.73 or Eqn. 2.74 and simplify, we get the following expression for the radius of the vacant node (in canonical form):

$$\frac{r_{vac}}{r_{enc}} = \frac{\frac{a_{sc}}{r_{enc}}(1 - e_{sc}^2)}{2 - \frac{a_{sc}}{r_{enc}}(1 - e_{sc}^2)} \tag{2.76}$$

2.3 How to Solve for Classical Orbit Elements

We can now derive the full set of classical orbit elements from v_∞, α, and κ. The following relations all assume that the gravity-assist body is in a circular orbit. First, from Eqn. 2.8:

$$\frac{r_{enc}}{a_{sc}} = 1 - \frac{v_\infty}{v_c}\left(\frac{v_\infty}{v_c} + 2\cos(\alpha)\right) \tag{2.77}$$

From Eqn. 2.58:

$$\tan(i_{sc}) = \sin(\kappa)\left(\frac{\sin(\alpha)}{v_c/v_\infty + \cos(\alpha)}\right) \tag{2.78}$$

Where:

$$\text{if: } -v_\infty \cos(\alpha) < v_c \implies \text{prograde} \implies |i_{sc}| > \pi/2\,;\, \text{sign}(i_{sc}) = \text{sign}(\kappa)$$
$$\text{if: } -v_\infty \cos(\alpha) > v_c \implies \text{retrograde} \implies |i_{sc}| < \pi/2\,;\, \text{sign}(i_{sc}) = -\text{sign}(\kappa)$$
$$\text{if: } -v_\infty \cos(\alpha) = v_c \implies \text{polar orbit} \implies |i_{sc}| = \pi/2\,;\, \text{sign}(i_{sc}) = \text{sign}(\kappa)$$

From Eqn. 2.66:

$$e_{sc}^2 = 1 - \frac{r_{enc}}{a_{sc}} \left(\frac{3 - \left(\frac{v_\infty}{v_c}\right)^2 - \frac{r_{enc}}{a_{sc}}}{2\cos(i_{sc})} \right)^2 \tag{2.79}$$

From Eqn. 2.73 and Eqn. 2.74:

$$\cos(\omega_{sc}) = \frac{\text{sign}(\kappa)}{e_{sc}} \left[\frac{a_{sc}}{r_{enc}}(1 - e_{sc}^2) - 1 \right] \tag{2.80}$$

From Eqn. 2.71:

$$\cos(f_{enc}) = \frac{1}{e_{sc}} \left[\frac{a_{sc}}{r_{enc}}(1 - e_{sc}^2) - 1 \right] \tag{2.81}$$

where the sign of f_{enc} is the same as ω_{sc}:

$$\text{sign}(\omega_{sc}) = \text{sign}(f_{enc}) = \text{sign}(\cos(\kappa)) \tag{2.82}$$

Then finally, from Eqn. 2.69:

$$\Omega_{sc} = L_{enc} + (1 - \text{sign}(\kappa)) \frac{\pi}{2} \tag{2.83}$$

where L_{enc} is the Longitude of Encounter as defined in § 2.2.1.

2.4 Relationship between Patched Conics and the 3-Body Problem

Equation 2.66, repeated below:

$$\left(\frac{v_\infty}{v_c}\right)^2 = 3 - \frac{r_{enc}}{a_{sc}} - 2\cos(i_{sc})\sqrt{\frac{a_{sc}}{r_{enc}}\left(1 - e_{sc}^2\right)} \tag{2.84}$$

is actually a much more remarkable result than I previously let on. It is a window into the connection between the patched-conic assumption and Circular Restricted 3-Body Problem (CR3BP). This section will illuminate the view through this window.

2.4.1 The Circular Restricted 3-Body Problem

Figure 2.8 depicts the geometry of the CR3BP. Here point **C** is the center of mass of the system and $\vec{r_1} = -r_1\hat{r}$ and $\vec{r_2} = r_2\hat{r}$ describe the position of the bodies m_1 and m_2 relative to the center of mass, where $\hat{r} = \cos(\omega t)\hat{\xi} + \sin(\omega t)\hat{\eta}$. Both bodies are assumed to be in a circular orbit and at a constant distance from each other. The spacecraft, m_3, is assumed to have negligible mass.

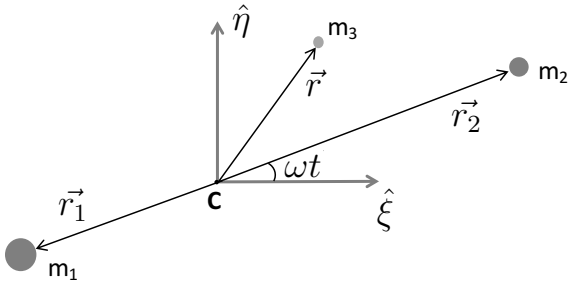

Figure 2.8: The Circular Restricted 3-Body Problem (CR3BP)

I will nondimensionalize the problem by assuming units such that $r_1 + r_2 = 1$ and $\mu_1 + \mu_2 = 1$ (where μ_1 and μ_2 are the masses m_1 and m_2 times Newton's Gravitational Constant). Since $\vec{r_1}$ and $\vec{r_2}$ are with respect to the center of mass:

$$m_1\vec{r_1} + m_2\vec{r_2} = (-m_1r_1 + m_2r_2)\hat{r_2} = 0 = (-\mu_1r_1 + \mu_2r_2)\hat{r_2} \tag{2.85}$$

Noting that $r_2 = 1 - r_1$ and $\mu_1 = 1 - \mu_2$:

$$-\mu_1 r_1 + \mu_2 r_2 = (\mu_2 - 1)r_1 + \mu_2(1 - r_1) = 0 \tag{2.86}$$

When we solve Eqn. 2.86 for r_1, we get:

$$r_1 = \mu_2 = \nu \tag{2.87}$$

Here ν is a parameter that describes both the relative positions and relative masses of the two gravitating bodies.

Finally, note that because we assume the two-bodies are in a circular orbit, this nondimensionalization yields:

$$\omega = \frac{1}{r_1 + r_2}\sqrt{\frac{\mu_1 + \mu_2}{r_1 + r_2}} = 1 \tag{2.88}$$

2.4.2 CR3BP Lagrangian

Consider m_3 in Figure 2.8. First, let's write its position relative to m_1 and m_2 as $\vec{\rho_1}$ and $\vec{\rho_2}$ respectively in terms of the third body's position with respect to the center of mass, $\vec{r}$.

$$\vec{\rho_1} = \vec{r} - \vec{r_1} = (\xi + \nu\cos(\omega t))\hat{\xi} + (\eta + \nu\sin(\omega t))\hat{\eta} + \zeta\hat{\zeta} \tag{2.89}$$

$$\vec{\rho_2} = \vec{r} - \vec{r_2} = (\xi + (\nu - 1)\cos(\omega t))\hat{\xi} + (\eta + (\nu - 1)\sin(\omega t))\hat{\eta} + \zeta\hat{\zeta} \tag{2.90}$$

The magnitudes of $\vec{\rho_1}$ and $\vec{\rho_2}$ are given by:

$$\rho_1^2 = (\xi + \nu\cos t)^2 + (\eta + \nu\sin t)^2 + \zeta^2 \tag{2.91}$$

$$\rho_2^2 = (\xi + (\nu - 1)\cos t)^2 + (\eta + (\nu - 1)\sin t)^2 + \zeta^2 \tag{2.92}$$

Let's now define a rotating reference frame (remember $\hat{r_2}$ is from **C** to m_2):

$$\hat{x} = \hat{r_2} \qquad \hat{z} = \hat{\zeta} \qquad \hat{y} = \hat{z} \times \hat{x} \tag{2.93}$$

The position of m_3 relative the center of mass is then:

$$\vec{r} = x\hat{x} + y\hat{y} + z\hat{z} \tag{2.94}$$

And $\vec{\rho_1}$ and $\vec{\rho_2}$ are:

$$\vec{\rho_1} = (x + \nu)\hat{x} + y\hat{y} + z\hat{z} \tag{2.95}$$

$$\vec{\rho_2} = (x + \nu - 1)\hat{x} + y\hat{y} + z\hat{z} \tag{2.96}$$

with magnitudes:

$$\rho_1^2 = (x + \nu)^2 + y^2 + z^2 \tag{2.97}$$

$$\rho_2^2 = (x + \nu - 1)^2 + y^2 + z^2 \tag{2.98}$$

The specific potential energy, U, of m_3 is:

$$U = -\frac{1 - \nu}{\rho_1} - \frac{\nu}{\rho_2} \tag{2.99}$$

and the specific kinetic energy, K, of m_3 is:

$$K = \frac{1}{2}(\dot{\vec{r_I}} \cdot \dot{\vec{r_I}}) \tag{2.100}$$

and $\dot{\vec{r_I}}$ is the inertial-frame velocity and is given by:

$$\dot{\vec{r_I}} = \dot{\vec{r}} + \vec{\omega} \times \vec{r} = (\dot{x} - y)\hat{x} + (\dot{y} + x)\hat{y} + \dot{z}\hat{z} \tag{2.101}$$

We may then write K as:

$$K = \frac{1}{2}\left[(\dot{x} - y)^2 + (\dot{y} + x)^2 + \dot{z}^2\right] \tag{2.102}$$

The Lagrangian, $L = K - U$, is then:

$$L = \frac{1}{2}\left[(\dot{x} - y)^2 + (\dot{y} + x)^2 + \dot{z}^2\right] + \frac{1-\nu}{\rho_1} + \frac{\nu}{\rho_2} \tag{2.103}$$

We can now get the equations of motion from the Euler-Lagrange equation:

$$\frac{\partial L}{\partial q_i} = \frac{d}{dt}\frac{\partial L}{\partial \dot{q}_i} \tag{2.104}$$

We start with the $\frac{\partial L}{\partial q_i}$:

$$\frac{\partial L}{\partial x} = (\dot{y} + x) - \frac{1-\nu}{\rho_1^3}(x + \nu) - \frac{\nu}{\rho_2^3}(x + \nu - 1) \tag{2.105}$$

$$\frac{\partial L}{\partial y} = -(\dot{x} - y) - \frac{1-\nu}{\rho_1^3}y - \frac{\nu}{\rho_2^3}y \tag{2.106}$$

$$\frac{\partial L}{\partial z} = -\frac{1-\nu}{\rho_1^3}z - \frac{\nu}{\rho_2^3}z \tag{2.107}$$

The $\frac{d}{dt}\frac{\partial L}{\partial \dot{q}_i}$ are then:

$$\frac{d}{dt}\frac{\partial L}{\partial \dot{x}} = \frac{d}{dt}(\dot{x} - y) = \ddot{x} - \dot{y} \tag{2.108}$$

$$\frac{d}{dt}\frac{\partial L}{\partial \dot{y}} = \frac{d}{dt}(\dot{y} + x) = \ddot{y} + \dot{x} \tag{2.109}$$

$$\frac{d}{dt}\frac{\partial L}{\partial \dot{z}} = \frac{d}{dt}\dot{z} = \ddot{z} \tag{2.110}$$

So the equations of motion in the rotating frame are:

$$\ddot{x} = 2\dot{y} + x - \frac{1-\nu}{\rho_1^3}(x+\nu) - \frac{\nu}{\rho_2^3}(x+\nu-1) \tag{2.111}$$

$$\ddot{y} = -2\dot{x} + y - y\frac{1-\nu}{\rho_1^3} - y\frac{\nu}{\rho_2^3} \tag{2.112}$$

$$\ddot{z} = -z\frac{1-\nu}{\rho_1^3} - z\frac{\nu}{\rho_2^3} \tag{2.113}$$

2.4.3 CR3BP Jacobi Integral

I will use the form of the Jacobi Integral given by:

$$J = \frac{\partial L}{\partial \dot{\vec{q}}} \cdot \dot{\vec{q}} - L \tag{2.114}$$

For the Lagrangian in Eqn. 2.103 the Jacobi Integral is:

$$J = (\dot{x} - y)\dot{x} + (\dot{y} + x)\dot{y} + \dot{z}^2 - \frac{1}{2}\left[(\dot{x} - y)^2 + (\dot{y} + x)^2 + \dot{z}^2\right] - \frac{1-\nu}{\rho_1} - \frac{\nu}{\rho_2} \tag{2.115}$$

$$J = \frac{1}{2}\left[(\dot{x} - y)(\dot{x} + y) + (\dot{y} + x)(\dot{y} - x) + \dot{z}^2\right] - \frac{1-\nu}{\rho_1} - \frac{\nu}{\rho_2} \tag{2.116}$$

$$J = \frac{1}{2}\left(\dot{x}^2 + \dot{y}^2 + \dot{z}^2 - x^2 - y^2\right) - \frac{1-\nu}{\rho_1} - \frac{\nu}{\rho_2} \tag{2.117}$$

Or, in terms $\vec{r_I}$ from Eqn. 2.101:

$$J = \frac{1}{2}\left(\dot{\vec{r_I}} \cdot \dot{\vec{r_I}}\right) - x^2 - y^2 - \dot{x}y + x\dot{y} - \frac{1-\nu}{\rho_1} - \frac{\nu}{\rho_2} \tag{2.118}$$

Note that:

$$\left(\vec{r_I} \times \dot{\vec{r_I}}\right) \cdot \hat{z} = x^2 + y^2 + \dot{x}y - x\dot{y} \tag{2.119}$$

So:

$$J = \frac{1}{2}\left(\dot{\vec{r_I}} \cdot \dot{\vec{r_I}}\right) - \left(\vec{r_I} \times \dot{\vec{r_I}}\right) \cdot \hat{z} - \frac{1-\nu}{\rho_1} - \frac{\nu}{\rho_2} \tag{2.120}$$

2.4.4 Jacobi Constant

The time derivative of Eqn. 2.117 is:

$$\dot{J} = \dot{x}\ddot{x} + \dot{y}\ddot{y} + \dot{z}\ddot{z} - x\dot{x} - y\dot{y} + \frac{1-\nu}{\rho_1^3}\left[(x+\nu)\dot{x} + y\dot{y} + z\dot{z}\right] + \frac{\nu}{\rho_2^3}\left[(x+\nu-1)\dot{x} + y\dot{y} + z\dot{z}\right] \tag{2.121}$$

$$\dot{J} = \dot{x}\left(\ddot{x} - x + \frac{1-\nu}{\rho_1^3}(x+\nu) + \frac{\nu}{\rho_2^3}(x+\nu-1)\right) + \dot{y}\left(\ddot{y} - y + y\frac{1-\nu}{\rho_1^3} + y\frac{\nu}{\rho_2^3}\right) + \dot{z}\left(\ddot{z} + z\frac{1-\nu}{\rho_1^3} + z\frac{\nu}{\rho_2^3}\right) \tag{2.122}$$

If we substitute the equations of motion from Eqn. 2.111, Eqn. 2.112, and Eqn. 2.113 in to the above, we get:

$$\dot{J} = \dot{x}(2\dot{y}) + \dot{y}(-2\dot{x}) = 0 \tag{2.123}$$

Therefore the Jacobi Integral is constant for the CR3BP. And since it is constant, we may define the *Jacobi Constant* as $-2J$ from Eqn. 2.120:

$$J_C = 2\left(\frac{1-\nu}{\rho_1} + \frac{\nu}{\rho_2}\right) + 2\left(\vec{r_I} \times \dot{\vec{r_I}}\right) \cdot \hat{z} - \left(\dot{\vec{r_I}} \cdot \dot{\vec{r_I}}\right) \tag{2.124}$$

2.4.5 The Tisserand Invariant

Let's assume the m_3 is at a point in its trajectory that is far enough from m_2 that its orbit may be approximated by an instantaneous two-body orbit of m_1. In that

case, we may apply: Eqn. 2.5, which with our current nondimemsionalization (i.e. $r_{enc} = 1$) is:

$$\dot{\vec{r_I}} \cdot \dot{\vec{r_I}} = 2 - \frac{1}{a} \tag{2.125}$$

also, from angular momentum:

$$\vec{r_I} \times \dot{\vec{r_I}} = \sqrt{a(1-e^2)}\hat{s}_3 \tag{2.126}$$

or, since $\hat{z} = \hat{q}_3$:

$$\left(\vec{r_I} \times \dot{\vec{r_I}}\right) \cdot \hat{z} = \cos(i_{sc})\sqrt{a(1-e^2)}\hat{z} \tag{2.127}$$

Now if we substitute into Eqn. 2.124:

$$J_C = 2\left(\frac{1-\nu}{\rho_1} + \frac{\nu}{\rho_2} - 1\right) + \frac{1}{a} + 2\cos(i_{sc})\sqrt{a(1-e^2)} \tag{2.128}$$

Now if we assume that m_1 is very close to the center of mass, i.e. $\nu \approx 0$, and that $\rho_1 \approx r_{enc} = 1$:

$$J_C \approx \frac{1}{a} + 2\cos(i_{sc})\sqrt{a(1-e^2)} \tag{2.129}$$

This approximation of the Jacobi Constant is the *Tisserand's Parameter*, and if we return to using units, it takes this form:

$$C_{Tiss} = \frac{r_{enc}}{a_{sc}} + 2\cos(i_{sc})\sqrt{\frac{a_{sc}}{r_{enc}}(1-e_{sc}^2)} \tag{2.130}$$

and now we can see the connection to Eqn. 2.84. Tisserand's Parameter is related to v_∞:

$$C_{Tiss} = 3 - \left(\frac{v_\infty}{v_c}\right)^2 \tag{2.131}$$

or in terms of Jacobi's Constant:

$$J_C \approx 3 - \left(\frac{v_\infty}{v_c}\right)^2 \tag{2.132}$$

2.5 How Flybys Change $\vec{v}_\infty$

So far we've done a lot of work relating the orbit of the central body to the $\vec{v}_\infty$. Now it is time to look at the orbit relative to the flyby body and how flybys change the $\vec{v}_\infty$ and the central-body orbit.

2.5.1 Bending Angle

Figure 2.9 shows the flyby hyperbola and the change in the $\vec{v}_\infty$ direction. Here $\vec{v}'_\infty$ is the $\vec{v}_\infty$ before the flyby and $\vec{v}''_\infty$ is after the flyby. The angle between $\vec{v}'_\infty$ and $\vec{v}''_\infty$ is the *bending angle*, δ.

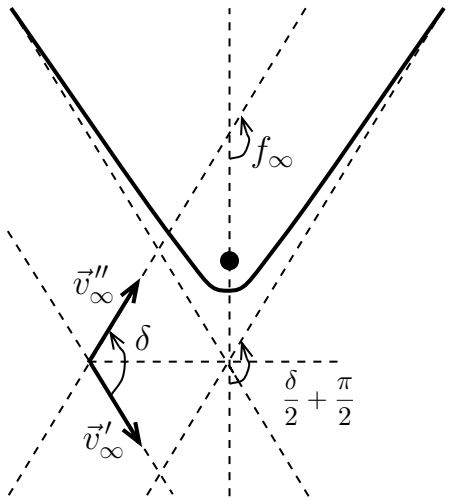

Figure 2.9: Hyperbolic flyby diagram with bending angle

To understand the bending from a flyby, let's start with the conic equation for the flyby:

$$r_{fb} = \frac{a_{fb}(1 - e_{fb}^2)}{1 + e_{fb}\cos(f_{fb})} \tag{2.133}$$

and solve for true anomaly:

$$\cos(f_{fb}) = \frac{1}{e_{fb}}\left[\frac{a_{fb}}{r_{fb}}(1 - e_{fb}^2) - 1\right] \tag{2.134}$$

The true anomaly as $r_{fb} \to \infty$ is f_∞:

$$\begin{aligned} \cos(f_\infty) &= \lim_{r_{fb}\to\infty}\left[\frac{a_{fb}(1 - e_{fb}^2)}{r_{fb}e_{fb}} - \frac{1}{e_{fb}}\right] \\ &= -\frac{1}{e_{fb}} \end{aligned} \tag{2.135}$$

By the geometric construction in Fig. 2.9, the f_∞ angle is also given by:

$$f_\infty = \frac{\delta}{2} + \frac{\pi}{2} \tag{2.136}$$

so:

$$-\cos(f_\infty) = -\cos\left(\frac{\delta}{2} + \frac{\pi}{2}\right) = \sin\left(\frac{\delta}{2}\right) \tag{2.137}$$

The flyby orbit periapsis then gives:

$$e_{fb} = 1 - \frac{r_{pfb}}{a_{fb}} \tag{2.138}$$

$$a_{fb} = \frac{\mu_{fb}}{v_\infty^2} \tag{2.139}$$

$$e_{fb} = 1 + \frac{r_{pfb}v_\infty^2}{\mu_{ga}} \tag{2.140}$$

So, the bending angle of the flyby (δ) is:

$$\sin\left(\frac{\delta}{2}\right) = \frac{\mu_{ga}}{\mu_{ga} + r_{pfb}v_\infty^2} \tag{2.141}$$

or in terms of the ΔV between $\vec{v}'_\infty$ and $\vec{v}''_\infty$:

$$\Delta V_{fb} = \frac{2v_\infty\mu_{ga}}{\mu_{ga} + r_{pfb}v_\infty^2} \tag{2.142}$$

2.5.2 Asymptote Sub-Point

Most moons in the solar system[3] are tidally locked to their planet. In terms of coordinate systems, this means that the moon's prime meridian, on average, points towards the planet, i.e. the $-\hat{p}_1$ direction. In addition, the poles of most moons point in the direction of their orbit normals.

This creates a correspondence in the orientation of the crank sphere shown in Fig. 2.2 and the latitude and longitude on a body. And we may write the v-infinity unit vector in terms of latitude (ϕ) and longitude (λ) for such moons [34] (neglecting any libration of the prime meridian):

$$\hat{v}_\infty = -\cos(\phi_0)\cos(\lambda_0)\hat{p}_1 - \cos(\phi_0)\sin(\lambda_0)\hat{p}_2 + \sin(\phi_0)\hat{p}_3 \tag{2.143}$$

Equation 2.143 may be used with Eqn. 2.49 to convert pump and crank to latitude and longitude, and Eqn. 2.48 may be used with inclination and flight path angle.

2.5.3 The B-Plane

Planet or satellite flyby approach trajectories are typically targeted in B-plane coordinates, which have good numerical convergence [35]. The *B-plane* is a plane passing through the target body center and perpendicular to the asymptote of the

[3]Saturn's moon Hyperion is not tidally locked. In fact, it is chaotically rotating. But all moons in the Solar System larger than Hyperion (and even several smaller such as Uranus' Miranda) are tidally locked and their poles point very closely to their orbit normals.

incoming trajectory. The *B-vector* is a vector in that plane, from the planet center to the piercing-point of the trajectory asymptote. The B-vector specifies where the point of closest approach would be if the target planet had no mass and did not deflect the flight path. Coordinates are defined by three orthogonal unit vectors, $\hat{S}$, $\hat{T}$, and $\hat{R}$, with the system origin at the center of the target body. The $\hat{S}$ vector is a unit vector parallel to the spacecraft $\vec{v}_\infty$ vector .

$$\hat{S} = \hat{v}'_\infty = \hat{b}_3 \tag{2.144}$$

$\hat{T}$ is arbitrary. For planetary moon tours, $\hat{T}$ is usually specified to lie in the target body's equatorial plane. For interplanetary trajectories it is also often specified to either lie in the ecliptic or be normal to the Earth's pole vector. I will define $\hat{T}$ as the cross product of the incoming asymptote and the flyby body's pole vector ($\hat{p}_3$):

$$\hat{T} = \frac{\hat{S} \times \hat{p}_3}{\cos\phi_0} = \hat{b}_1 \tag{2.145}$$

Equation 2.145 is divided by the cosine of the latitude of the asymptote (ϕ_0) in order to render $\hat{T}$ a unit vector since generally $\hat{S}$ and $\hat{p}_3$ are not orthogonal. Finally $\hat{R}$ completes the orthogonal triad:

$$\hat{R} = \hat{S} \times \hat{T} = \hat{b}_2 \tag{2.146}$$

This coordinate system is shown in Fig. 2.10. The angle from the $+\hat{T}$ axis to the B-vector is the *B-plane angle*, θ_{fb}.

The B-vector is then given by:

$$\vec{B} = B\left[\cos(\theta_{fb})\hat{b}_1 + \sin(\theta_{fb})\hat{b}_2\right] \tag{2.147}$$

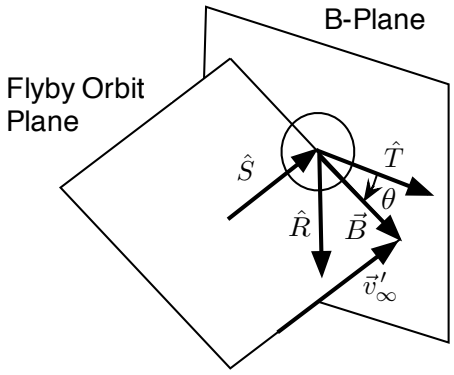

Figure 2.10: B-plane diagram

The magnitude of $\vec{B}$, referred to as the *impact parameter*, is found from the flyby angular momentum:

$$h_{fb} = \mu_{ga}\sqrt{a_{fb}(1-e_{fb}^2)} \tag{2.148}$$

$$= r_{pfb}v_{pfb} \tag{2.149}$$

$$= \sqrt{\mu_{ga}r_{pfb}\left(2\mu_{ga} - r_{pfb}v_\infty^2\right)} \tag{2.150}$$

Note that as $r_{fb} \to \infty$:

$$\lim_{r_{fb}\to\infty}[\vec{r}_{fb} \times \vec{v}_{fb}] = Bv_\infty\hat{h}_{fb} \tag{2.151}$$

therefore:

$$B = \sqrt{r_{pfb}^2 + 2\mu_{ga}r_{pfb}/v_\infty^2} \tag{2.152}$$

It is common to specify the flyby *aim point* in terms of $\vec{B}\cdot\hat{T}$ and $\vec{B}\cdot\hat{R}$:

$$\vec{B}\cdot\hat{T} = B\cos(\theta_{fb}) \tag{2.153}$$

$$\vec{B}\cdot\hat{R} = B\sin(\theta_{fb}) \tag{2.154}$$

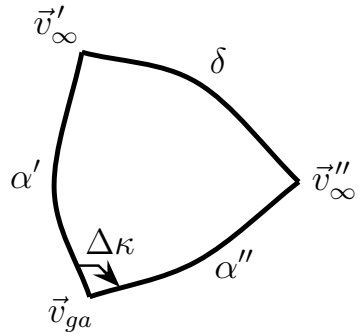

Figure 2.11: Spherical triangle for components of bending

2.5.4 Pump and Crank Changes

The maximum change in pump angle from a given flyby is when the spacecraft velocity vector before the flyby ($\vec{v}'_{sc}$) and after the flyby ($\vec{v}''_{sc}$) are both in the same plane and there is no change to the crank angle. In that case the change in pump angle is exactly the bending angle from the flyby. However, if some of the bending is used to change the crank angle, less of the bending can be used to change the pump angle.

$$|\alpha'' - \alpha'| \leq \delta \tag{2.155}$$

Figure 2.11 shows the spherical triangle formed by $\vec{v}_{ga}$ and the $\vec{v}_\infty$ vectors before and after the flyby. If α' is the pump angle before the flyby, and α'' is the pump angle after the flyby, Fig. 2.11 shows us how much κ will change with a given bending angle.

From Eqn. 2.28:

$$\vec{v}'_\infty = v_\infty \sin(\alpha')\cos(\kappa')\hat{q}_1 + v_\infty \cos(\alpha')\hat{q}_2 - v_\infty \sin(\alpha')\sin(\kappa')\hat{q}_3 \tag{2.156}$$

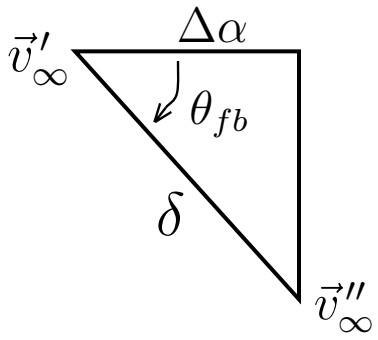

Figure 2.12: Spherical triangle for θ_{fb}

$$\vec{v}''_\infty = v_\infty \sin(\alpha'') \cos(\kappa'')\hat{q}_1 + v_\infty \cos(\alpha'')\hat{q}_2 - v_\infty \sin(\alpha'') \sin(\kappa'')\hat{q}_3 \tag{2.157}$$

and the dot product of these two vectors gives the bending angle:

$$\vec{v}'_\infty \cdot \vec{v}''_\infty = \cos(\delta) \tag{2.158}$$

This dot product then yields a result equivalent to the spherical law of cosines applied to Fig. 2.11:

$$\cos(\delta) = \cos(\alpha') \cos(\alpha'') + \sin(\alpha') \sin(\alpha'') \cos(\Delta\kappa) \tag{2.159}$$

or, solved for $\cos(\Delta\kappa)$:

$$\cos(\Delta\kappa) = \frac{\cos(\delta) - \cos(\alpha') \cos(\alpha'')}{\sin(\alpha') \sin(\alpha'')} \tag{2.160}$$

Equation 2.160 lets us take a bending angle for a given flyby altitude from Eqn. 2.141, and then deduce the change to pump and crank. Or, conversely, the bending required for a given change in pump and crank.

If $\hat{T}$ is in the gravity-assist body's orbit plane, then B-plane angle is the angle of the flyby orbit plane relative to gravity-assist body's orbit plane. Applying Napier's

Rules to the right spherical triangle defined by $\vec{v}'_\infty$ and $\vec{v}''_\infty$ (see Fig. 2.12) then yields the following relation for the B-plane angle, θ_{fb}:

$$\cos(\theta_{fb}) = \frac{\tan(\Delta\alpha)}{\tan(\delta)} \tag{2.161}$$

and

$$\text{sign}(\theta_{fb}) = -\text{sign}(\Delta\kappa) \tag{2.162}$$

2.6 How to Apply the Results in This Chapter

Say we are given some orbit and told it has a gravity assist. We would start with Eqn. 2.66 in § 2.1.3 to get the v_∞ magnitude. Then from § 2.1.4 we use Eqn. 2.67 to get α and Eqn. 2.68 to get κ. Then, if we wanted to see what orbits could be accessed with multiple flybys of this gravity-assist body, we could vary α and κ and use the relations in § 2.3 to find what orbits are possible. We could also assume a minimum r_{pfb} that we would be comfortable with and use Eqn. 2.141 in § 2.5.1 to find a maximum δ. The relations in § 2.5.4 could then be used to look at what pump and crank changes are possible with a single flyby.

Once we pick a new orbit that we want, we can use Eqn. 2.159 to solve for the δ needed from the flyby. Equation 2.141 can then be solved to find the r_{pfb} needed:

$$r_{pfb} = \frac{\mu_{ga}}{v_\infty^2}\left(1/\sin\left(\frac{\delta}{2}\right) - 1\right) \tag{2.163}$$

From here, Eqn. 2.161 gives us the B-plane angle and Eqn. 2.152 gives us the B-plane magnitude, and we now have all that we need to target the flyby that gives us the desired change in pump and crank.

CHAPTER 3. BALLISTIC GRAVITY-ASSIST TRANSFERS

There are two classes of ballistic gravity-assist transfers: same-body and different-body transfers. *Same-body* transfers are to and from the same gravity-assist body. Because of this, there are built-in phasing constraints that both limit the sorts of transfers possible and also allow us to develop some useful analytic relations that are independent of the particular time of the transfer (if we assume the gravity-assist body is in a circular orbit). *Different-body* transfers are between two different gravity-assist bodies. These transfers depend on the relative positions of the two bodies at the time of the transfer, so it is harder to develop general relations to describe these transfers.

In order to develop relations independent of the flyby times, we may assume that the gravity-assist bodies are in circular orbits. We may also assume that the gravity-assist body orbits are coplanar with each other, but not necessarily with the spacecraft orbit. We will get a lot of mileage out of these assumptions as they allow us to eliminate time dependencies with the ephemerides of the gravity-assist bodies. This will allow us to develop methods that provide good insight into the fundamental geometric constraints that govern gravity-assist transfers. We can then use these methods to develop initial guesses for numerical methods that can easily account for the full ephemerides of the gravity-assist bodies.

3.1 Same-Body Transfers

If we perform two flybys of the same gravity-assist body in succession, there are three kinds of ballistic transfers possible between these encounters: resonant, non-resonant, and backflip. Each category of transfer places constraints on the period and inclination of the orbit around the central body. For these transfers, the flyby before

the transfer will be denoted with one prime and the flyby after the transfer with a double-prime.

3.1.1 Resonant Transfers

In the case of the *resonant transfer*, the time of flight between the flybys is some integer multiple of the gravity-assist body's period and resonant transfers are named by the ratio of gravity-assist body revolutions to spacecraft revolutions. Resonant transfers are labeled $N{:}M$, where N is the number of gravity-assist body revs and M is the number of spacecraft revs.[1] For example a 3:1 resonant transfer has 1 spacecraft rev for every 3 gravity-assist body revs and a flight time of 3 gravity-assist body periods. A 4:5 resonance has 5 spacecraft revs for every 4 gravity-assist body revs and has a flight time of 4 gravity-assist body periods. The ratio between the spacecraft orbit's period and the gravity-assist body's period is then:

$$\frac{T_{sc}}{T_{ga}} = \frac{M}{N} \tag{3.1}$$

Since the flight time is an integer number of gravity-assist body periods, both encounters occur at the same place in the gravity-assist body's orbit. That is, the longitude of encounter is the same for the prime and double-prime flybys:

$$L''_{enc} = L'_{enc} \tag{3.2}$$

Therefore, the spacecraft orbit plane is only constrained to contain the line connecting this point to the central body and the transfer may achieve a wide range of inclination.

The pump angle of a resonant transfer, from Eqn. 2.13 and Eqn. 3.1, is given by:

$$\cos(\alpha) = \frac{v_c^2 \left[2 - \left(\frac{N}{M}\right)^{\frac{2}{3}}\right] - v_\infty^2 - v_{ga}^2}{2 v_\infty v_{ga}} \tag{3.3}$$

[1]The $N:M$ labeling is the convention for gravity-assist trajectory design. In the CR3BP, the convention is $M:N$.

The crank angle depends on inclination and is given by Eqn. 2.68:

$$\sin(\kappa) = -\tan(i_{sc}) \left(\frac{v_c/v_\infty + \cos(\alpha)}{\sin(\alpha)} \right) \tag{3.4}$$

where, $-\pi/2 \leq \kappa \leq \pi/2$ for inbound encounters and $\pi/2 \leq \kappa \leq 3\pi/2$ for outbound.

We may repeat the same resonance indefinitely by using the flyby ΔV to change crank and not pump. As we increase or decrease crank from zero, inclination will increase until the maximum inclination is reached for $\kappa = \pm\pi/2$. Beyond that, the flyby will switch from an inbound to outbound flyby and inclination will decrease until $\kappa = \pi$. Then inclination will decrease until $\kappa = \pm 3\pi/2$, and the flyby will switch back to inbound and inclination will decrease again.

Increasing or decreasing crank until the maximum inclination is reached and the flyby switches from inbound to outbound or outbound to inbound is a technique called *cranking over the top*. Cranking over the top is useful both to get ground tracks to globally cover the surface of the gravity-assist body and to move the line of apsides to the other side of the central body.

3.1.2 Non-Resonant Transfers

In the case of the *non-resonant transfer*, the flybys of the gravity-assist body occur at different places in the gravity-assist body's orbit. That is, the prime and double-prime flybys occur at different longitudes of encounter:

$$L''_{enc} = L'_{enc} + 2\pi y \tag{3.5}$$

Equation 3.5 introduces a new quantity, y, which is a non-dimensional time of flight offset:

$$y = t_{trans}/T_{ga} - N_e \tag{3.6}$$

This offset is time of flight of the transfer, t_{trans}, divided by the period of the gravity-assist body minus the number of full revolutions, N_e, of the gravity-assist body between the two encounter times. This number of revolutions is counted by the number of times that the gravity-assist body passes through the initial longitude of encounter. This time of flight offset is also the angular offset between the two encounters in the gravity-assist body's orbit divided by 2π.

Both encounters of the gravity-assist body will fall on a line when y is either 0 or 1/2. When y is zero, we have a resonant transfer. When y is 1/2, we have a special case of the non-resonant transfer that is given its own category, the *backflip transfer*. These backflip transfers are described in the next section and will be excluded from the category of non-resonant transfers. When y is neither 0 nor 1/2, we have a non-resonant transfer where both encounters do not fall on the same line.

Since, both encounters are not on the same line for a non-resonant transfer, the orbit plane of the transfer is uniquely determined. Specifically, all non-resonant transfers must be in the gravity-assist body's orbit plane and therefore have zero inclination.

Non-resonant transfers either go from an inbound to an outbound encounter (IO) or from an outbound to an inbound encounter (OI). Both encounters occur at the same true anomaly magnitude, since both occur at the same r_{enc}. The inbound encounter has a negative true anomaly and the outbound has a positive true-anomaly.

Although, it may first appear that there would be continuum of non-resonant transfers, there are actually only discrete values of orbit period that are allowable for a given v_∞. As will be shown below, once the number of complete spacecraft revolutions (c) and complete gravity-assist body revolutions (d) are specified there is only one inbound-outbound transfer and one outbound- inbound transfer for a given v_∞ magnitude.

Figure 3.1 illustrates a non-resonant transfer where the inbound encounter is labeled 'I' and the outbound encounter is labeled 'O'. In Fig. 3.1, we see that for an outbound to inbound transfer the angle between encounters is $2\pi - 2|f_{enc}|$ and for an inbound to outbound encounter that angle is $2|f_{enc}|$. From Eqn. 3.5, in both cases

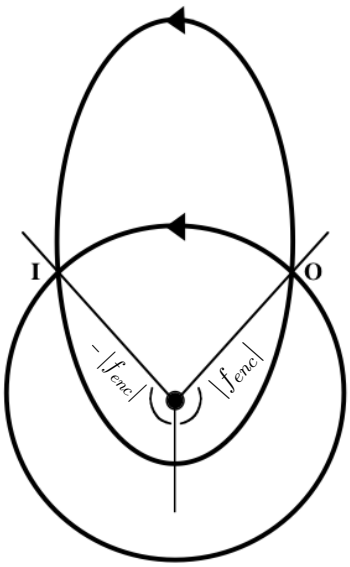

Figure 3.1: Non-resonant transfer

the angle between the encounters is $2\pi y$. From these observations, we may derive this expression for an inbound to outbound transfer in terms of the true anomaly of encounter from Eqn. 2.81:

$$y_{IO} = |f_{enc}|/\pi \tag{3.7}$$

and this expression for an outbound to inbound transfer:

$$y_{IO} = 1 - |f_{enc}|/\pi \tag{3.8}$$

To compute the time of flight of a non-resonant transfer, we first compute the eccentric anomaly for Kepler's equation. This expression gives the eccentric anomaly, which will be negative at the inbound encounter and positive at the outbound encounter:

$$\cos(E_{enc}) = \frac{1}{e_{sc}}\left(1 - \frac{r_{enc}}{a_{sc}}\right) \tag{3.9}$$

Kepler's equation then gives the time from periapsis for the encounters:

$$\tau_{enc} = \frac{T_{sc}}{2\pi} \left[E_{enc} - e_{sc} \sin(E_{enc}) \right] \tag{3.10}$$

As with f_{enc}, τ_{enc} will be negative at the inbound encounter and positive at the outbound encounter, but will have the same magnitudes for both encounters. It is possible for an inbound to outbound transfer to use a hyperbolic (or parabolic) orbit around the central body. The hyperbolic anomaly for this case is given by:

$$\cosh(H_{enc}) = \frac{1}{e_{sc}} \left(1 - \frac{r_{enc}}{a_{sc}} \right) \tag{3.11}$$

and the time from periapsis is:

$$\tau_{enc} = \frac{1}{v_c} \sqrt{\frac{a_{sc}}{r_{enc}}} \left[e_{sc} \sinh(E_{enc}) - H_{enc} \right] \tag{3.12}$$

Hyperbolic and parabolic transfers are special cases of interest for trajectories that capture or escape the central body. However, the bulk of gravity-assist tour design is concerned with elliptic and circular transfers, and we will ignore unbound orbit cases for the remainder of the chapter.

The time of flight for an inbound to outbound transfer is given by:

$$t_{trans;IO} = c\, T_{sc} + 2|\tau_{enc}| \tag{3.13}$$

Here, $M_a$is the number of apoapses in the spacecraft's orbit passed between encounters. The time of flight for an outbound to inbound transfer is:

$$t_{trans;OI} = c\, T_{sc} - 2|\tau_{enc}| \tag{3.14}$$

In Eqn. 3.14, for an outbound to inbound transfer, the spacecraft must pass through at least one apoapsis.

If we combine Eqn. 3.13 with Eqn. 3.6, we get the following for an inbound to outbound transfer:

$$y_{IO} = \frac{1}{T_{ga}} \left(M_a \, T_{sc} + 2|\tau_{enc}| \right) - N_e \tag{3.15}$$

and from combining Eqn. 3.14 with Eqn. 3.6, we get the following for an outbound to inbound transfer:

$$y_{OI} = \frac{1}{T_{ga}} \left(M_a \, T_{sc} - 2|\tau_{enc}| \right) - N_e \tag{3.16}$$

The angular offset is given by Eqn. 3.7 and Eqn. 3.8, and the time of flight offset is given by Eqn. 3.15 and Eqn. 3.16. Since y is non-dimensionalized to be both an angular and a time of flight offset, we can impose the condition that the gravity assist body is reencountered by combining these equations. After M_a and N_e are selected, the period of the transfer is determined by solving the system of equations with a given value of v_∞: Eqn. 3.7 and Eqn. 3.15 for and inbound-outbound transfer or Eqn. 3.8 and Eqn. 3.16 for an outbound-inbound transfer. These equations may be solved iteratively, using the relations in § 2.3 to get a_{sc} and e_{sc}. Solutions for some example cases are given in Table 3.1.

The pump angle for these transfers are found from the period by:

$$\cos(\alpha) = \frac{v_c^2 \left[2 - \left(\frac{T_{ga}}{T_{sc}} \right)^{\frac{2}{3}} \right] - v_\infty^2 - v_{ga}^2}{2 v_\infty v_{ga}} \tag{3.17}$$

The crank angle for a non-resonant transfer is either 0 or π depending on whether the flyby is inbound or outbound respectively.

Orbit Orientation Changes with Non-Resonant Transfers

WIth the relations in § 2.3 we see from Eqn. 2.79 that as period increases, eccentricity decreases and in Eqn. 2.80 that as period increases, $|\omega_{sc}|$ decreases. But

Table 3.1: Example Non-Resonant Transfers

v_∞/v_c	N_e	M_a	IO:T_{sc}/T_{ga}	OI:T_{sc}/T_{ga}
0.5	1	0	0.541	0.432
0.5	1	1	1.247	1.830
0.5	1	2	2.149	2.878
0.5	1	3	3.116	3.896
0.5	1	6	6.087	6.917
0.5	2	1	0.719	0.802
0.5	2	2	1.137	1.390
0.5	2	3	1.596	1.919
0.5	3	1	0.518	0.475
0.5	3	2	0.799	0.880
0.5	3	3	1.095	1.251
1.0	1	0	0.682	0.354
1.0	1	1	1.531	1.461
1.0	1	2	2.460	2.545
1.0	1	3	3.422	3.583
1.0	1	6	6.372	6.630
1.0	2	1	0.823	0.656
1.0	2	2	1.281	1.214
1.0	2	3	1.754	1.746
1.0	3	1	0.570	0.422
1.0	3	2	0.878	0.781
1.0	3	3	1.192	1.139
1.5	1	0	0.727	0.432
1.5	1	1	1.817	1.200
1.5	1	2	2.787	2.197
1.5	1	3	3.768	3.222
1.5	1	6	6.738	6.259
1.5	2	1	0.879	0.647
1.5	2	2	1.409	1.105
1.5	2	3	1.907	1.587
1.5	3	1	0.559	0.459
1.5	3	2	0.921	0.756
1.5	3	3	1.269	1.072

since $\text{sign}(\omega_{sc}) = \text{sign}(\kappa)$, a period increase decreases ω_{sc} for an outbound flyby and increases it for an inbound flyby. Since non-resonant transfers switch from inbound to outbound and vice versa, it is possible to use a repeating sequence of pump-up (i.e. period increasing) and pump-down (i.e. period decreasing) flybys to rotate the spacecraft orbit. Table 3.2 from Wolf and Smith [9] summarizes how pumping changes orientation with non-resonant transfers. Using such sequences of non-resonant transfers to change orbit orientation is called *petal rotation*. An example of this petal rotation is shown in Fig. 3.2.

Table 3.2: Orbit Orientation Changes

	pump-up flyby	pump-down flyby
inbound flyby	clockwise orbit rotation	counterclockwise orbit rotation
outbound flyby	counterclockwise orbit rotation	clockwise orbit rotation

3.1.3 Backflip Transfers

Backflip Transfers are a special case of a non-resonant transfer where the second encounter is π radians from the first. Because of this they are also sometimes called $n\pi$-transfers, π-transfers, or 180° transfers. Figure 3.3 shows an example backflip transfer.The longitude of encounter of the prime and double-prime flybys differ by π radians:

$$L''_{enc} = L'_{enc} \pm \pi \tag{3.18}$$

Backflips are useful in tour design as they move the longitude of encounter by π radians in a single transfer. When accessible, they are the quickest method to move the longitude of encounter.

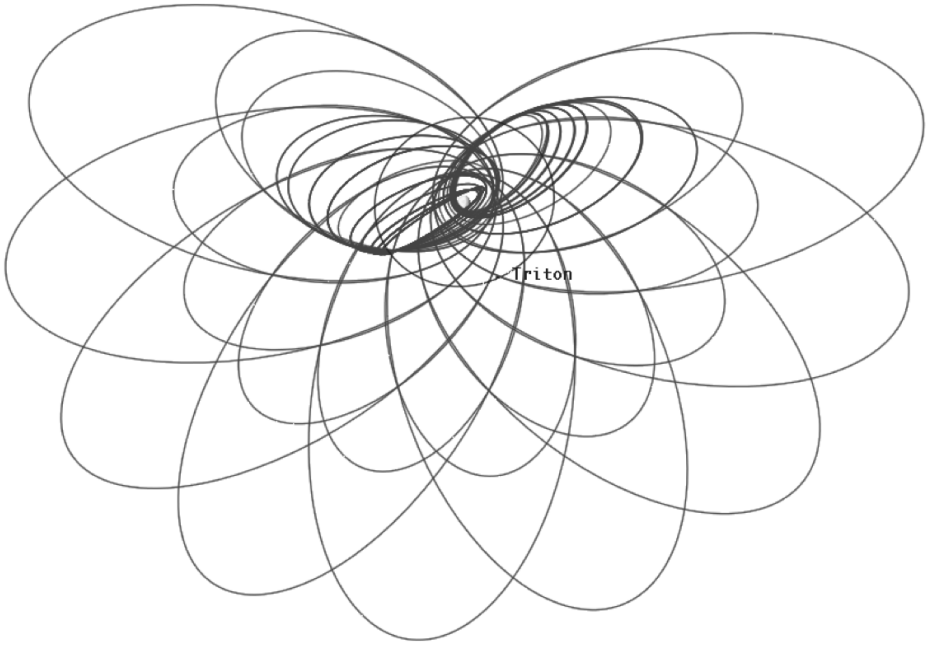

Figure 3.2: Example petal rotation with Triton

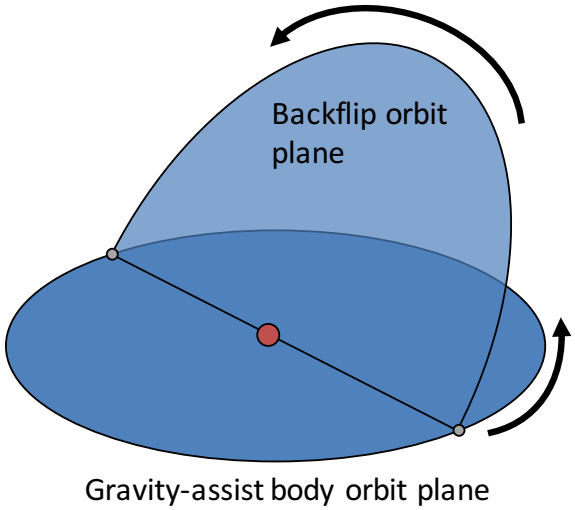

Figure 3.3: Illustration of same-body backflip transfer

The flybys of a backflip occur on a line that runs through the central body. This means that backflips can be inclined like resonant transfers. Setting y=1/2 in Eqn. 3.15 and Eqn. 3.16 gives analogous equations for backflips. For an inbound to outbound backflip:

$$\left(N_e + \frac{1}{2}\right) T_{ga} = M_a\, T_{sc} + 2|\tau_{enc}| \tag{3.19}$$

and for an outbound to inbound backflip transfer:

$$\left(N_e + \frac{1}{2}\right) T_{ga} = M_a\, T_{sc} - 2|\tau_{enc}| \tag{3.20}$$

An additional constraint is placed on backflips since the only way to have two encounters π radians apart is for both flybys to be on the line of nodes. This requires that $\omega_{sc} = \pm\pi/2$. From Eqn. 2.80:

$$e_{sc}^2 = 1 - \frac{r_{enc}}{a_{sc}} \tag{3.21}$$

When Eqn. 3.21 is substituted into Eqn. 3.9, we get the interesting result that the eccentric anomaly of a backflip depends only on the semimajor axis (and therefore the period):

$$\cos(E_{enc}) = \sqrt{1 - \frac{r_{enc}}{a_{sc}}} \tag{3.22}$$

This means that Kepler's Equation and therefore Eqn. 3.19 and Eqn. 3.20 are independent of v_∞ magnitude. Table 3.3 provides some example solutions to Eqn. 3.19 and Eqn. 3.20.

Equation 3.21 can be combined with Eqn. 2.79 to yield the following expression for the inclination of a backflip transfer:

$$\cos(i_{sc}) = \frac{1}{2}\left[3 - \frac{r_{enc}}{a_{sc}} - \left(\frac{v_\infty}{v_c}\right)^2\right] \tag{3.23}$$

Table 3.3: Example Same-Body Backflip Transfers

N_e	M_a	IO:T_{sc}/T_{ga}	OI:T_{sc}/T_{ga}
0	0	1	*no transfer*
1	0	*no transfer*	1
1	1	1.135	1.785
1	2	2.231	2.758
1	3	3.249	3.747
1	4	4.257	4.740
1	5	5.262	5.736
2	2	1.045	1.407
2	3	1.602	1.890
3	3	1.023	1.277

This is an important result: there is only one permissible inclination for a given d, c same-body backflip transfer depending on v_∞. Backflip transfers can be very difficult to converge numerically without using the inclination constraint from Eqn. 3.23.

3.1.4 The V-Infinity Globe

Figure 2.2 showed a sphere for all v-infinity vectors with the same magnitude. Each point on this sphere represents a direction of $\vec{v}_\infty$, and therefore a corresponding $\vec{v}_{sc}$. This, as was shown in § 2.3, is then sufficient to uniquely determine the orbit about the central body. The surface of the *v-infinity globe* therefore represents all orbits with a given v_∞ magnitude with respect a the gravity-assist body.

By relating the pump and crank of a v-infinity vector to the orbit of the central body, we can draw contours of orbits on the v-infinity globe representing orbits with a given characteristic such as orbit period or inclination as shown in Fig. 3.4. In Fig. 3.4, blue contours representing orbits with the same orbit period and green contours with the same inclination. To draw contours of constant period we use Eqn. 2.67, and to draw contours of constant inclination we use Eqn. 2.68.

We will use the outbound asymptotes from flybys in a tour to draw a map of that tour on the v-infinity globe. The inbound flyby asymptotes could also be plotted as the negative vector of the outbound asymptotes from the previous flybys in a tour. If this were done, a flyby's groundtrack would then be a great circle connecting these two points.

If we assume that the gravity-assist body is in a circular orbit we can non-dimensionalize the tour map so that it is applicable to any moon. To do this we divide distances by r_{enc}, velocities by v_c, and times by T_c. Figure 3.5 shows this map for $v_\infty/v_c = 0.75$ with vacant node contours, non-resonant, and backflip transfers added. Figure 3.6 through Fig. 3.10 shows this for other values of v_∞/v_c.

In these plots, contours of constant period are shown in blue and labeled with their resonance with respect to gravity-assist body. Inclination contours are shown in green for steps of 10 degrees. Node radius contours non-dimesionlized in terms of r_{vac}/r_{enc} are shown in cyan. The red period contour represents escape energy, and the orbits in the region bounded by it are hyperbolic with respect to the central body. Similarly, the dashed black contour bounds orbits that are retrograde. Finally the magenta 'x' and 'o' marks represent some non-resonant and backflip transfers. The 'x' represents the asymptote before a transfer, and the 'o' is the asymptote after the transfer.

On these maps, the "northern hemisphere" is comprised of orbits which have the gravity-assist encounter at the ascending node, and the "southern hemisphere" of encounters is at the descending node. The hemisphere from 90° E to 90° W (i.e. the moon's anti-planet hemisphere) is comprised of asymptotes for orbits which encounter the gravity-assist body outbound from periapsis, and the opposite hemisphere is comprised of orbits with inbound flybys.

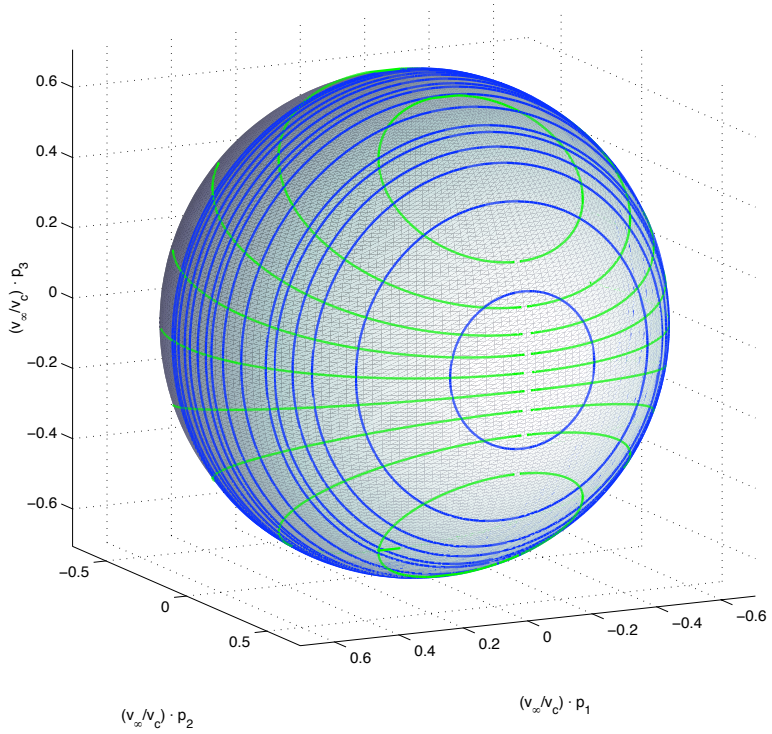

Figure 3.4: The V-Infinity Globe

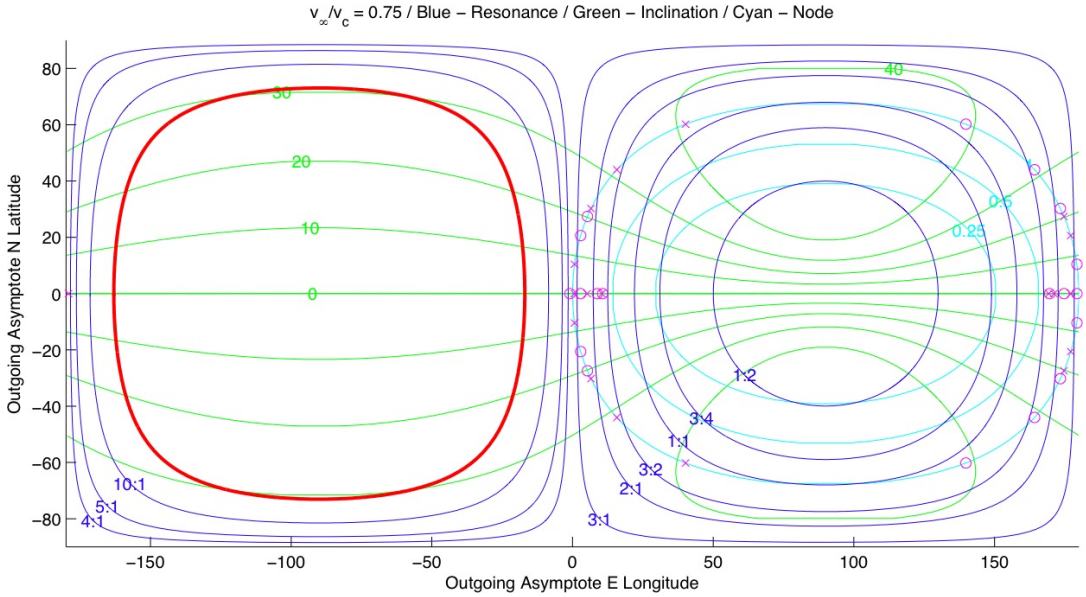

Figure 3.5: Non-dimensional Tour Map, $v_\infty/v_c = 0.75$

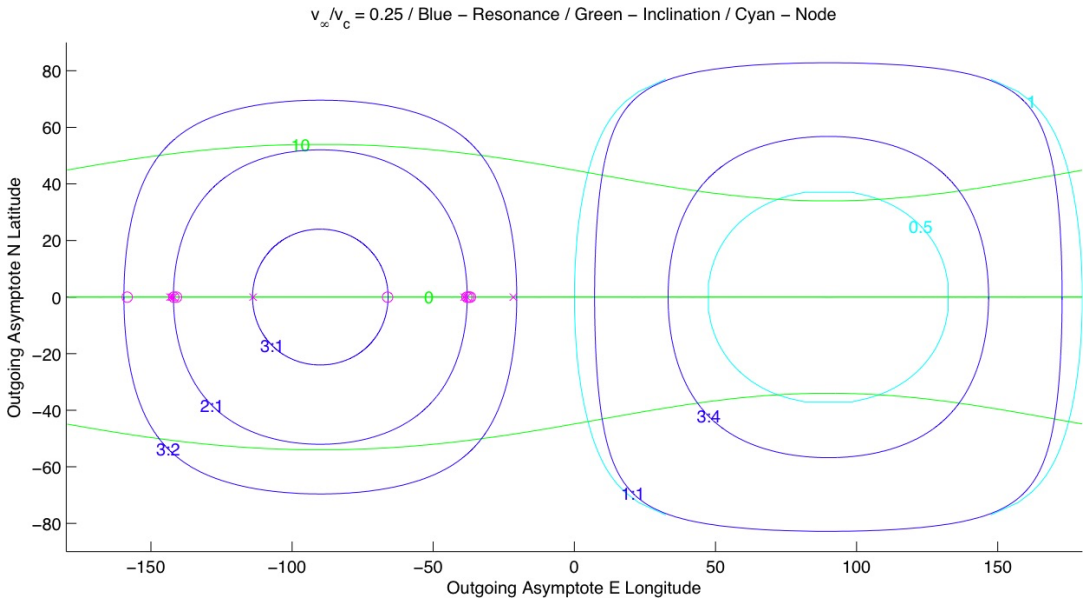

Figure 3.6: Non-dimensional Tour Map, $v_\infty/v_c = 0.25$

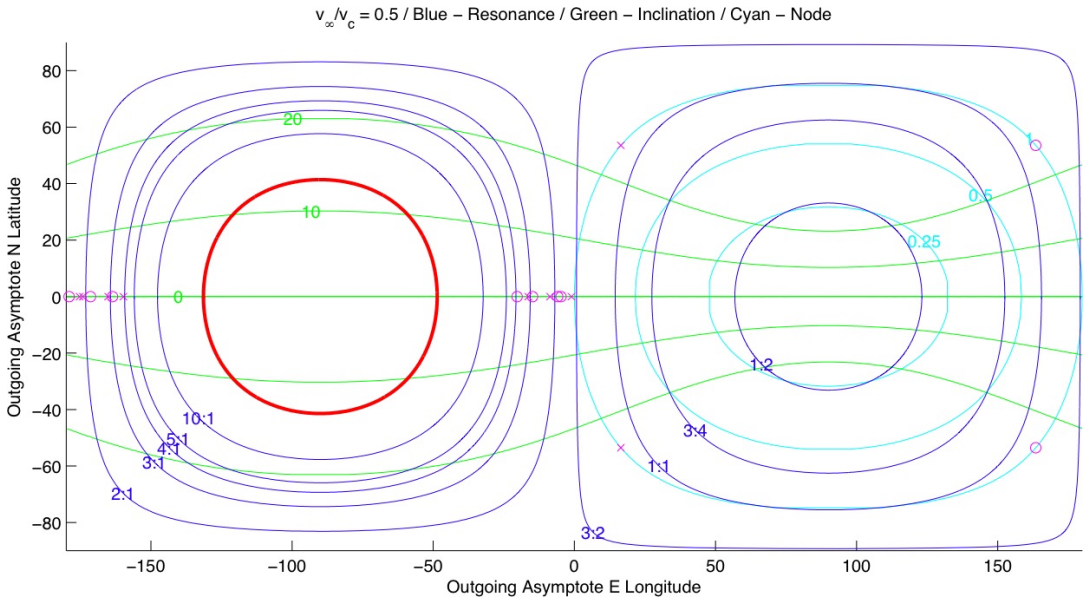

Figure 3.7: Non-dimensional Tour Map, $v_\infty/v_c = 0.5$

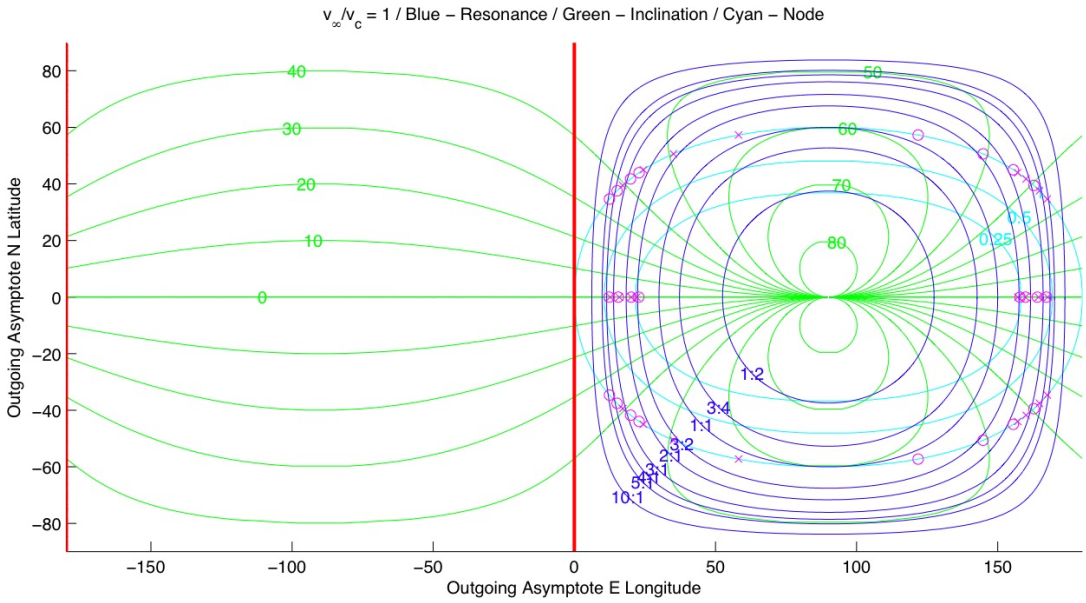

Figure 3.8: Non-dimensional Tour Map, $v_\infty/v_c = 1.0$

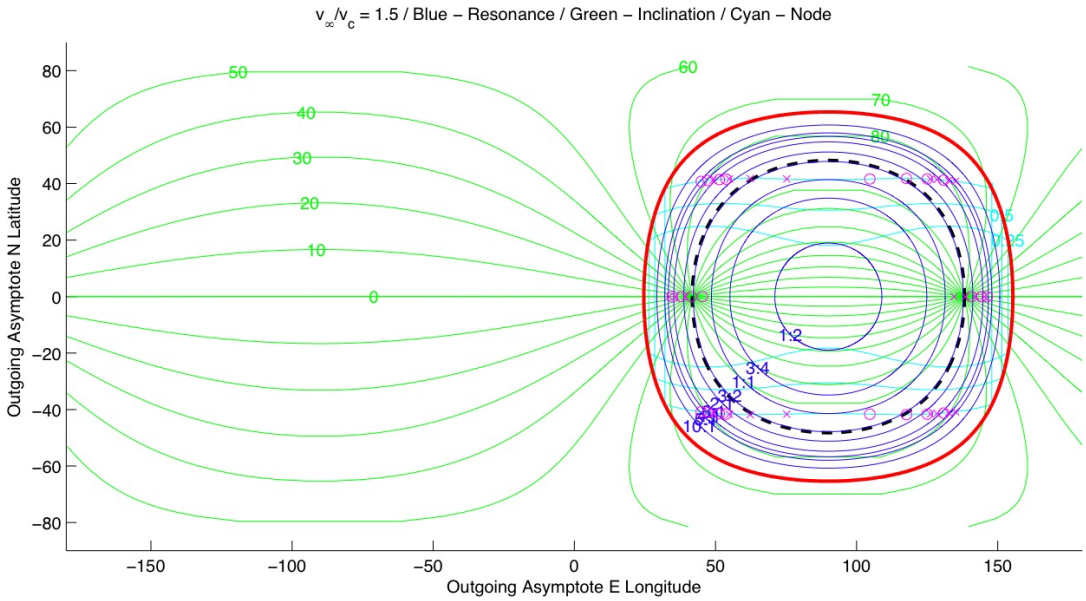

Figure 3.9: Non-dimensional Tour Map, $v_\infty/v_c = 1.5$

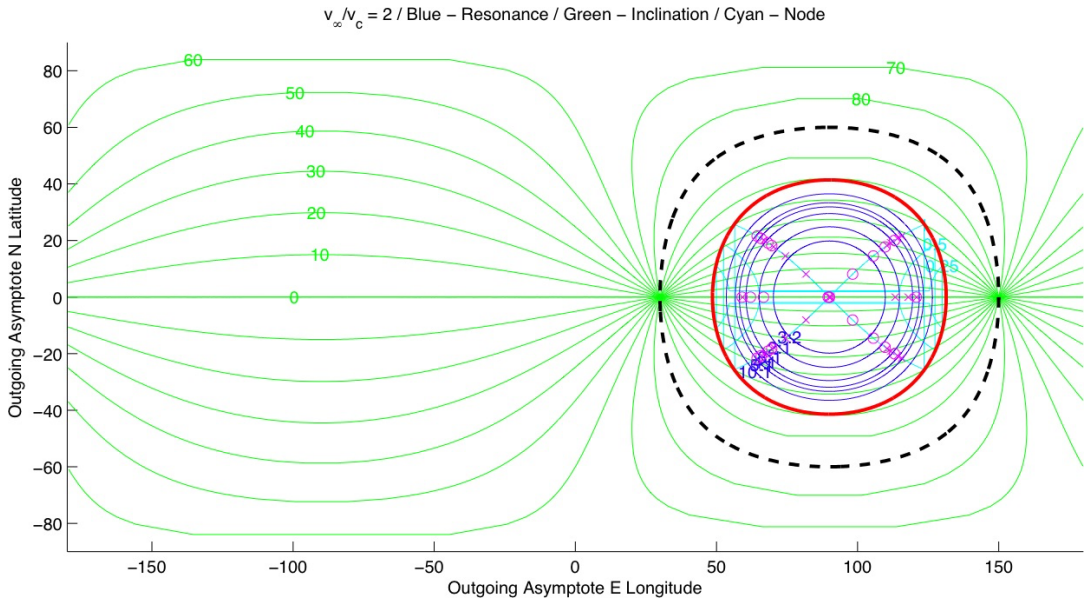

Figure 3.10: Non-dimensional Tour Map, $v_\infty/v_c = 2.0$

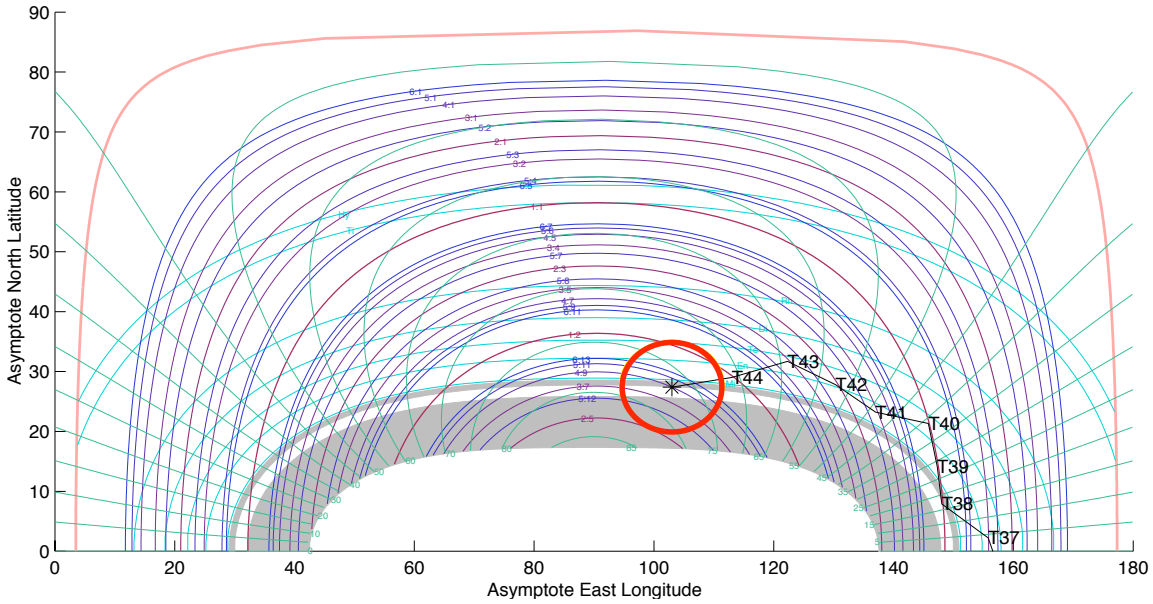

Figure 3.11: Tour Map for Cassini extended mission

Bending Angle

The bending angle from a flyby becomes a distance on the surface of the v-infinity globe. If we had a three-dimensional v-infinity globe at our disposal, we could measure this distance with a pair of spanners to plot a tour. In practice, we can also do this with a ruler on two-dimensional projections as long as we stay away from areas of the tour map which are most distorted by the projection (e.g. the high latitudes in the cylindrical projections used in this chapter).

3.1.5 Application To Cassini Extended Mission Design

Figure 3.11 is the tour map that was used for much of the early Cassini extended mission design. It is a detailed map for the Cassini v-infinity at the end of the prime mission (5.8 km/s) showing many various Titan resonances. Node crossing distances are shown for the orbits of all of the major satellites except for Iapetus[2], and node crossings that intersect the rings are shown as a grey region. Orbits with periapses below Saturn's surface are in the central white region.

The last few orbits of the Cassini prime mission are plotted on Fig. 3.11. Each orbit is a point, and the flybys are the lines connecting the points. The last orbit of the prime mission is marked with an asterisk and a red circle is drawn around it showing the $8°$ of bending from a 1000 km Titan flyby. The extended mission will start from this point and move in steps of $8°$ or less across the map.

With this map, the Cassini tour designers were able to draw in tours with a pencil and a ruler. The flight times of the tours could then be estimated by adding up the Titan revs of the various resonant orbits. From this map, the tour designers could quickly assess the various methods for achieving equatorial orbits or placing the node crossings at the orbits of other moons (particularly Enceladus).

[2]Iapetus orbits in a different plane from the other satellites and encounters with it do not necessarily occur on the line of nodes of the spacecraft's orbit.

3.2 Different-Body Transfers

For different body transfers the general approach to find them is to start from the position of the first body at the time of the flyby and then use a Lambert solver to find transfers to the second body. The transfer flight time and the number of revolutions of the spacecraft orbit are varied to give a set of Lambert arcs connecting the two bodies. The departure v_∞ is then calculated for each Lambert arc and those that match the inbound v_∞ at the first flyby are then checked to see how much bending is needed from the flyby to reach. Transfers that can be reached with flyby altitudes above some preset minimum are then considered valid options. This algorithm, called *C_3-matching*,[3] is a numerical approach that is dependent on the epoch and initial conditions for a given tour. Although this technique has been used to great effect in tools such as STOUR [11–13] to find gravity-assist tours, it can only offer point solutions.

In this section, we will attempt to gain insight into general, epoch-independent, different-body transfers using the relations developed in the previous chapter. To do this, we will look at planar transfers where both gravity-assist bodies and the spacecraft orbit are all in the same plane and at inclined backflip transfers where the two gravity-assist bodies are at node crossings of the spacecraft orbit.

3.2.1 Planar Transfers and Tisserand Graphs

For planar different-body transfers, the following two equations from § 2.3 (modified for zero i_{sc}) can be very useful:

$$\frac{r_{enc}}{a_{sc}} = 2 - \frac{1}{v_c^2}\left[v_\infty^2 + v_{ga}^2 + 2v_\infty v_{ga}\cos(\alpha)\right] \tag{3.24}$$

[3] where $C_3 = v_\infty^2$

$$e_{sc}^2 = 1 - \frac{1}{4}\frac{r_{enc}}{a_{sc}}\left(3 - \left(\frac{v_\infty}{v_c}\right)^2 - \frac{r_{enc}}{a_{sc}}\right)^2 \tag{3.25}$$

If we vary α from 0 to π we get all possible values of a_{sc} and e_{sc} for a given v_∞. We can then use this to plot contours of the possible orbits for a given v_∞. Figure 3.12 is an exampel of this plotting v_∞ of specific energy and periapsis radius for the inner Solar System. Here contours of $1, 3, 5, 7, \ldots$ km/s v_∞ are plotted for Mercury, Venus, Earth, and Mars. Where the contours intersect a transfer is possible between those two planets with the v_∞ at each planet given by the respective contour. Dashed lines at the top of the plot show orbits that can reach the outer planets starting with Jupiter on the bottom. Marks on each contour correspond to a $\Delta\alpha$ equal to the bending angle, δ, corresponding to a 300 km flyby at each planet. These tick marks enable us to estimate how far along each contour a single flyby can change the heliocentric orbit.

Because of the connection between Eqn. 3.25 and the Tisserand Parameter (as explained in § 2.4.5), Fig. 3.12 is called a *Tisserand Graph* (a term first coined by Longuski and introduced in Strange and Longuski [18]). This Tisserand Graph plots specific energy and periapsis radius (an "$\mathcal{E}$-r_p plot"). Other Tisserand Graphs plot period and periapsis (a "P-r_p plot"), apoapsis and periapsis (a "r_a-r_p plot"), or any other pair of quantities derived from a_{sc} and e_{sc}. In a Tisserand Graph each point on the plot represents an orbit of the central body and flybys can be used to modify that orbit by moving along a v_∞-contour. Tick marks are used to estimate when multiple flybys are needed to move a certain distance along a contour. Gravity-Assist tours can be designed by following contours across a plot. As an example, a VEEGA trajectory that launches with a v_∞ of 3 km/s from Earth and then uses one Venus and two Earth flybys to reach Jupiter is drawn on Fig. 3.12. Figure 3.13 shows this VEEGA in more detail on a P-r_p plot. Figure 3.14 shows an example P-r_p plot used for a Jupiter Europa Orbiter tour design by Kloster et al. [36] This Tisserand Graph

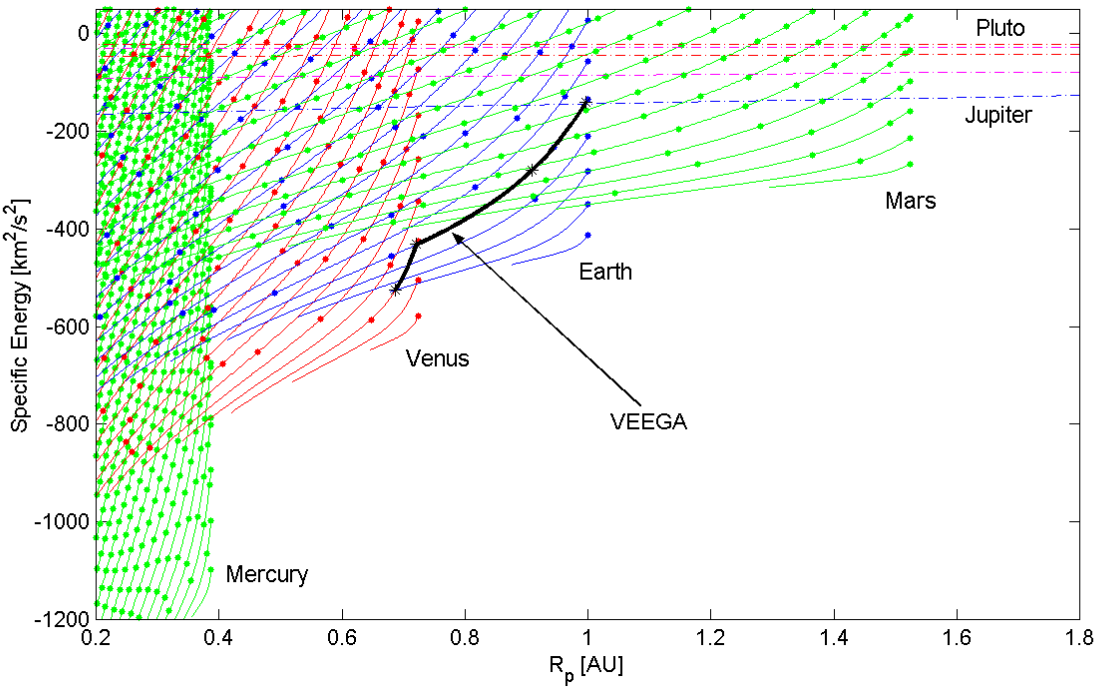

Figure 3.12: Example $\mathcal{E}$-r_p Tisserand Graph [18]

has estimated radiation dose contours (in krad per orbit) overlaid to assist with the design of a low radiation tour (magenta). The v_∞ contours in Fig. 3.14 are in steps of 1 km/s, starting at 1 km/s.

3.2.2 Backflips and the Vacant Node

An inclined different body transfer is also called a *Backflip Transfer* as both encounters happen on the line of nodes. In Fig. 3.15 the first flyby in the transfer is at the point labeled *encounter* and the second is at the *vacant node*. In order for the transfer to be possible the vacant node must be at the orbit radius of the central body. If we place r_{enc} at the radius of the first body's orbit and r_{vac} at the radius of the

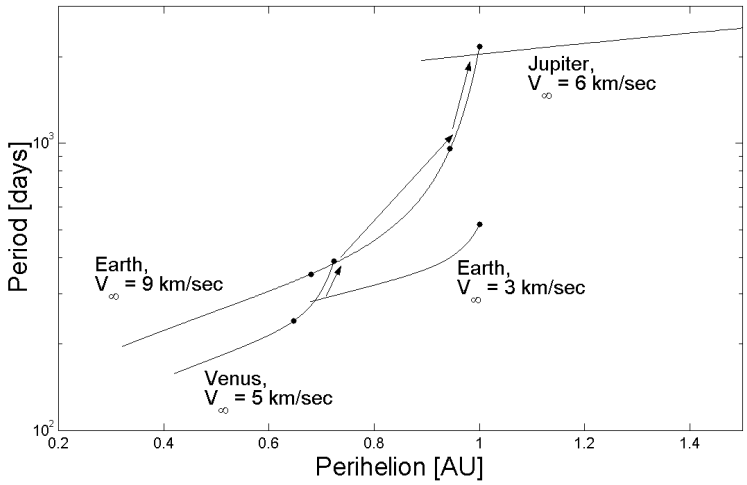

Figure 3.13: Example P-r_p Tisserand Graph for VEEGA [18]

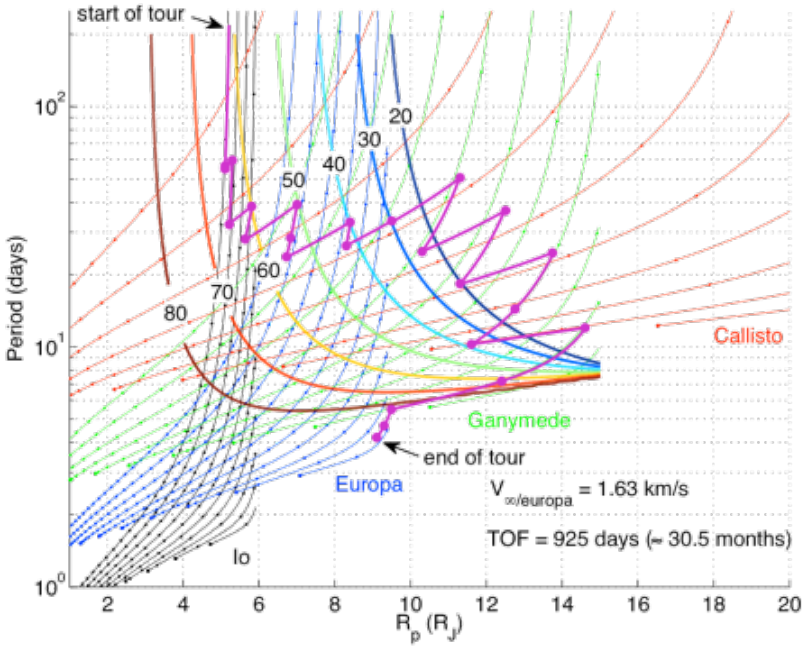

Figure 3.14: Example Tisserand Graph for JEO tour design [36]

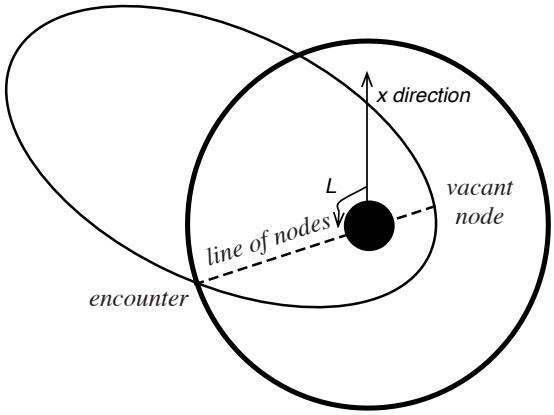

Figure 3.15: Vacant Node

second body's orbit and combine Eqn. 2.76 with Eqn. 3.25 we can get the following expression for the inclination required for a different-body backflip:

$$\cos(i_{sc}) = \sqrt{\frac{1}{8}\left(1+\frac{r_2}{r_1}\right)}\left(3-\left(\frac{v_\infty}{v_1}\right)^2-\frac{r_1}{a_{sc}}\right) \tag{3.26}$$

where r_1 is the first body's orbit radius, v_1 is the circular orbit velocity at r_1, and r_2 is the second body's orbit radius.

3.3 Are These Transfers Really Ballistic?

The methods in this chapter can be used to design a tour that will have no ΔV in the idealized patched-conic model with circular coplanar gravity-assist bodies. This idealized tour can then be used as an initial guess for an optimizer using the full force model, which can then be used to find deterministic ΔV needed to fly this tour design. This deterministic ΔV will in general be non-zero, so these transfers are not ballistic in the "real world". However, these idealized relations are still very useful for getting initial guesses to use in the optimizers with high-fidelity force models.

CHAPTER 4. V-INFINITY LEVERAGING

For spacecraft trajectories using gravity assists, a spacecraft's v_∞ (i.e. hyperbolic excess velocity) relative a gravity-assist body cannot usually be changed without a gravity assist from another body or a maneuver. The term *V-Infinity Leveraging* refers to using maneuvers to change v_∞ and was first coined by Longuski (and first appears in print in Williams' Masters Thesis [12]). A small leveraging maneuver can translate into a change in v_∞ ten or more times larger than the maneuver itself. As the bending provided by a flyby is a function of the flyby v_∞, leveraging maneuvers provide an economical way to influence the efficacy of a flyby.

V-infinity leveraging decreases v_∞ by making the orbit around the central body more circular, and increases v_∞ by making that orbit more eccentric. For *exterior leveraging* a maneuver is done near apoapsis that raises periapsis to lower v_∞, or lowers periapsis to increase v_∞. *Interior leveraging* uses a maneuver at periapsis to change v_∞ by changing the orbit's apoapsis. A detailed description of V-Ininfity Leveraging and related nomenclature is provided in Sims, Longuski, and Staugler [14].

4.1 Non-Tangent V-Infinity Leveraging

Past work [14, 15, 22–24] in V-Infinity Leveraging Transfers (VILTs) has largely focused on *tangent leveraging*, i.e. leveraging where the v_∞ vector is tangent to the gravity-assist body's velocity vector at one end of the transfer. For example, an exterior VILT that reduces v_∞ would use a maneuver at apoapsis to raise periapsis to the gravity-assist body's orbital distance. Such a VILT would achieve the maximum reduction in v_∞ for a given apoapsis radius. Tangent VILTs are very efficient at getting the maximal change in v_∞ for a give transfer time.

In this application where we want to rotate the v_∞ vector by 180°, such tangent leveraging may undo rotation provided by flybys before the VILT. For example, when going from a Titan-Rhea Hohmann to a Rhea-Dione Hohmann, Rhea starts out at periapsis of the Saturn-centered orbit and flybys are used to lower periapsis to Dione. Exterior tangent VILTs to reduce v_∞ will tend to move periapsis back to Rhea and undo the work of the flybys in lowering periapsis. This chapter will look at non-tangent VILTs as a way to balance the larger bending provided by lower v_∞ against the tendency for leveraging to sometimes retard the progress of flybys.

4.1.1 Resonance Hopping

When constructing a sequence of flybys using only one gravity-assist body, three types of transfers between flybys are available [8, 15]. *Resonant transfers* are transfers where the flight time between flybys is an integer multiple of the gravity-assist body's period, T_{ga}. Because of this, both flybys of a resonant transfer occur at the same location in the gravity-assist body's orbit. *Non-resonant transfers* are transfers where the flight time of the transfer is not a integer multiple of T_{ga} but is such that the spacecraft is still able to re-encounter the gravity-assist body. The flybys of a non-resonant transfer occur at different locations in the gravity-assist body's orbit. *Backflip transfers* (also referred to as *pi-transfers*), are a special case of a non-resonant transfer where the two flybys occur half a rev apart in the gravity-assist body's orbit. Because of the locations of the flybys, both resonant transfers and backflip transfers may be inclined, but non-resonant transfers must be in the plane of the gravity-assist body's orbit.

Compared to non-resonant and backflip transfers, resonant transfers are simple to analyze, as their period is simply $(N/M)T_{ga}$, where N is the number of gravity-assist body revs, and M is the number of spacecraft revs. Because of this, a special kind of tour called *resonance hopping* [8] is often used to estimate how quickly a given gravity-assist body can change the spacecraft's orbit around a central body. For a

set of resonant transfers, labeled N:M , the flight time of a resonance hopping tour is simply the sum of the N's for each resonant orbit multiplied by T_{ga}. A gravity-assist body with strong gravity can hop between resonant orbits with low values of N using only a few flybys, while a body with weaker gravity often forces the choice of high N resonances which result in longer flight times.

Figure 4.1 illustrates how a resonance hopping tour may be constructed using Rhea. This figure shows resonant transfers as vertical lines on a plot of orbit resonance (i.e. T_{sc}/T_{ga}) versus flyby v_∞. As flyby v_∞ approaches 0, the spacecraft orbit cannot be much different from the gravity-assist body's orbit and certain resonances become unavailable (hence the cessation of the vertical lines for lower v_∞'s). In Fig. 4.1 it is important to note the gaps around certain low N resonances such as 1:1, 2:1, 1:2, and 3:2. This consequence of the spacing of rational numbers on the number line can make it difficult to find resonance to hop to near these low N resonances.

The shaded area in Fig. 4.1 shows all resonances that can be either reached from a 1:1 resonance or that may reach a 1:1 resonance with a single Rhea flyby of 50 km or higher. The width of this region is determined by the bending from a flyby, which is a function of v_∞ as shown in Eqn. 4.1:

$$\sin\left(\frac{\delta}{2}\right) = \frac{\mu_{ga}}{\mu_{ga} + r_{pfb} v_\infty^2} \tag{4.1}$$

and by the pump angle (α) required for a given resonance. Pump angle is discussed in the next section, and it is also a function of v_∞. For flybys that do not change inclination (i_{sc}), the change in pump angle is simply the bending angle.

From Fig. 4.1, we see that the resonances with the lowest N that can reach a 1:1 are 8:9 and 8:7. To hop between a 1:1 and a 8:9 or 8:7 requites a v_∞ between 0.4 km/s and 0.8 km/s. If the spacecraft v_∞ is out side of this range, a longer transfer with a higher N is required such as a 10:11 or a 12:11.

Figure 4.2 show a similar plot for Titan where the shaded areas represents regions that can hop from or to a 3:4 resonance with a single 850 km flyby. To hop between

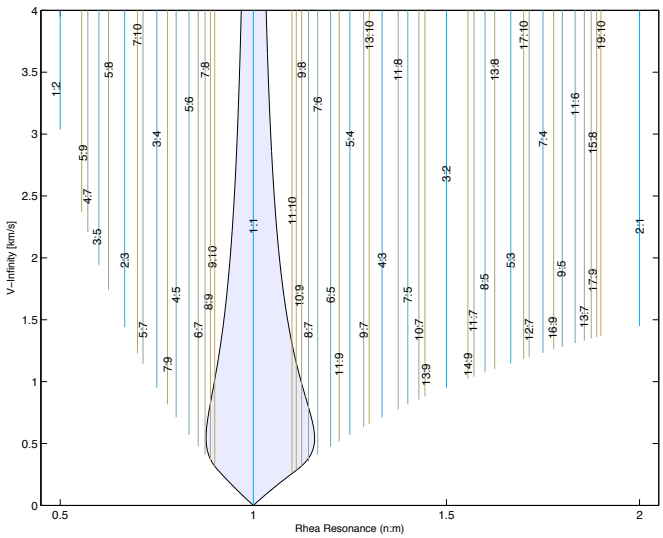

Figure 4.1: Resonances available to/from 1:1 Rhea resonance with 50 km flyby

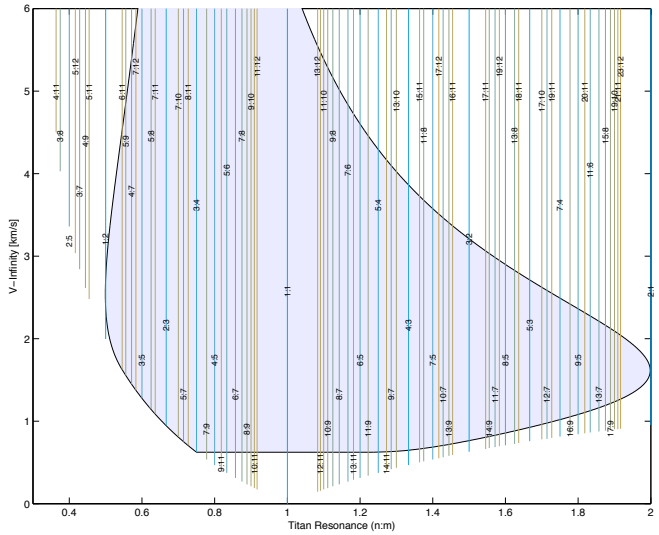

Figure 4.2: Resonances available to/from 3:4 Titan resonance with 850 km flyby

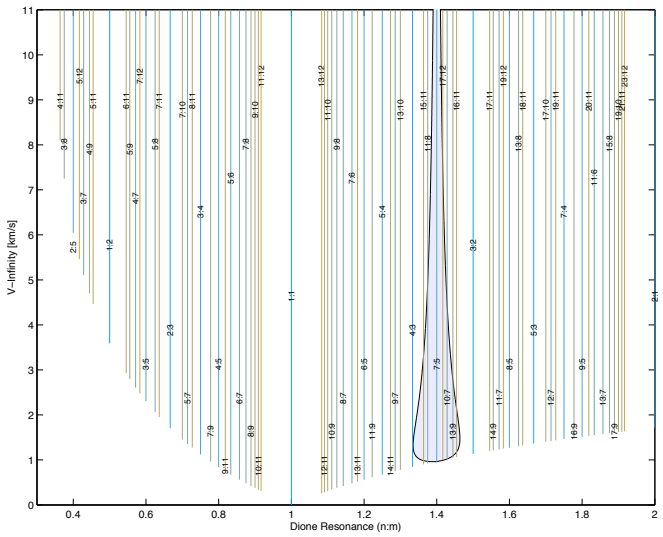

Figure 4.3: Resonances available to/from 7:5 Dione resonance with 50 km flyby

a 2:1 and a 3:4 requires a v_∞ of ∼1.6 km/s, and to hop between 1:2 and 3:4 requires a v_∞ between ∼2.4 and ∼2.7 km/s. This means that a Titan resonance hoping tour from 2:1 to 3:4 to 1:2 would require changing the spacecraft v_∞. For Titan, where the shaded region covers most of the plot, it is probably better to choose a different sequence of resonances that don't require a change in v_∞. However, for smaller moons where the shaded area is much smaller, changing the choice of resonances may be a larger penalty. Consider Fig. 4.3, which shows hopping from or to a 7:5 resonance with a 50 km flyby. For a v_∞ of ∼1.3 km/s a hop from 7:5 to 4:3 is possible. But without this v_∞, the hop must be to 11:8 and then 4:3, a flight time difference of 11 Dione revs (30 days). Being able to modulate the spacecraft v_∞ to make efficient resonance hops would enable savings in flight time at many such places in a tour. This is the motivation for the development of non-tangent VILTs that is discussed in the following sections.

4.1.2 Phase-Free Leveraging

To simplify the analysis, we may assume that the leveraging maneuver occurs at an apse and is tangent to the orbital velocity. The maneuver will be at apoapsis for exterior leveraging and at periapsis for interior leveraging. This assumption limits the effect of the leveraging maneuver to changing an orbit's eccentricity and does not rotate the orbit. I will also assume that leveraging transfers are in the plane of the gravity-assist body's orbit (i.e. $i_{sc} = 0$).

If we introduce k_{ei} as a constant that is $+1$ for exterior leveraging and -1 for interior leveraging, we can write the radius of the apse where the leveraging maneuver occurs, the *leveraging apse*, r_{la} as:

$$r_{la} = a_{sc}(1 + k_{ei}e_{sc}) \tag{4.2}$$

which can be solved for eccentricity:

$$e_{sc} = k_{ei}\left(\frac{r_{la}}{a_{sc}} - 1\right) \tag{4.3}$$

and then substituted into Eqn. 2.130 to yield a quadratic in r_{la} and a_{sc} (where C_{Tiss} is a function of v_∞ given by $C_{Tiss} = 3 - \left(\frac{v_\infty}{v_c}\right)^2$:

$$4a_{sc}r_{la}^2 - 8a_{sc}^2 r_{la} + a_{sc}^2 C_{Tiss}^2 - 2a_{sc}C_{Tiss} + 1 = 0 \tag{4.4}$$

This quadratic then yields two roots for r_{la}. One corresponding to $r_{la} > a_{sc}$ (i.e. r_{la} at apoapsis) and the other to $r_{la} < a_{sc}$ (i.e. r_{la} at periapsis). Therefore r_{la} for a given a_{sc} and v_∞ is:

$$r_{dv} = a_{sc} + k_{ei}\sqrt{a_{sc}^2 - \frac{1}{4}a_{sc}(3 - v_\infty^2)^2 + \frac{1}{2}(3 - v_\infty^2) - \frac{1}{4a_{sc}}} \tag{4.5}$$

We now can start with a v'_∞ before the leveraging maneuver and compute r_{la} as a function of a'_{sc} or T'_{sc} or α' of the pre-maneuver orbit. For the post maneuver orbit,

r_{la} stays the same and we can either use Eqn. 4.3 and Eqn. 2.65 to compute v''_∞ as a function of a given a''_{sc} or use Eqn. 4.4 to compute a''_{sc} from v''_∞ . However, another approach is to specify the radius of the apse without the maneuver, i.e. the *vacant apse*, r_{va}:

$$r_{va} = 2a_{sc} - r_{la} \tag{4.6}$$

If r_{la} and r''_{va} are known, we may use Eqn. 4.6 to solve for a''_{sc} and v''_∞ from Eqn. 2.65. If $r'_{va} = r''_{va}$ there is no leveraging maneuver and the transfer is ballistic. If either r'_{va} or r''_{va} are equal to one, we have the case of tangent leveraging.

After we have solved for a'_{sc} and a''_{sc}, the ΔV of the leveraging transfer is given by:

$$\Delta V = \left| \sqrt{\frac{2}{r_{la}} - \frac{1}{a'_{sc}}} - \sqrt{\frac{2}{r_{la}} - \frac{1}{a''_{sc}}} \right| \tag{4.7}$$

We now can calculate phase-free VILTs specified by a parameter before the VILT: $\{v'_\infty$ or $r'_{va}\}$, a parameter after the VILT: $\{v''_\infty, r''_{va}\}$, and a free parameter: $\{r_{la}, a'_{sc}, T'_{sc},$ or $\alpha'\}$. These VILTs are phase-free because we have not yet enforced a constraint that the VILT must encounter the gravity-assist body both before and after the leveraging maneuver. Adding this constraint will allow us to specify a VILT by a combination of spacecraft and gravity-assist body revs for a transfer instead of $\{r_{la}, a'_{sc}, T'_{sc},$ or $\alpha'\}$.

4.1.3 Leveraging Returns

In order to have a VILT return to the gravity-assist body, we must match the flight time of the spacecraft transfer ($t_{trans;sc}$) with the time that it takes the gravity-assist body to travel between the encounter locations ($t_{trans;ga}$). We must also realize that VILTs can correspond to various numbers of gravity-assist body revolutions, various numbers of spacecraft revolutions, and that the maneuver could occur on any of the spacecraft orbit revs. In addition, the flybys on either end of a VILT can either be

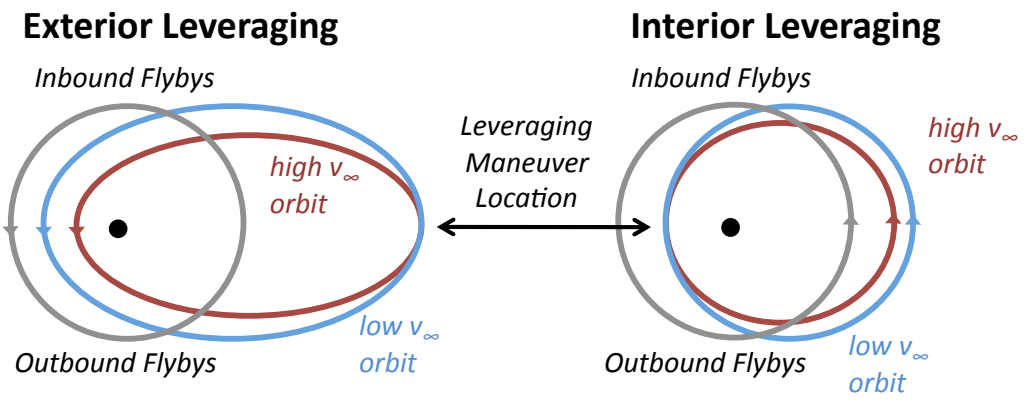

Figure 4.4: Leveraging with Inbound and Outbound flybys

inbound (i.e. before periapsis) or *outbound* (i.e. after periapsis) as shown in Fig. 4.4. As shown in Fig. 4.4, both exterior and interior VILTs may be inbound to outbound (IO), inbound to inbound (II), outbound to inbound (OI), or outbound to outbound (OO). For the case where there is no ΔV , IO and OI VILTs become ballistic non-resonant transfers, and II and OO VILTs become ballistic resonant transfers.

For each of the 8 types of VILTs that may be derived from Fig. 4.4 (i.e. {interior or exterior} and {IO,II,OI, or OO}), there are solutions for various combinations of gravity-assist body integer revs (N), spacecraft integer revs (M), and the spacecraft rev number of the maneuver (L_m). To denote these different cases we will use a modified versions the naming convention of Sims et al. [14]:

$$\{\text{int or ext}\}\text{-}\{\text{IO,II,OI, or OO}\}\ N{:}M(L_m) \tag{4.8}$$

Examples of this naming convention would be: int-OI 2:3(1), ext-OO 1:1(0), int-IO 0:0(0), ext-II 12:11(7), etc.

We can enforce the return constraint by matching the flight time between flyby locations of the spacecraft ($t_{trans;sc}$) to that of the gravity-assist body ($t_{trans;ga}$). To find $t_{trans;sc}$ we start by solving for the eccentric anomaly:[1]

$$E_{sc} = k_{io} \cos^{-1}\left(\frac{a_{sc}-1}{e_{sc}a_{sc}}\right) \tag{4.9}$$

where $k_{io} = \text{sign}(f_{enc})$ is $+1$ for an outbound encounter and -1 for an inbound encounter. From E_{sc} we can now get the time from periapsis of the encounter in the spacecraft's orbit (where $T_{sc} = (a_{sc})^{3/2}$):

$$\tau_{sc} = \frac{T_{sc}}{2\pi}\left(E_{sc} - e_{sc}\sin(E_{sc})\right) \tag{4.10}$$

By thoughtful inspection of Fig. 4.4 we can derive the following relations for $t_{trans;sc}$ for the 8 kinds of VILTs:[2]

exterior: IO,II, or OO $$t_{trans;sc} = (\tau''_{sc} - \tau'_{sc}) + T'_{sc}(L_m + 1/2) + T''_{sc}(M - L_m - 1/2) \tag{4.11}$$

exterior: OI $$t_{trans;sc} = (\tau''_{sc} - \tau'_{sc}) + T'_{sc}(L_m + 1/2) + T''_{sc}(M - L_m + 1/2) \tag{4.12}$$

interior: O,II, or OO $$t_{trans;sc} = (\tau''_{sc} - \tau'_{sc}) + T'_{sc}L_m + T''_{sc}(M - L_m) \tag{4.13}$$

interior: OI $$t_{trans;sc} = (\tau''_{sc} - \tau'_{sc}) + T'_{sc}L_m + T''_{sc}(M - L_m + 1) \tag{4.14}$$

By using k_{ei} and M_a we can simplify the four equations above into one equation:

$$t_{trans;sc} = \tau''_{sc} - \tau'_{sc} + T'_{sc}\left(L_m + \frac{1+k_{ei}}{4}\right) + T''_{sc}\left(M_a - L_m - \frac{1+k_{ei}}{4}\right) \tag{4.15}$$

[1]For the one hyperbolic VILT, an $M = 0$ IO transfer, the analogous equations for hyperbolic anomaly would have to be used instead of Eqn. 4.9 and Eqn. 4.10.
[2]Remember that τ_{sc} has the same sign as k_{io}.

where M_a is the number of spacecraft revs counted by apoapsis crossings and is related to M as follows:

$$M_a = \begin{cases} M & \text{if IO,II, or OO} \\ M+1 & \text{if OI} \end{cases} \tag{4.16}$$

Equation 4.15 accounts for the time of flight of the spacecraft. The next part is to account for the time of flight of the gravity-assist body. Since we have assumed the gravity-assist body to be in a circular orbit we can find its flight time from the angle between the two encounters. The true anomaly of each encounter is given by:

$$f_{sc} = k_{io} \cos^{-1}\left(\frac{1}{e_{sc}}(a_{sc}(1-{e_{sc}}^2)-1)\right) \tag{4.17}$$

Then the flight time of the gravity assist body is:

$$t_{trans;ga} = N_a + \frac{1}{2\pi}(f''_{sc} - f'_{sc}) \tag{4.18}$$

where, like M_a, N_a is introduced to cover the OI case. Here N_a is the number of times that the gravity-assist body crosses the line between the central body and spacecraft apoapsis. N_a is given by:

$$N_a = \begin{cases} N & \text{if IO,II, or OO} \\ N+1 & \text{if OI} \end{cases} \tag{4.19}$$

Since we need to use Kepler's equation to get $t_{trans;sc}$ we cannot start from the constraint $t_{trans;sc} = t_{trans;ga}$ and work backwards to find the VILT. Rather we have to iteratively guess phase-free VILTs until this constraint is met. We do this by guessing one of the free parameters of the phase free problem, $\{r_{la}, a'_{sc}, T'_{sc}$, or $\alpha'\}$, and iterating to find the value where:

$$t_{trans;sc} = t_{trans;ga} \tag{4.20}$$

Each of the solutions to Eqn. 4.20 gives a VILT specified by the naming convention in Eqn. 4.8.

4.1.4 Tisserand Graph of Non-Tangent Leveraging

A *Tisserand Graph* [18, 23, 24, 37] may be used to better understand how VILTs help us change the central body orbits we can access from flybys. It can also help us see the family of VILTs specified by Eqn. 4.8. Figure 4.5 is an example of such a Tisserand graph.

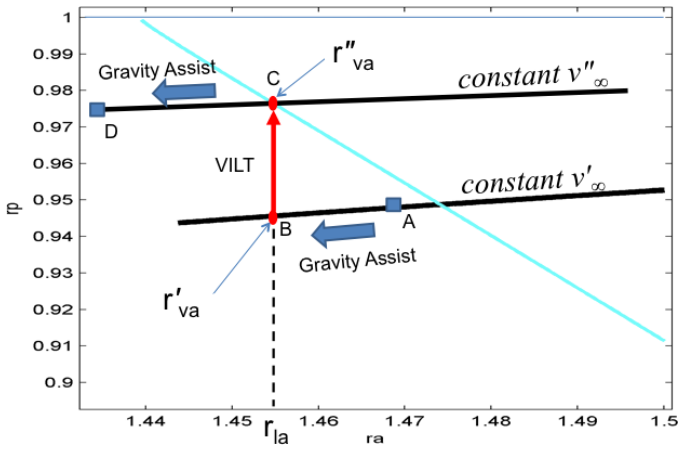

Figure 4.5: Example of external VILT

Figure 4.5 is a Tisserand Graph showing apoapsis radius (r_a) versus periapsis radius (r_p). Each point on the graph represents an orbit around the central body. Since Tisserand's criterion remains constant through flybys, we may plot contours with constant values of Tisserand's criterion or v_∞ ($C_{Tiss} = 3 - v_\infty^2$) to represent how flybys can change the orbit with respect to the central body. We may also plot other contours to show how VILTs change the orbit with respect to the central body, and by comparison with the C_{Tiss} or v_∞ contours we may also see how the VILTs change the flyby v_∞. In Fig. 4.5, the VILT is shown connecting the orbit before the leveraging maneuver with v'_∞ and r'_{va} to the orbit after the leveraging maneuver with v''_∞ and r''_{va}, resulting in a reduction in v_∞. Since for exterior leveraging the apoapsis

radius (i.e. $r_{la} = r_a$) doesn't change during the maneuver, the VILT follows a line of constant apoapsis on this Tisserand graph. The light blue line represents other VILTs that could go to different values of v''_∞ and r''_{va}.

In Fig. 4.5, a gravity assist goes from the spacecraft orbit at point A to the orbit at point B. The VILT then goes from the orbit at point B to the orbit at point C, which then re-encounters the gravity-assist body. Finally another flyby changes the spacecraft orbit from point C to point D. This orbit at point D could be the start of another VILT, a ballistic transfer, a transfer to another moon, or just an orbit around the central body that is not intended to return to the gravity-assist body. In this manner we may depict the sequence of VILTs and ballistic transfers in a gravity-assist tour on a Tisserand graph to show both how the flyby v_∞ changes as well as the orbit around the central body.

Notice in Fig. 4.5, that if the VILT were to go to another point on the VILT's blue line with a v_∞ between v''_∞ and c'_∞, point B would have to move to the right so that it could be connected to the blue line with a constant r_a, and less bending would be needed by the flyby from A to B. The point where the blue line crosses the v'_∞ contour is a ballistic transfer. Between this point and point A are VILTs that require less bending than the ballistic transfer. These VILTs are important when we construct tours with low mass moons than cannot provide much bending. Even if we do not have enough bending to reach a desired ballistic non-resonant or resonant transfer, there may be a related VILT that we could reach. In the case shown, these low-bending VILTs decrease v_∞. However, if our starting point were further right on the v'_∞ contour, these low-bending VILTs would increase v_∞.

4.2 Example Leveraging Tour to Enceladus

We may now use the techniques in the previous sections to design an example *leveraging tour* (i.e. a tour with VILTs) that starts from a Saturn arrival condition similar to that of the Titan Saturn System Mission (TSSM) study [38] and reaches

Enceladus orbit. This tour is intended to be an example of how leveraging techniques can improve upon the Enceladus orbit insertion from a direct Titan to Enceladus transfer and is not intended to represent an optimal solution to the problem. I do not wish to tie this example solution to a specific epoch and will not consider the phasing of the transfer orbits between the moons. Neglecting these transfer orbits will add a small amount of additional flight time to our estimates (on the order of a few revs of the moons involved). However, the additional ΔV from these transfers will be negligible as these transfers would be pretty much ballistic.

Table 4.1: Initial Saturn Orbit

TSSM SOI	746 m/s	Initial r_p	1.2 R_S
Pre-SOI Mass	5814 kg	Initial r_a	200 R_S
Flight Time to SOI	9 yrs	Initial T_{sc}	180 days

Table 4.1 gives the Saturn arrival conditions for the TSSM study. [38] We will use this as a starting point for designing our trajectory to Enceladus and for comparison with other methods. On arrival at Saturn, the TSSM mission uses a 746 m/s Saturn Orbit Insertion (SOI) maneuver to enter an initial 1.2 Saturn radii by 200 Saturn radii orbit. From this orbit, we use a 564 m/s Periapsis Raise Maneuver (PRM) to raise the periapsis to Titan's orbit and achieve a v_∞ of 1.46 km/s. Table 4.2 shows the three flybys and one leveraging maneuver used to transition from this orbit to a Titan-Rhea Hohmann transfer. Figure 4.6 shows these flybys and the leveraging on a Tisserand graph.

Table 4.3 and Fig. 4.7 show the 14 Rhea flybys and 8 leveraging maneuvers needed to get from the Titan-Rhea Hohmann to the Rhea-Dione Hohmann. This sequence of VILTs and ballistic transfers requires 9.5 months and 251 m/s. The minimum flyby altitude allowed for Rhea (as well as Dione and Tethys) is 50 km. Some of these encounters are very close in time from an operational perspective, and a future mission's ground system may not be able to handle flybys closer than 9 days. However, for this

Table 4.2: Titan Transfers

Flyby	t_{trans} [d]	Altitude [km]	Transfer Type N:M(L)	v'_∞ [km/s]	v''_∞ [km/s]	ΔV [m/s]
Titan-1	61.3	2290	ext-OI 2:1(0)	1.46	1.27	27.4
Titan-2	21.3	3010	OI 1:1	1.27	1.27	0.0
Titan-3	—	15220	*transfer to Rhea*			

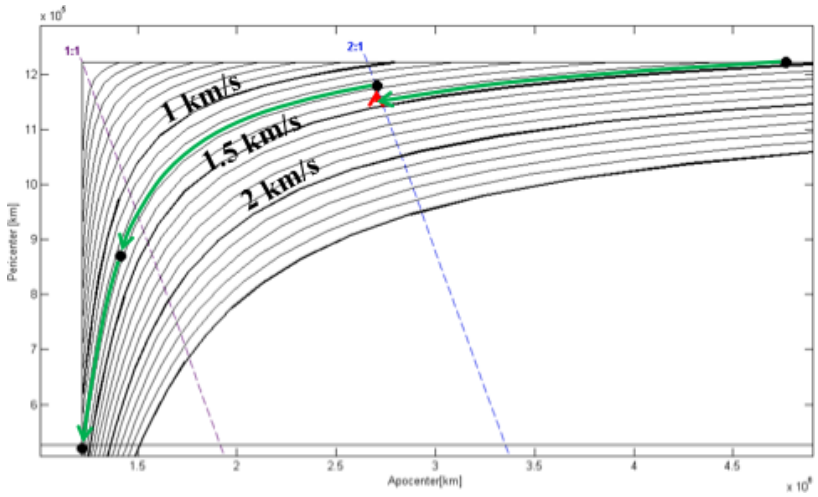

Figure 4.6: Titan leveraging

example, I chose to design a tour without presupposing any particular constraints from the ground system with the assumption that such a tour could be modified by adding transfers with multiple spacecraft revs if needed (e.g. 1:1 transfers could be replaced with 2:2 or 3:3 transfers).

In Table 4.3, flybys Rhea-3 and Rhea-9 are particularly interesting in that they increase v_∞. If the goal of this sequence of flybys is to lower v_∞ from the initial 1.75 km/s to near the Rhea-Dione Hohmann's 0.73 km/s, why is ΔV used to increase v_∞? The answer can be found in the earlier discussion of Fig. 4.5; v_∞ was increased in order to reach a low flight time VILT. The flybys before the VILT were already at or near the 50 km limit and could not provide enough bending to reach the ballistic transfer. By increasing v_∞, less bending was needed to reach the desired VILT.

The Dione transfers are shown in Table 4.4 and Fig. 4.8, taking 3.5 months and 90 m/s. The Tethys transfers in Table 4.5 and Fig. 4.9 then go from Dione to Enceladus in 4.5 months with 28 m/s. Finally, in Table 4.6 and Fig. 4.10, 4.5 months and 96 m/s of Enceladus leveraging is used to reduce the Enceladus v_∞ from 800 m/s to 300 m/s. Due to Enceladus' small mass, we allowed the minimum flyby altitude during this segment to decrease to 40 km initially and then to 25 km at the end. Although we believe that such low flybys should be possible at Enceladus, a future project may find it preferable to do orbit insertion from a higher v_∞ rather than develop a flight system and ground system capable of such low flybys.

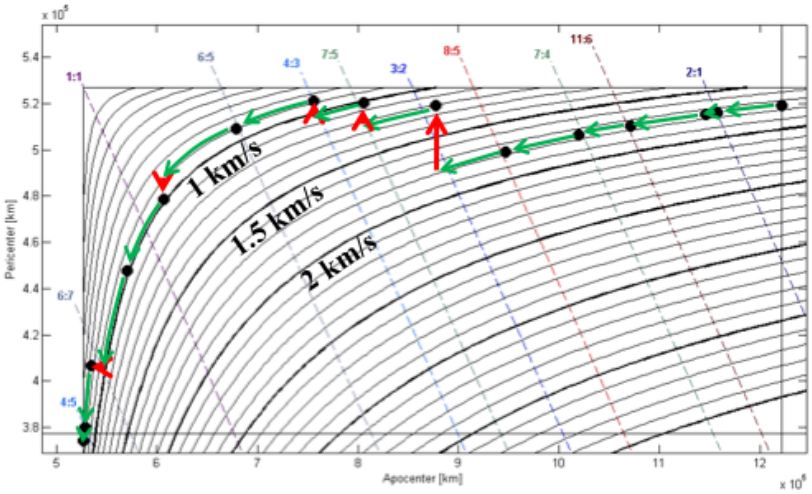

Figure 4.7: Rhea leveraging

Table 4.7 shows the combined ΔV of these transfers along with the TSSM SOI ΔV and a PRM ΔV calculated from the TSSM initial orbit. The Enceladus orbit insertion is calculated with a 10% estimate of gravity losses. Tour statistical ΔV is estimated at 5 m/s per flyby. The table also shows ΔV totals for two alternate strategies for reaching Enceladus: inserting directly from a Titan-Enceladus Hohmann, and inserting directly from the initial TSSM orbit. The ΔV for each strategy is then used with the TSSM bi-prop I_{sp} of 323 sec. to calculate a mass inserted into Enceladus orbit assuming the TSSM Saturn arrival mass of 5814 kg. From Enceladus orbit, the spacecraft may use additional ΔV for orbit maintenance, orbit changes, and/or

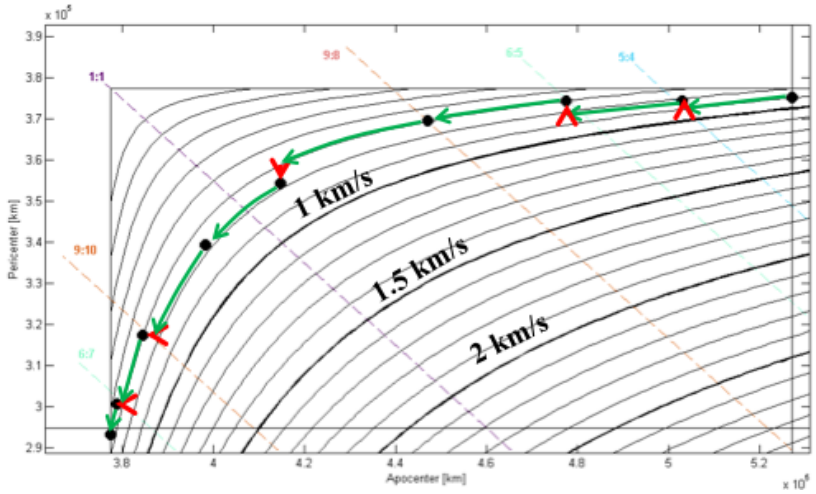

Figure 4.8: Dione leveraging

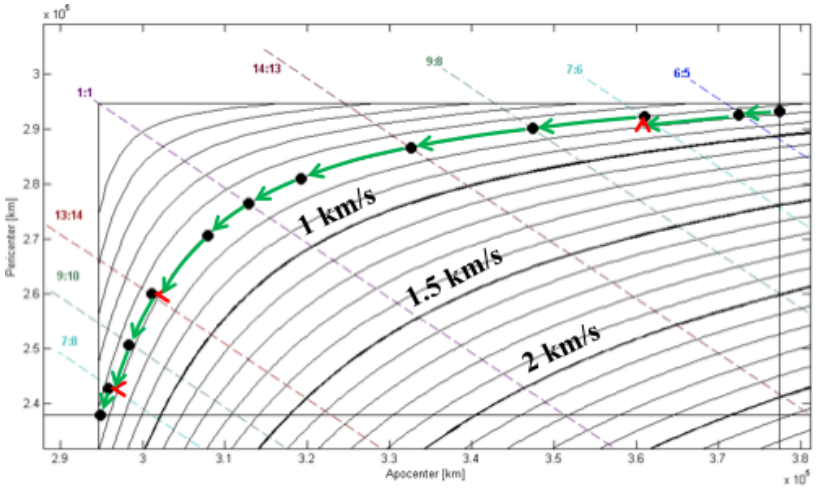

Figure 4.9: Tethys leveraging

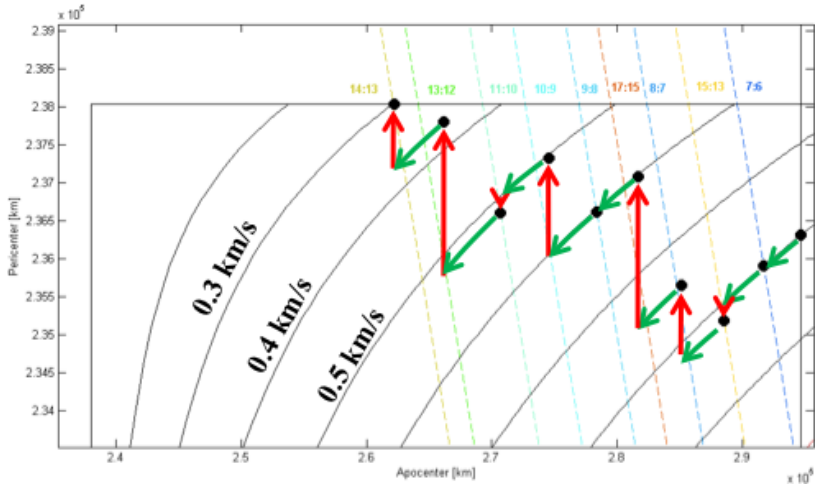

Figure 4.10: Enceladus leveraging

Table 4.3: Rhea Transfers

Flyby	t_{trans} [d]	Altitude [km]	Transfer Type N:M(L)	v'_∞ [km/s]	v''_∞ [km/s]	ΔV [m/s]
Rhea-1	17.6	140	OI 2:1	1.75	1.75	0.0
Rhea-2	17.4	4910	OI 2:1	1.75	1.75	0.0
Rhea-3	50.4	50	ext-IO 11:6(2)	1.75	1.76	1.4
Rhea-4	38.7	470	OI 7:4	1.76	1.76	0.0
Rhea-5	37.1	50	ext-IO 8:5(4)	1.76	1.77	2.0
Rhea-6	19.6	60	ext-OI 3:2(1)	1.77	1.21	99.1
Rhea-7	37.4	50	ext-OI 7:5(4)	1.21	1.02	29.7
Rhea-8	23.5	510	ext-OI 4:3(0)	1.02	0.88	24.1
Rhea-9	31.4	50	ext-OI 6:5(0)	0.88	0.90	5.0
Rhea-10	6.5	60	ext-IO 1:1(0)	0.90	0.99	35.7
Rhea-11	6.2	240	OI 1:1	0.99	0.99	0.0
Rhea-12	30.1	80	int-IO 6:7(5)	0.99	0.75	53.6
Rhea-13	21.4	200	IO 4:5	0.75	0.75	0.0
Rhea-14	—	6990	*transfer to Dione*			

Table 4.4: Dione Transfers

Flyby	t_{trans} [d]	Altitude [km]	Transfer Type N:M(L)	v'_∞ [km/s]	v''_∞ [km/s]	ΔV [m/s]
Dione-1	16.8	100	ext-OI 5:4(3)	0.90	0.82	12.0
Dione-2	19.3	160	ext-OI 6:5(0)	0.82	0.70	21.5
Dione-3	25.2	110	IO 9:8	0.70	0.70	0.0
Dione-4	3.9	60	ext-IO 1:1(0)	0.70	0.77	30.4
Dione-5	3.8	220	OI 1:1	0.77	0.77	0.0
Dione-6	26.5	50	int-IO 9:10(9)	0.77	0.70	17.9
Dione-7	16.7	180	int-OI 6:7(6)	0.70	0.65	8.4
Dione-8	—	970	*transfer to Tethys*			

Table 4.5: Tethys Transfers

Flyby	t_{trans} [d]	Altitude [km]	Transfer Type N:M(L)	v'_∞ [km/s]	v''_∞ [km/s]	ΔV [m/s]
Tethys-1	13.4	790	OI 6:5	0.77	0.77	0.0
Tethys-2	13.5	110	ext-IO 7:6(0)	0.77	0.70	12.1
Tethys-3	17.3	60	IO 9:8	0.70	0.70	0.0
Tethys-4	27.0	50	IO 14:13	0.70	0.70	0.0
Tethys-5	2.7	50	IO 1:1	0.70	0.70	0.0
Tethys-6	2.9	510	OI 1:1	0.70	0.70	0.0
Tethys-7	2.6	480	OI 1:1	0.70	0.70	0.0
Tethys-8	25.8	50	int-IO 13:14(2)	0.70	0.67	10.3
Tethys-9	17.3	150	OI 9:10	0.67	0.67	0.0
Tethys-10	14.7	130	int-IO 7:8(7)	0.67	0.63	5.3
Tethys-11	—	270	*transfer to Enceladus*			

Table 4.6: Enceladus Transfers

Flyby	t_{trans} [d]	Altitude [km]	Transfer Type N:M(L)	v'_∞ [km/s]	v''_∞ [km/s]	ΔV [m/s]
Enceladus-1	11.0	40	OI 7:6	0.80	0.80	0.0
Enceladus-2	21.9	30	ext-OI 15:13(3)	0.80	0.82	3.2
Enceladus-3	12.3	40	ext-OI 8:7(5)	0.82	0.75	13.1
Enceladus-4	23.5	40	ext-IO 17:15(8)	0.75	0.60	25.5
Enceladus-5	13.7	40	OI 9:8	0.60	0.60	0.0
Enceladus-6	15.1	40	ext-OI 10:9(8)	0.60	0.50	16.6
Enceladus-7	16.4	30	ext-OI 11:10(0)	0.50	0.52	2.0
Enceladus-8	19.2	30	ext-OI 13:12(11)	0.52	0.37	25.6
Enceladus-9	20.6	25	ext-OI 14:13(1)	0.37	0.30	10.4

Table 4.7: Delta-V Comparison

	Leveraging Tour	Titan-Encel.	SOI-Encel.
SOI [m/s]	746	746	746
PRM [m/s]	564	546	159
Titan Leveraging [m/s]	27	—	—
Rhea Leveraging [m/s]	251	—	—
Dione Leveraging [m/s]	90	—	—
Tethys Leveraging [m/s]	28	—	—
Encel. Leveraging [m/s]	96	—	—
Tour Statistical ΔV Est. [m/s]	225	20	—
Encel. Orbit Insertion [m/s]	242	3,933	5,380
Total ΔV [m/s]	2,269	5,245	6,285
Encel. On-Orbit Mass [kg]	2,839	1,109	798
TOF from SOI [yr]	$\sim$3	$\sim$0.8	$\sim$0.5

for landing on Enceladus, but this ΔV is not accounted for in this analysis. Finally, for each strategy, an approximate flight time is estimated that does not account for phasing orbits that may be needed to transfer between the moons.

This example leveraging tour places allows an Enceladus orbiter 2.5$\times$ of the mass of the Titan-Enceladus Hohmann trajectory and 3.5$\times$ of the mass of a direct insertion after SOI. It does this with an increase of flight time to 3 years. Assuming a 9 year flight time to Saturn like the TSSM trajectory, that would leave a mission with up to 3 years at Enceladus before reaching the 15 year spacecraft design lifetime typical for outer planet missions. With longer flight time also comes exciting science from 14 Rhea flybys, 8 Dione Flyby, and 11 Tethys flybys, all of which are at much lower Encounters speeds than the handful of Cassini flybys of these bodies. Furthermore, this is just one example tour and other tours exist with different combinations of flight time and ΔV [39].

CHAPTER 5. ASTEROID REDIRECTION

NASA's Asteroid Redirect Mission (ARM) [26, 27, 40, 41] study initially considered two mission scenarios: redirection of a small ($<\sim$12 m) asteroid into a Lunar Distant Retrograde Orbit (DRO) or retrieval of a 2-3 m boulder from a larger asteroid and bringing that into the same Lunar DRO [42]. The techniques in this chapter are applicable to the first ARM scenario: redirection of an entire asteroid. Although NASA chose the second scenario for ARM in 2015, the redirection of an entire asteroid is still a very interesting problem in astrodynamics.

Various concepts for asteroid capture or redirection have been studied over the years, [43–49] but have not been feasible with current technology. However, a 2011 study [26, 27] by the Keck Institute for Space Studies (KISS) showed that it is now possible to capture a small (but large enough to be detected) asteroid and place it into Earth or Lunar orbit using recent developments in high-power Solar Electric Propulsion (SEP) technology, upgrades to NASA's asteroid detection system, and new astrodynamics techniques. [40, 41] NASA's current ARM concept derives from this study. In addition, work in the NASA ARM study and in a second 2014 KISS study on asteroid redirection technology found that the technologies developed by ARM could also be applied to redirect asteroids onto useful heliocentric orbits such as Earth-Mars cyclers and Earth backflip orbits. This chapter will present the dynamical criteria that can be used to identify which asteroids could be redirected into the Earth-Moon system or onto other heliocentric orbits for relatively low ΔV ($<\sim$200 m/s).

5.1 The Asteroid Redirection Mission Concept

The ARM concept is intended as a pathfinder mission for human interplanetary spaceflight. ARM consists of an Asteroid Redirect Robotic Mission (ARRM) and

an Asteroid Redirect Crew Mission (ARCM). In the entire asteroid redirection case, ARRM would place an asteroid into lunar orbit where it will be visited by the ARCM, the first of a series of Lunar "Proving Ground" missions that would develop the operational methods and life support systems for interplanetary flight. The ARRM vehicle would use a 40 kW SEP system that could be readily scaled up to the 100-200 kW power levels that would be needed by human Mars missions. [50, 51]

Figure 5.1 shows the timeline for the ARRM small asteroid option. [41] The ARRM vehicle could launch on an SLS, Falcon Heavy, Atlas V, or Delta IV Heavy. If launched on an Altas V, a low thrust spiral would be used to reach the Moon. Other launch vehicles allow direct launch to a Lunar Gravity Assist (LGA) that would inject the vehicle onto an interplanetary trajectory to the asteroid to be redirected. This asteroid would be chosen because it has a natural Earth close approach in the desired time frame (2023-2024) that could be redirected to a Lunar Gravity Assist (LGA) that would capture the asteroid.

The ARV would use SEP to reach the asteroid and rendezvous with it. At the asteroid, it would capture the asteroid in a large inflatable bag designed to contain the asteroid if it is a rubble pile or otherwise has low cohesion. The SEP system would then be used to redirect the asteroid and to target an LGA that would capture the asteroid into a loose Earth orbit. From there, solar perturbations and a second LGA would be used to place the asteroid into a Lunar Distant Retrograde Orbit (DRO). This initial DRO would only have a lifetime of a year or two, but small maneuvers ($<$ 30m/s) with the SEP system over several months could be used to move the asteroid into a DRO with a lifetime of several hundred years. [41]

Alternate Redirection Technologies

The capture system design for the ARM small asteroid redirection mission scenario was to deploy a 12-15 m inflatable bag which would surround the asteroid and then be drawn tight to the asteroid to anchor the spacecraft to the asteroid. The spacecraft

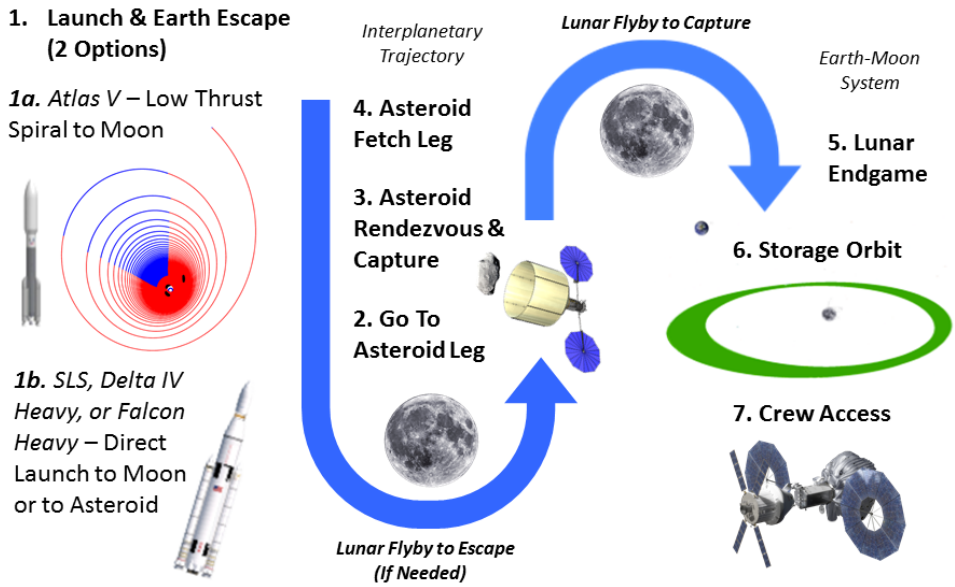

Figure 5.1: Mission timeline for ARM small asteroid redirection concept

would use its monopropellant reaction control system to de-spin the asteroid and rotate it to the proper attitude for thrusting. It would then use the SEP system to apply the redirection ΔV to the asteroid.

Although this system works for small asteroids, it is not likely scalable to much larger asteroids because larger bag sizes are difficult to test on the ground, and the propellant needed to de-spin a larger asteroid could be prohibitive. Therefore, a successor to the ARM vehicle may employ new methods to redirect larger asteroids. Two promising technologies that could allow redirection of an asteroid without contact with the surface or the need to de-spin the asteroid are ion beam deflection [52] and laser ablation. [53] Ion beam deflection applies impulse to an asteroid by impinging the plume from an electric thruster on an asteroid and a second propulsion system contracts the thrust on the spacecraft to maintain position relative to the asteroid. For the plume impingement, gridded ion thrusters are preferred because they produce more focused beams than Hall effect thrusters. The technique of laser ablation would impart impulse on an asteroid with a high-power laser that vaporizes spots on the

surface. Although currently a less mature technology than ion beam deflection, laser ablation holds promise as potentially a more efficient way to redirect larger asteroids.

5.2 Asteroid Redirection to Capture

Asteroids with v_∞ magnitude less than 2.1 km/s and a declination less than 15° may be captured by one or more LGAs, provided they can be targeted to the proper Lunar flyby aim-point. For asteroids with higher v_∞ declinations, Earth flybys could be used to lower the declination. For asteroids with higher v_∞ magnitudes, low-thrust double Earth-Moon flybys or v_∞ leveraging could be used to lower the v_∞ magnitude to an acceptable range for capture.

5.2.1 Capture via Lunar Gravity Assist

To capture an asteroid, a Lunar gravity assist is employed to decrease the Earth-relative energy of the return mass from a positive $C_3 < 2\ km^2/s^2$ to a C_3 of around -0.5 km^2/s^2. Figure 5.2 shows the maximum C_3 that could be captured with a single LGA depending on the v_∞ declination and right ascention. A C_3 of 2 km^2/s^2 permits asteroid capture from declinations ranging up to 30° from the ecliptic; [54] direct LGA capture from higher energies may be achievable in special cases of in-plane arrivals

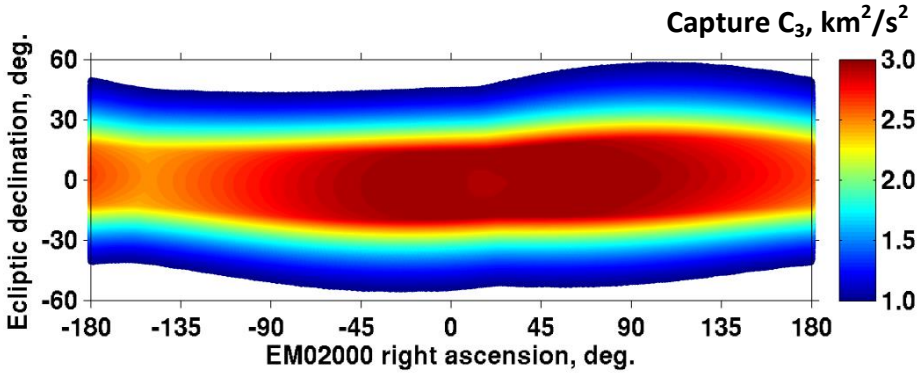

Figure 5.2: Lunar Gravity Assist (LGA) performance [54]

and favorable lunar phase. Multiple LGAs may also allow capture from a C_3 has high as 4 km^2/s^2. [54]

5.2.2 The Dynamical Filter Using Tisserand's Criterion

An asteroid's Tisserand parameter is most nearly the Jacobi constant when the object is farthest from the secondary body (i.e. Earth). If we calculate the Tisserand parameter from the oscillating orbit elements of an asteroid (relative to the Earth-Sun barycenter) when it is farthest from the Earth, we can use Eqn. 2.65 to caluclate a v_∞ for that asteroid that will not change without interaction from other planets or non-gravitational forces. Therefore this v_∞ is a very good predictor of the v_∞ an asteroid would have when it encounters the Earth. This works even if the asteroid does not currently cross the Earth's orbit and would need to follow a low-energy manifold to reach the Earth.

The Tisserand parameter can be graphed [18] as a function of parameters derived from orbit elements (e.g. period and periapsis or periapsis and apoapsis) to design spacecraft trajectories. Campagnola et al. [37] have proposed a Tisserand-Poincaré graph that allows the design of both gravity-assist and low-energy manifold trajectories. Figure 5.3 is such a Tisserand-Poincaré graph applied to the problem of finding asteroids that could be redirected to an LGA capture.

Figure 5.3 shows all known Near Earth Asteroids (NEAs) with a perihelion from 0.7 to 1.1 AU and an aphelion from 0.9 to 1.5 AU. The open red circles represent asteroid estimated to be 15 m or larger and the closed circles represent asteroids smaller than 15 m. The green area shows objects that have a Tisserand parameter corresponding to a v_∞ of 1.8 km/s or less and cross the Earth's orbit. The yellow area shows objects that come close but do not cross the Earth's orbit and have a Tisserand parameter corresponding to a v_∞ of 2.6 km/s or less. The black diagonal lines show the synodic period of the asteroids. Asteroids in the green area could be returned with minimal ΔV to redirect a natural Earth encounter to an LGA. Asteroids in the

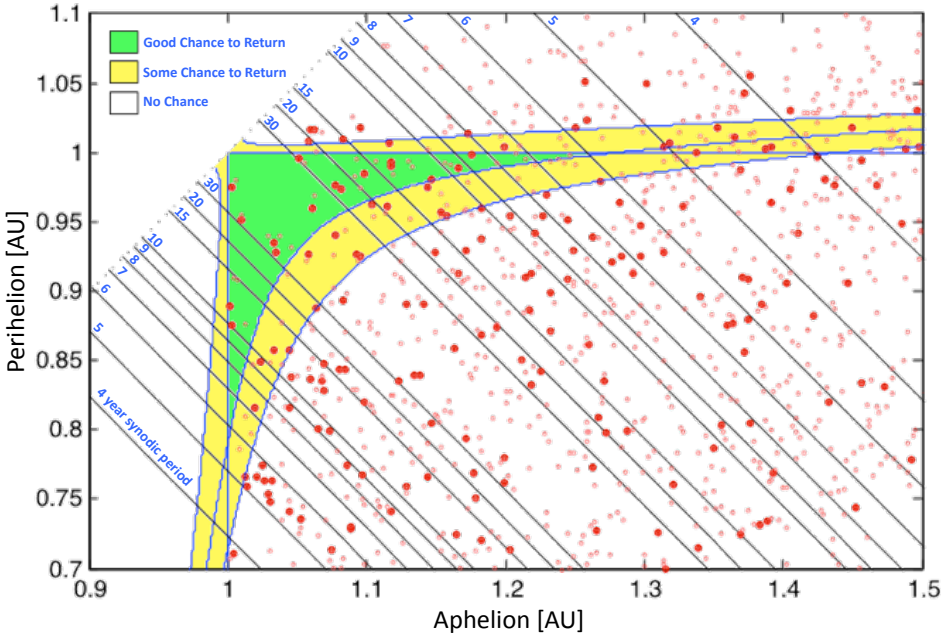

Figure 5.3: Tisserand-Poincaré Graph of redirectable asteroids

yellow area may also be returnable, but would require extra ΔV to either lower their v_∞ or to modify the asteroid orbit so that it has an Earth encounter. Asteroids in the white region either have a v_∞ too high for LGA capture or have orbits that cannot be modified to cross the Earth's without large ΔV.

5.2.3 Redirection of High v_∞ Asteroids

Even if an object naturally encounters Earth with a higher v_∞ than could be captured directly with a lunar gravity, tens or even hundreds of tonnes of asteroid mass could still be captured into orbit. In this case an additional flyby of Earth followed by 1-2 years of thrusting can efficiently lower the Earth-approach C_3 to around 2 km^2/s^2, enabling lunar-assisted capture. Two example trajectories are shown in Fig. 5.4, where 1.5 yr (left) or 2.1 yr (right) of SEP thrusting leverages the C_3 with respect to Earth from 16 km^2/s^2 down to 2 km^2/s^2. The transfer duration

from Earth flyby to lunar capture does not vary significantly for different Earth flyby v_∞.

As indicated by the gold lines in Fig. 5.5, the ΔV to reduce the flyby v_∞ to enable LGA capture is significantly less using an Earth flyby followed by SEP thrusting than attempting to directly reduce the approach velocity. The mass curves in Fig. 5.5 are computed assuming a 5 t spacecraft, 40-kW SEP system (P_0), 90% duty cycle (d), 55% efficiency (η) at 2000 s I_{sp}, or 60% efficiency at 3000 s I_{sp}, and that the return mass is maximized by thrusting during the entire transfer time (t). It is then possible to estimate the maximum return mass via the following equations:

$$m_{prop} = \frac{2\eta d P_0}{(gI_{sp})^2} t \tag{5.1}$$

$$m_{return} = \frac{m_{prop}}{e^{\frac{\Delta V}{gI_{sp}}} - 1} - 5t \tag{5.2}$$

In the case of 4-km/s v_∞ , 2.1 yr flight time, and 3000 s I_{sp}, the ΔV is 1.65 km/s, the propellant mass is 3.30 t and the return mass is 52 t. Equation 5.1 is only an approximation for orbits that remain near 1 AU (such as the leveraging transfers

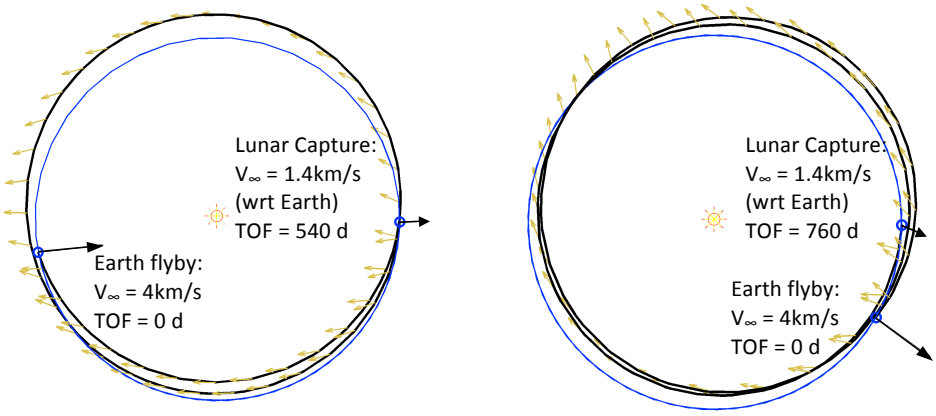

Figure 5.4: Example SEP leveraging sequence

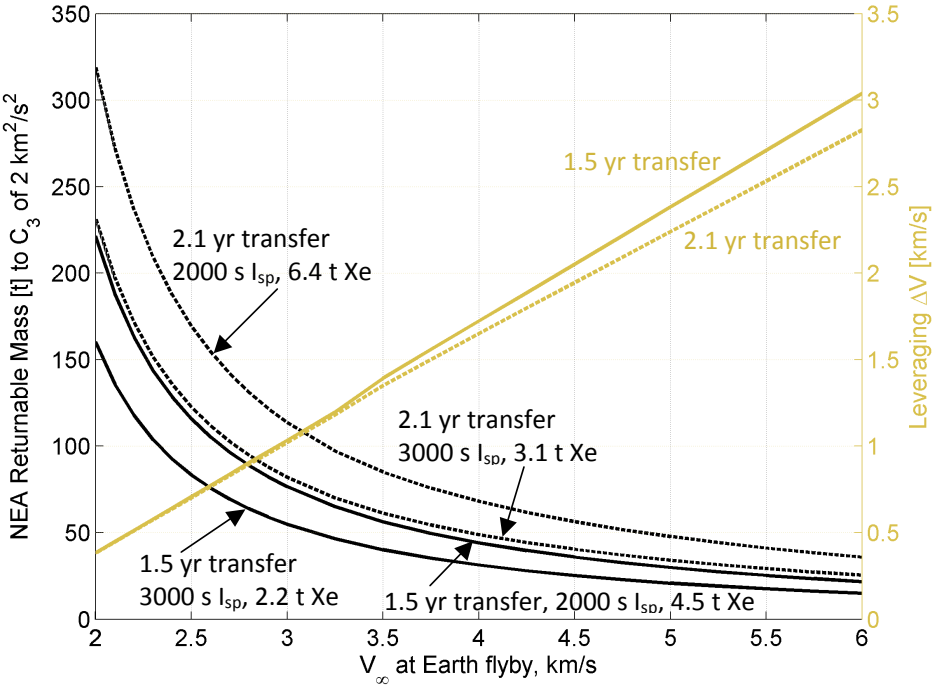

Figure 5.5: SEP leveraging performance

shown in Fig. 5.4), but permits the mass to be estimated for a variety of SEP systems with different P_0 and I_{sp}. In addition, the returnable mass can be estimated for different propellant throughput constraints via Eqn. 5.2.

5.2.4 Asteroids Redirectable to Earth Capture

Of the known NEAs, 32 objects have a v_∞ less than 2.6 km/s as calculated from Eqn. 2.65, perihelion less than 1.03 AU, an aphelion greater than 0.97 AU, and have natural Earth close approaches in the 2020s. Retrieval trajectories for these objects have been calculated and are shown in Table 5.1. This table gives the current best return masses for these asteroids assuming a 40-kW SEP system with 3000 sec Isp and launch on a Delta IV Heavy in 2018. (The trajectory search used to generate this table was not exhaustive, and better trajectories could be found.) In these data, twelve asteroids have been found with return masses greater than 100 t, and six in the

years 2020 through 2026. Three of these have have been characterized (2013 EC20, 2009 BD, and 2011 MD) and have retrievable masses below the return capability. Four asteroids that return after 2025 have future characterization opportunities: 2008 HU4, 2012 TF79, 2012 LA, and 2011 BL45.

Table 5.1: Candidate Asteroids for LGA Capture

Asteroid	Diameter Est.	Asteroid v_∞	Return Mass	Natural Return	Characterization
2007 UN12	4-12 m	1.2 km/s	490 t	9/2020	
2008 EA9	7-20 m	1.9 km/s	130 t	11/2020	
2013 EC20	2-4 m	*2.6 km/s*	120 t	3/2021,11/2026	radar 2013
2010 UE51	5-15 m	1.2 km/s	130 t	10/2022	
2009 BD	3-7 m	1.2 km/s	590 t	6/2023	Spitzer 2013
2011 MD	2-16 m	1.0 km/s	800 t	7/2024	Spitzer 2014
2008 HU4	6-16 m	0.5 km/s	1600 t	4/2026	*radar 2016*
2012 TF79	8-23 m	0.3 km/	170 t	3/2027	*Spitzer 2016*
2006 RH120	3-9 m	1.0 km/s	490 t	10/2028	
2012 LA	8-21 m	1.5 km/s	230 t	5/2029	*Spitzer 2018*
2011 BL45	9-26 m	1.4 km/	1400 t	8/2029	*Spitzer 2015*
2008 UA202	3-9 m	1.9 km/s	310 t	10/2029	

5.2.5 Example Redirection Trajectory

From Table 5.1, asteroid 2009 BD has been characterized [55] to have a mass less than 145 t and, as a result, is an attractive candidate for redirection. Figure 5.6 presents an example trajectory to 2009 BD launching in 2018 and Fig. 5.7 shows an example redirection trajectory with a capture LGA in June 2023. Trajectories to redirect other asteroids in Table 5.1 are very similar. They all involve a < 2 year trajectory to rendezvous with the asteroid followed by a redirection leg that only slightly modifies the asteroid's natural orbit to achieve the LGA target. The Strange et al. paper on the ARM mission design [41] provides more detail on this trajectory.

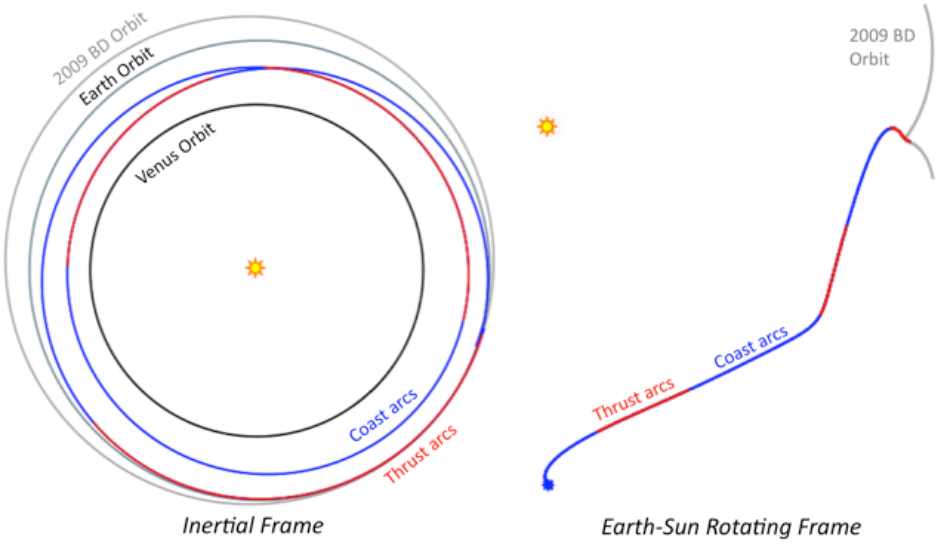

Figure 5.6: ARM "Go To" leg

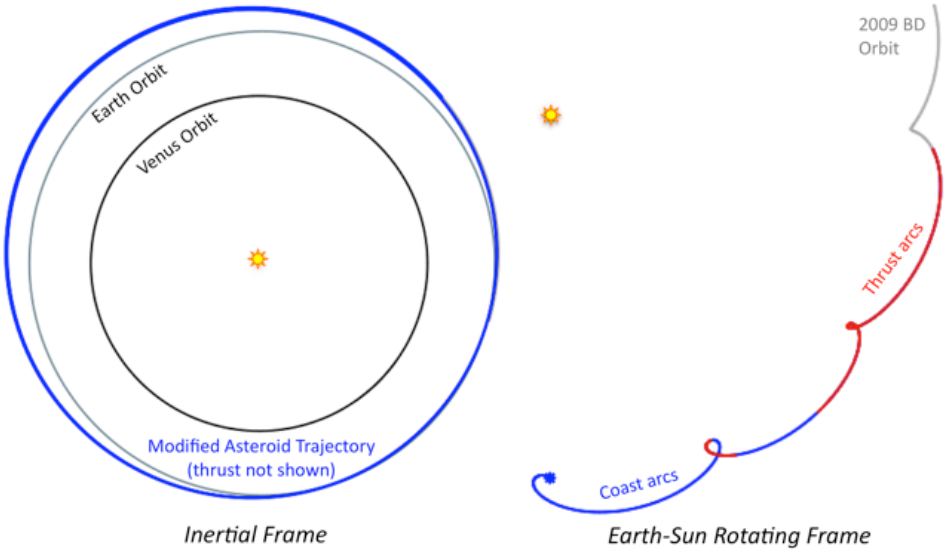

Figure 5.7: ARM "Fetch" leg

5.3 Asteroid Heliocentric Redirection

Asteroids that have a v_∞ too high to be captured with an LGA can still be redirected onto gravity-assist tours using Earth or other planets. Such tours could move the asteroids into orbits resonant with Earth that regularly return to Earth, allowing the opportunity for multiple crew missions. They could also move asteroids onto Earth-Mars cycler [56] orbits (discussed below) where the asteroidal material could be used for radiation shielding on cycler habitats. Asteroids could even be placed onto trajectories to the outer solar system. Because there are so many asteroids, if there is a ballistic gravity-assist trajectory valid for a spacecraft, chances are that an asteroid could be found with the right v_∞ to redirect onto that trajectory.

5.3.1 Earth Resonant and Backflip Orbits

A useful place to redirect an asteroid is an Earth resonant orbit (i.e. an orbit whose period is some rational number multiple of the Earth's). Such orbits would allow regular access to the asteroid for both crew visits and resource extraction. However, purely resonant orbits require missions at least a year long to visit. The backflip orbit is a half resonant orbit that would encounter the Earth at 6 month intervals, making it an especially attractive destination for redirection. Although resonant orbits can generally be achieved with one flyby, backflip orbits may require multiple flybys to set up depending on the asteroid's natural orbit. An asteroid could be placed in either a resonant or backflip orbit temporarily and then redirected onto another orbit. Such a scenario would allow a 6 month crew mission to an asteroid that could process the asteroid into radiation shielding or propellant before redirection of the processed material onto another trajectory such as a cycler.

5.3.2 Mars Cyclers

Earth-Mars cycler trajectories are repeating sequences of Earth and Mars flybys where an interplanetary transfer vehicle does not stop at Earth or Mars. [56, 57] To get to Mars on a cycler, the crew would fly in a small taxi vehicle to the cycler, ride it to Mars and then take the taxi from the cycler to Mars. To get home the crew would take their taxi from Mars to the cycler and then from the cycler to Earth. In general, one cycler would be used to get to Mars and another for the return trip. There are different families of cycler trajectories requiring differing ΔV to maintain the cycler, taxi ΔV , and number of cycler vehicles to cover all Mars opportunities. One interesting cycler is the S1L1 cycler. [57] This cycler is a repeating sequence of Earth-Earth-Mars flybys that is nearly ballistic and requires 4 cyclers to cover all Mars opportunities (and 2 vehicles if every other opportunity is skipped).

Over 400 asteroids approach Earth in the 2020s with the right v_∞ range to potentially be redirected onto a cycler. Table 5.2 presents a small subset of these with a v_∞ near 4 km/s, which could allow them to be redirected onto an S1L1 cycler in the 2030s. This table provides a crude, not optamized, estimate of the impulsive ΔV that would be needed to target the first flyby of the redirection sequence.

Table 5.2: Some Candidate Asteroids for Mars Cycler Redirection

Asteroid	Absolute Magnitude	Diameter Est. [m]	Mass Est. [t]	Natural Flyby Date	v_∞ [km/s]	ΔV Est. [m/s]
2013 UX2	29.2	3-14	29-2600	Oct. 2026	3.68	99
2008 LD	29.8	3-16	44-4000	Jun. 2035	4.13	36
2010 UY7	28.5	4-19	77-6900	Oct. 2027	3.96	136
2011 CL50	27.6	6-28	270-24,000	Feb. 2031	3.59	90
2006 UQ216	27.3	7-33	400-36,000	Nov. 2028	3.79	89
2009 HD	27.2	8-34	470-42,000	Oct. 2028	4.01	128
2011 HG2	27.0	8-37	610-55,000	Feb. 2025	3.36	39
2011 PB50	24.9	22-98	11,000-1e6	Feb. 2025	4.02	121
2003 LN6	24.7	24-108	110-1.3e6	Apr. 2026	3.98	66

Figure 5.8 presents an example redirection trajectory for asteroid 2013 UX2 from Table 5.2. This example shows that 2013 UX2's orbit is conducive to redirection to meet up with an S1L1 cycler on Nov. 15, 2031, but further characterization of 2013 UX2 would be needed to reduce its mass uncertainty before we know if it could be redirected by an ARM-like vehicle.

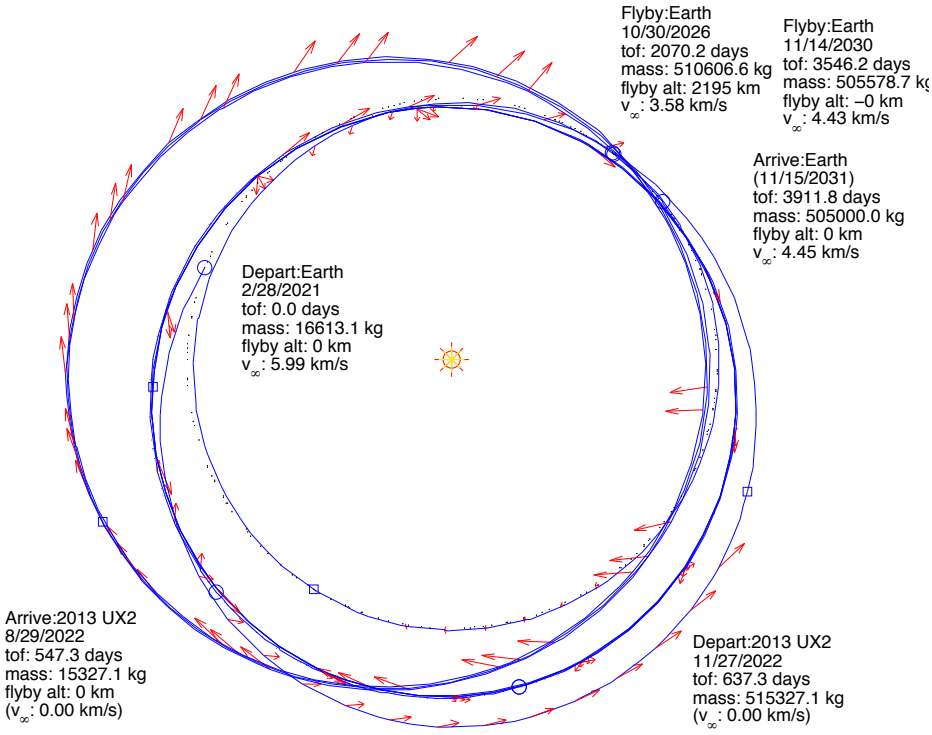

Figure 5.8: Example redirection of 2013 UX2 onto S1L1 cycler

CHAPTER 6. URANUS TOUR DESIGN

The 2013-2023 Planetary Science Decadal Survey [58] has identified a Uranus orbiter with atmospheric probes mission as a high-priority candidate for an outer planet flagship mission. Both Uranus and Neptune are Ice Giants and have different composition and atmospheric dynamics from Jupiter and Saturn. Uranus, being closer, is slightly easier to reach than Neptune [59]. In addition, unlike Neptune, Uranus is believed to still possess the satellites that formed with it. This could provide an opportunity to test hypotheses about the Uranian portion of the solar system nebula by observing these moons.

Past work by Heaton and Longuski [60] has shown that a Galileo-like multiple moon gravity-assist tour is possible at Uranus, provided the v_∞ with respect to the Uranian moons is sufficiently small. Since Uranus has a very high obliquity (97.77°), missions that do not arrive near the equinox (which occurs every 42 years and the next equinox is in 2049), will have very high approach declinations relative to the Uranian equator. This then leads to highly inclined ($60° - 80°$) initial capture orbits. This high inclination causes tours to begin with high v_∞ relative to the satellites (5–8 km/s), which is not conducive to the types of tours proposed by Heaton and Longuski. Because of this, the mission study conducted for the Decadal Survey was not able to achieve any significant orbit shaping with gravity-assists of the Uranian Satellites [61].

This chapter will focus on the design of the initial inclination reduction sequences needed to set up an equatorial multiple satellite Uranian tour. It will not address other aspects of potential Uranian mission designs such as the delivery of atmospheric probes and the design of a science tour of the Uranian satellites. Although this chapter focuses on Uranian missions, the techniques described here are valid in general and

could be used for other missions to design inclination modification sequences using a combination of maneuvers and gravity assists.

6.1 Inclination Reduction with Both Maneuvers and Flybys

Satellite tours such as those flown by Galileo and Cassini typically start with an orbit insertion maneuver and a periapsis raise maneuver that will together target a v_∞ at a moon. We may use this same approach at Uranus. Flybys of the targeted moon will then be used to lower the inclination of the orbit into the plane of the other Uranian satellites so that a gravity-assist tour is then possible. This section will develop the method for analyzing both the initial orbit and the inclination reduction flybys.

6.1.1 Twist and Incline Angles

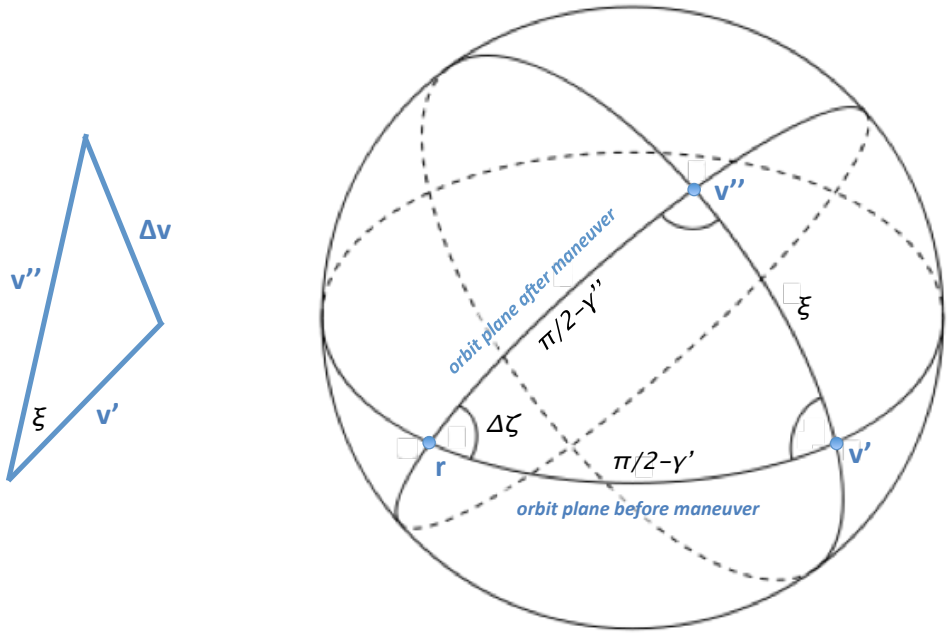

Figure 6.1: Maneuver planar triangle (left) and spherical triangle (right)

Figure 6.1 shows two constructions for determining the ΔV of a maneuver. On the left is a planar triangle showing how the addition of the $\Delta\vec{v}$ vector to the velocity before the maneuver ($\vec{v}\,'$) yields the velocity after the maneuver ($\vec{v}\,''$). The law of cosines applied to this triangle yields the following relation:

$$\Delta v^2 = v'^2 + v''^2 - 2v'v'' \cos(\xi) \tag{6.1}$$

where ξ is the maneuver *twist* angle. In the case of a maneuver at apoapsis, ξ is exactly the apo-twist angle [30–32].

But how does one find this angle or even identify the plane that this triangle is in? To answer these questions we use the right side of Fig. 6.1, which shows a spherical triangle constructed from the orbit planes before and after the maneuver. Both planes contain the radius vector at the time of the maneuver, and the angle between the planes is $\Delta\zeta$. The angle in each plane between a velocity vector and the radius vector is the compliment of the flight path angle (γ). The spherical law of cosines then yields the following relation for ξ:

$$\cos(\xi) = \sin(\gamma')\sin(\gamma'') + \cos(\gamma')\cos(\gamma'')\cos(\Delta\zeta) \tag{6.2}$$

We will call ζ the *incline* angle at the maneuver location, and it is found from the spherical right triangles in Fig. 6.2. In this figure, the orbit plane is the hypotenuse of the right spherical triangle and the base is a reference plane for the coordinates (e.g. the planet equator). Here, ϕ is the latitude of the maneuver location, λ the longitude, and f the true anomaly. The orbit parameters in the figure are inclination (i_{sc}), argument of periapsis (ω_{sc}), and the node angle (Ω_{sc}). The bottom of the figure shows Napier's Circles [62] for each triangle. These circles, which are a mnemonic for Napier's Rules, have the two angles next to the right angle of the triangle and the compliments of the other angles, listed in their order around the right spherical triangle. The sine of any angle in the circle is equal to the product of the two angles

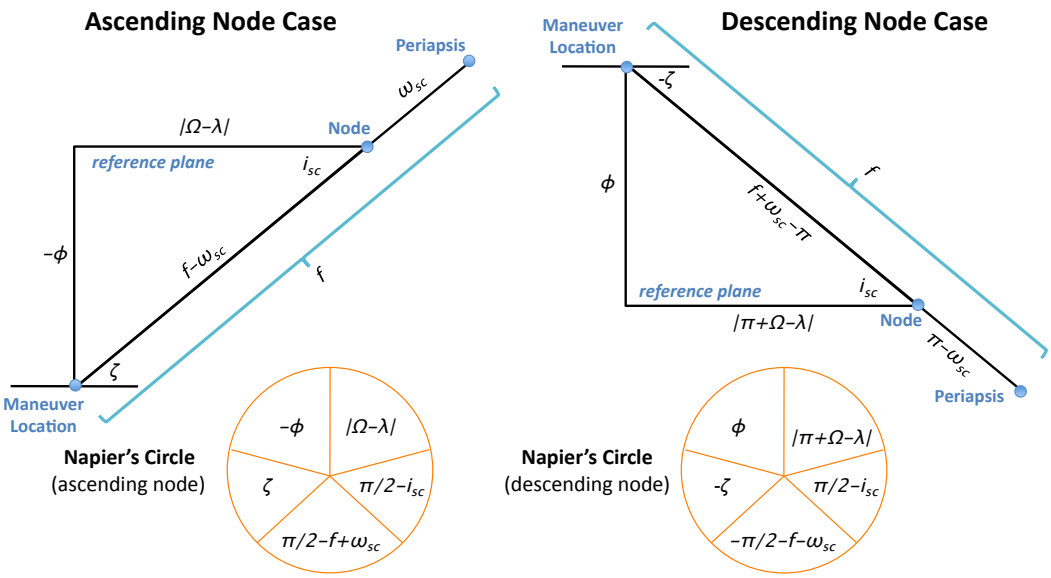

Figure 6.2: Spherical right triangles for determining incline angle (ζ)

next to it or the cosines of the two angles opposite to it. Napier's rules give us the following useful relation for the latitude of a maneuver before the ascending node:

$$\sin(\phi) = -\sin(i_{sc})\sin(f - \omega_{sc}) \tag{6.3}$$

and for before the descending node:

$$\sin(\phi) = -\sin(i_{sc})\sin(f + \omega_{sc}) \tag{6.4}$$

The inclination in both cases is:

$$\cos(i_{sc}) = \cos(\phi)\cos(\zeta) \tag{6.5}$$

When the maneuver is at the node crossing the incline angle is the orbit inclination ($\zeta_{node} = i_{sc}$), and on the hyperbolic asymptote the incline angle is the B-Plane angle ($\zeta_{\infty} = \theta_{fb}$).

Location of Inclination Change Maneuvers

Equation 6.5 tells us that a maneuver cannot reduce the inclination below the latitude of the maneuver location (i.e. the $\zeta = 0$ case). And if we recall that flight path angle is given from orbital angular momentum by:

$$\cos(\gamma) = \frac{h}{rv} = \frac{1}{rv}\sqrt{\mu_{cb} a_{sc}(1 - e_{sc}^2)} \tag{6.6}$$

and we combine this with Eqn. 6.1 and Eqn. 6.2, we get:

$$\Delta v^2 = v'^2 + v''^2 - \frac{2}{r^2}\cos(\Delta\zeta)\left(\sqrt{r^2 v'^2 - h'^2}\sqrt{r^2 v''^2 - h''^2} + h'h''\right) \tag{6.7}$$

Since v' and v'' decrease as r increases, Eqn. 6.7 tells us the the ΔV for a given change in incline ($\Delta\zeta$) decreases as radius increases. For these reasons, we would like to pick our maneuver location for an inclination change at the maximum radius in the orbit where the latitude is less than or equal to the new inclination.

Arrival Conditions

Equation 6.5 also tells us that the declination of the spacecraft hyperbolic asymptote (ϕ_∞) on approach to Uranus sets the minimum inclination of the arrival hyperbola. This inclination can be achieved by targeting a B-Plane angle (θ_{fb}) of 0°, and an inclination of 90° can be achieved with a θ_{fb} of ±90°. Equation 6.3 and Eqn. 6.4 allow us to calculate the argument of periapsis ω_{sc} which will be needed to check to see if the spacecraft is passing through a Uranian ring. To do this we will need f_∞, the true anomaly of the hyperbola's asymptote, which is a function of the Uranus periapsis distance (r_p) targeted for orbit insertion:[1]

$$\cos(f_\infty) = -\frac{1}{e_{sc}} = \frac{-\mu_{cb}}{\mu_{cb} - r_p v_i^2} \tag{6.8}$$

[1]Equation 6.8 is derived later in this chapter.

Here μ_{cb} is the central body's GM, and v_i is the magnitude of the incoming v_∞ vector.

If we chose the reference plane for orbit inclination to be the Uranian ring plane, the ring plane crossing will always be on the line of nodes of the spacecraft's orbit. We may then check the radius at the node crossing to determine if the spacecraft crosses within a ring or not. The argument of periapsis (ω_{sc}) is defined as the angle from the ascending node to periapsis. The angle from the descending node to periapsis is then $\pi - \omega_{sc}$. If we substitute these values for f_{node} into the conic equation, setting $r = r_{node}$:

$$r_{node} = \frac{a_{sc}(1 - e_{sc}^2)}{1 \pm e_{sc}\cos(\omega_{sc})} \tag{6.9}$$

we may then write ω_{sc} as the following:

$$\begin{aligned} &\text{if at ascending node (i.e., } i_{sc} \geq 0\text{):} \\ &\cos(\omega_{sc}) = \frac{1}{e_{sc}}\left[\frac{a_{sc}}{r_{enc}}(1 - e_{sc}^2) - 1\right] \end{aligned} \tag{6.10}$$

$$\begin{aligned} &\text{if at descending node (i.e., } i_{sc} < 0\text{):} \\ &\cos(\omega_{sc}) = \frac{1}{e_{sc}}\left[1 - \frac{a_{sc}}{r_{enc}}(1 - e_{sc}^2)\right] \end{aligned} \tag{6.11}$$

This gives us $\cos(\omega_{sc})$, but not the sign of ω_{sc}. To resolve this quadrant ambiguity, we note that the sign of ω_{sc} depends of whether the node crossing is inbound (i.e. before periapsis) or outbound (i.e. after periapsis):

$$\text{sign}(\omega_{sc}) = \begin{cases} 1 & \text{if crossing inbound} \\ -1 & \text{if crossing outbound} \end{cases} \tag{6.12}$$

We will check the inbound crossing of the hyperbola before orbit insertion and the outbound crossing of the initial capture orbit.

6.1.2 Finding Inclination Reduction Sequences

To find an inclination reduction sequence, it is most convienant to begin the analysis in the middle at the first flyby and then work our way out. Equation 2.65 allows us to assume a v_∞ for that flyby and an orbit period before that flyby and derive the inclination needed. We can then work backwards to an assumed periapsis raise maneuver location and orbit period and inclination before that maneuver, and again back from there to an assumed orbit insertion maneuver location and B-plane angle for the incoming hyperbola. For a given target moon and v_∞, we can optimize the free parameters subject to the node crossing constraints to find the lowest ΔV solution. For the example mission in the following section, this was done using MATLAB's *fmincon* function (a non-linear, constrained optimization solver).

The inclination reduction sequence cannot change the v_∞ with respect to the flyby moon without the addition of v_∞ leveraging maneuvers or backflip transfers with other moons. In this analysis, we will neglect those cases and assume the v_∞ is constant. This means that as inclination is reduced, the eccentricity will increase (by Eqn. 2.65) and the periapsis will decrease. Placing periapsis at the outer edge of the ring system then provides a lower bound on orbit period. We will target the minimum integer resonance (i.e. 1:1, 2:1, 3:1, etc.) that avoids the rings. Until that period is achieved, the flybys will pump down to the lowest integer resonance achievable and use any excess bending to reduce crank. After we reach that period, flybys will reduce crank until inclination is zero.

6.2 Example Uranus Tour Design

As an example application of the techniques developed in the previous section, this section will develop a ΔV estimate for an inclination reduction sequence starting from the interplanetary trajectory in Fig. 6.3. This is a 13-year ΔV-EGA with a Saturn flyby launching in 2025. It arrives with a v_∞ of 6.5 km/s and a declination of 75.6°. The goal will be to find a 1-year reduction sequence, which would then

leave us enough time for a 2-year planar tour in a 15-year mission. We will limit the Uranian periapsis altitude to no lower than 5,000 km and the ring plane crossing to no lower than 51,140 km to avoid the rings. In this example, the first Uranian moon flyby will be 200 km and subsequent flybys will limited to 50 km or higher.

6.2.1 Tisserand Graph for Uranian Satellites

Figure 6.4 shows a $r_a - r_p$ Tisserand Graph [18,37] for Oberon (black) and Titania (blue) for 0 inclination. The solid lines are contours of constant v_∞ and the dashed lines are the integer resonances with each satellite. The red horizontal line denotes cases where the orbit periapsis is below the outer extent of the rings. The v_∞ contours have tick marks denoting the spacing between 50 km flybys of each moon.

We see that a Titania 3:1 resonance (26 days) is very close to an Oberon 2:1 resonance (27 days). To avoid the rings at this resonance we need a v_∞ of 4.5 km/s or less at Titania or a v_∞ of less than about 3.9 km/s at Oberon. A v_∞ of 2 km/s is the lowest v_∞ at either body to allow periapses near the rings.

6.2.2 ΔV and Flight Time

Figure 6.5 shows the optimal ΔV required to target various v_∞ values from the given arrival conditions. Figure 6.6 then shows the flight time of the inclination reduction sequences for each v_∞ (including the initial Uranian orbit). We see that to achieve a 1-year inclination reduction sequence, we would need a v_∞ of about 2.2 km/s at Titania or about 2 km/s at Oberon. This corresponds to an initial orbit ΔV of 1.86 km/s for Titania and 1.9 km/s for Oberon.

6.3 Relevance of Results

This chapter developed a parameterization of maneuvers in terms of twist (ξ) and incline (ζ) angles that is convenient for designing maneuvers that change inclina-

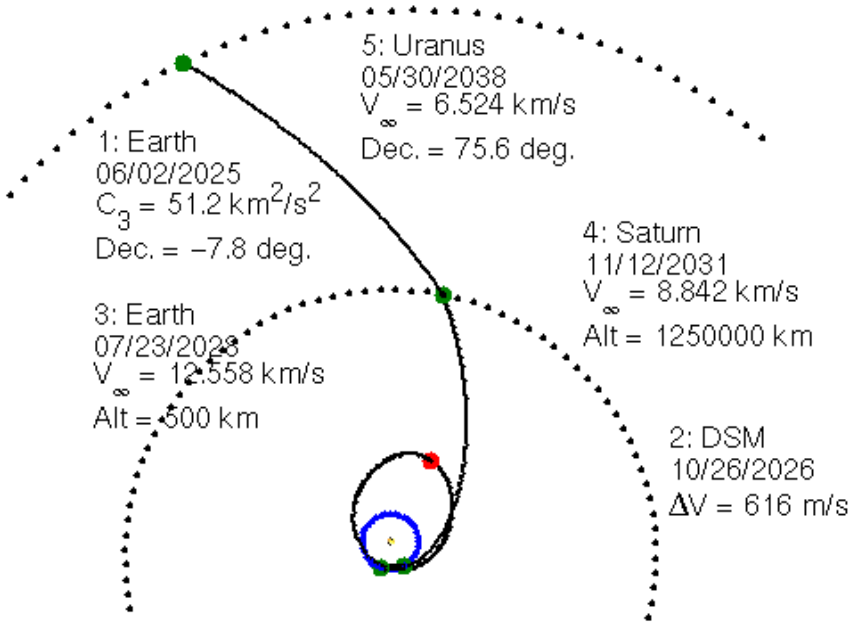

Figure 6.3: Example 2025 EESU trajectory

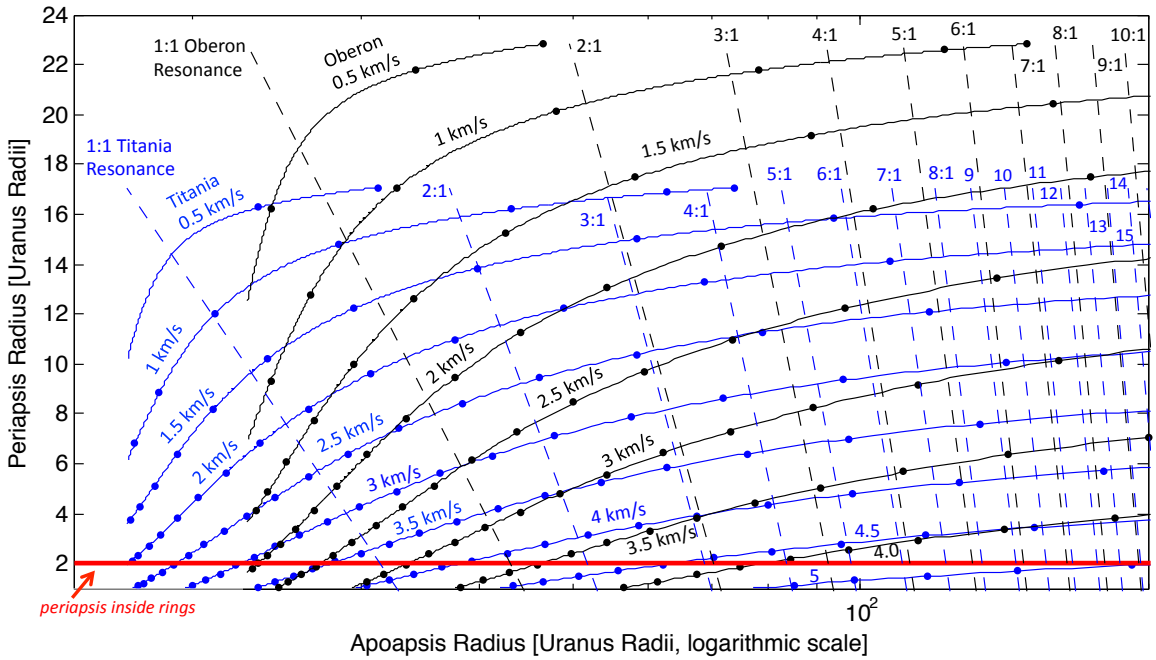

Figure 6.4: Tisserand Graph for Oberon and Titania

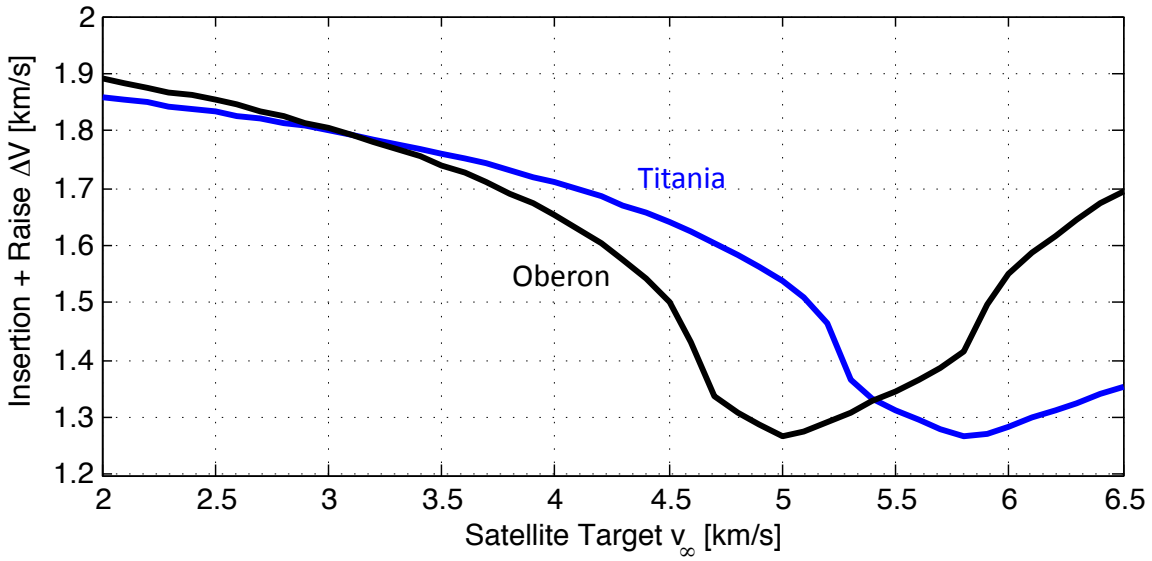

Figure 6.5: Oberon and Titania v_∞ vs. ΔV

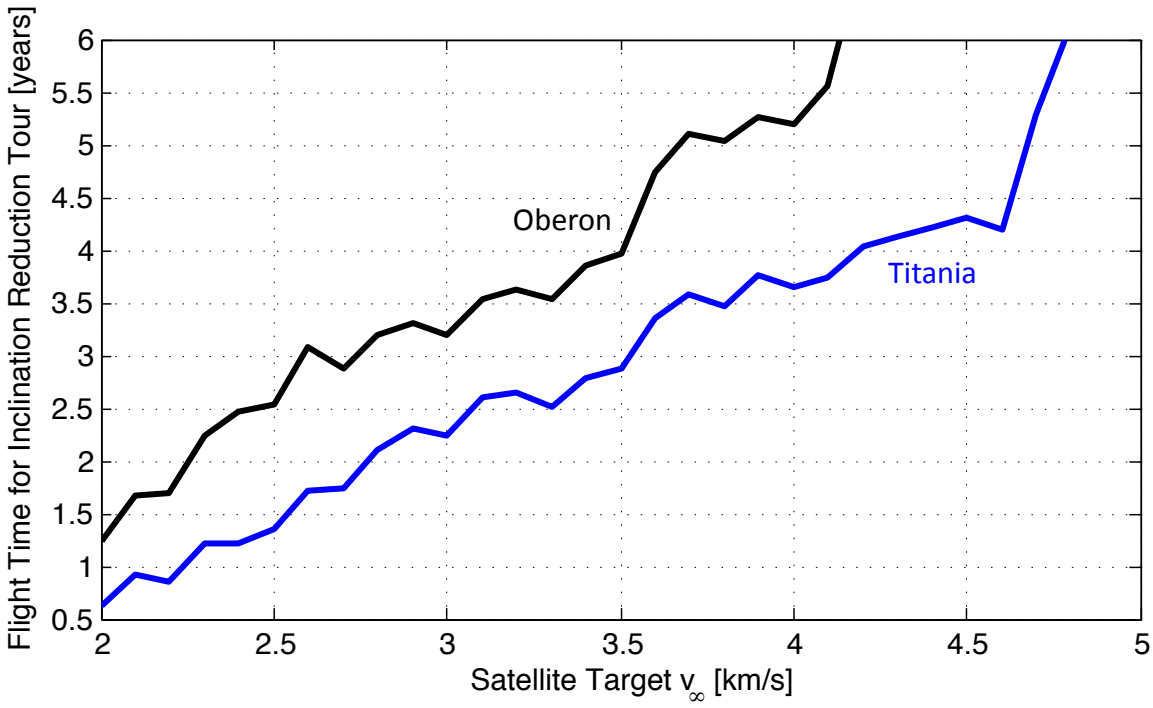

Figure 6.6: Oberon and Titania v_∞ vs. flight time

tion or argument of periapsis. This combined with known relations between v_∞ and Tisserand's Criterion and for pump and crank in Chapter 2, enables the analysis of initial inclination reduction sequences for gravity-assist tours with algebraic relations. Although this chapter focuses on Uranian missions, the techniques described in this chapter are valid in general and could be used for other missions to design inclination modification sequences using a combination of maneuvers and gravity assists.

CHAPTER 7. SUMMARY

7.1 Mission Applications

The techniques in Chapters 2 and 3 were used to develop both the Cassini Equinox [63] and Solstice [64] extended missions. Tisserand Graphs from Chapter 3 and the Leveraging techniques in Chapter 4 have been use for tour designs for the NASA Europa Orbiter [20,36,65], NASA Europa Clipper [66], NASA Europa Lander [65,67], NASA Jupiter System Observer [68], NASA Titan Saturn System Mission [38], NASA Asteroid Redirect Mission [41], ESA JUpiter ICy moon Explorer (JUICE) [69], and JAXA Jupiter Magnetospheric Orbiter [70] mission concepts.

7.2 Topics for Future Work

Different-Body Transfers

Tisserand Graphs only provide a phase-free method for designing different-body transfers. I suspect that it should be possible to modify the algorithm for finding same-body non-resonant transfers in § 3.1.2 to find different-body transfer as a function of the angle between the positions of the two bodies at the start of the transfer. Such a method should be possible without solving Lambert's problem.

Non-Leveraging Impulsive Transfers

Leveraging transfers are only one possible way to used impulsive ΔV in concert with gravity assists. What about using ΔV to focus on changing pump or crank instead of v_∞ magnitude?

Low-Thrust V-Infinity Leveraging

Low-thrust transfers add a great deal more flexibility than the impulsive transfers studied in Chapter 4. This opens up both the potential for greater design freedom and the problem of many more degrees of freedom to consider in analysis.

Low-Energy Gravity-Assist Transfers

Patched conics are not sufficient for designing gravity-assist trajectories in the Earth-Moon system. Trajectories with low Lunar v_∞ are heavily perturbed by the Moon, and trajectories with high Lunar v_∞ are heavily perturbed by the Sun. An approach that uses Lunar flybys as patch-points between CR3BP orbits rather than Keplerian orbits has already been shown to yield interesting resultsby Gregory Lantoine [54], and I think there is still a lot more to do in this area.

7.3 Conclusion

Figure 7.1 shows my first attempt at understanding the three-dimensional version of the v-infinity triangle (Fig. 2.1). My utter confusion in staring at Fig. 7.1 eventually

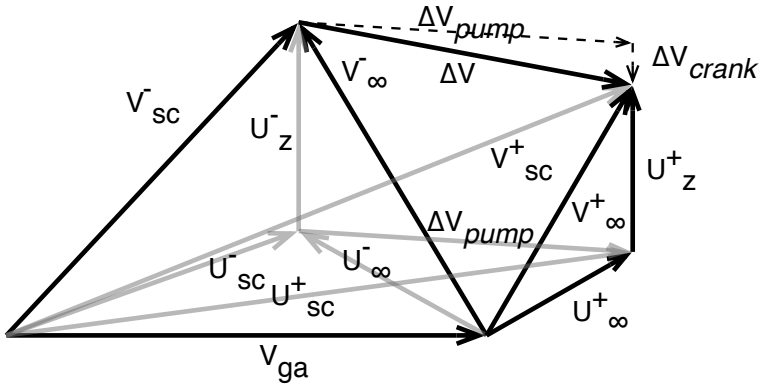

Figure 7.1: A confusing gravity-assist vector diagram

led me to spherical coordinates, spherical trigonometry, the results in Chapter 2, and eventually much of the rest of this dissertation.

I hope that this dissertaion has demonstrated how algebra, vector analysis, and even spherical trigonometry can still be useful for spaceflight – even in world where powerful computers are ubiquitous. The techniques in this dissertation have allowed me to handcraft gravity-assist tours that do what I want instead of just waiting to see what a month-long computer run spits out. This has made the tour design problem a lot less confusing and a lot more fun.

REFERENCES

REFERENCES

[1] R.H. Battin. *An Introduction to the Mathematics and Methods of Astrodynamics*, pages 423–424. AIAA Press, Reston, Va., revised edition, 1999.

[2] R.A. Brouke. On the History of the Slingshot Effect and Cometary Orbits. *AAS/AIAA Astrodynamics Specialist Conference*, July–Aug. 2001. AAS Paper 01-435.

[3] F.F. Tisserand. *Traite de Mechanique Celeste*, volume 4. Gauthier-Villars et Fils, 1896.

[4] K.A. Ehricke. *Space Flight: II – Dynamics*. van Nostrand, 1962.

[5] M.A. Minovitch. The Determination and Characteristics of Ballistic Interplanetary Trajectories under the Influence of Multiple Planetary Attractions. *JPL TR 32-464*, Oct. 1963.

[6] G.A. Flandro. Fast Reconnaissance Missions to the Outer Solar System Utilizing Energy Derived from the Gravitational Field of Jupiter. *Acta Astronautica*, 12(4):329–327, July–Aug. 1966.

[7] J.C. Beckman, J.R. Hyde, and S. Rasool. Exploring Jupiter and Its Satellites with an Orbiter. *Aeronautics and Astronautics*, 12:24–35, Sept. 1974.

[8] C. Uphoff, P.H. Roberts, and L.D. Friedman. Orbit Design Concepts for Jupiter Orbiter Missions. *Journal of Spacecraft and Rockets*, 13(6):348–355, June 1976.

[9] A.A. Wolf and J.C. Smith. Design of the Cassini Tour Trajectory in the Saturnian System. *Journal of the International Federation of Automatic Control*, 3(11):1611–1619, Oct. 1995.

[10] J.C. Smith. Description of Three Candidate Cassini Satellite Tours. *AAS Spaceflight Mechanics Meeting*, Feb. 1998. Paper AAS 98-106.

[11] S.N. Williams. Automated Design of Multiple Encounter Gravity-Assist Trajectories. Master's thesis, School of Aeronautics & Astronautics, Purdue University, West Lafayette, IN, Aug. 1990.

[12] S.N. Williams and J.M. Longuski. Automated Design of Multiple Encounter Gravity-Assist Trajectories. *AIAA/AAS Astrodynamics Conference*, Aug. 1990. AIAA Paper 90-2982.

[13] J.M. Longuski and S.N. Williams. Automated Design of Gravity-Assist Trajectories to Mars and the Outer Planets. *Celestial Mechanics and Dynamical Astronomy*, 52(3):207–220, 1991.

[14] J.A. Sims, J.M. Longuski, and A.J. Staugler. V_∞ Leveraging for Interplanetary Missions: Multiple-Revolution Orbit Techniques. *Journal of Guidance, Control, and Dynamics*, 20(3):409–415, May 1997.

[15] N.J. Strange and J.A. Sims. Methods for the Design of V-Infinity Leveraging Maneuvers. *AAS/AIAA Astrodynamics Specialist Conference*, Aug. 2001. Paper AAS 01-437.

[16] N.J. Strange. Pumping, Cranking, and Bending: The Theory Behind the Galileo and Cassini Tours. JPL Numerical Algorithms Seminar, March 2006.

[17] N.J. Strange. Control of Node Crossings in Saturnian Gravity-Assist Tours. *AAS/AIAA Astrodynamics Specialist Conference*, Aug. 2003. Paper AAS 03-545.

[18] N.J. Strange and J.M. Longuski. Graphical Method for Gravity-Assist Trajectory Design. *Journal of Spacecraft and Rockets*, 39(1):9–16, 2002.

[19] A.V. Labunsky, O.V. Papkov, and K.G. Sukhanov. *Multiple gravity assist interplanetary trajectories*, pages 33–54. CRC Press, 1998.

[20] A. Heaton, N.J. Strange, J.M. Longuski, and E.B. Bonfiglio. Automated Design of the Europa Orbiter Tour. *Journal of Spacecraft and Rockets*, 39(1):17–22, 2002.

[21] N.J. Strange, R.P. Russell, and B.B. Buffington. Mapping the V-Infinity Globe. *AAS/AIAA Astrodynamics Specialist Conference*, Aug. 2007. Paper AAS-07-277.

[22] G. Hollenbeck. New Flight Techniques for Outer Planet Missions. *AAS/AIAA Astrodynamics Specialist Conference*, July 1975. Paper AAS 75-087.

[23] A.T. Brinckerhoff and R.P. Russell. Pathfinding and V-Infinity Leveraging for Planetary Moon Tour Missions. *AAS Space Flight Mechanics Meeting*, Feb. 2009. Paper AAS 09-222.

[24] S. Campagnola and R.P. Russell. Endgame Problem Part 1: V-Infinity-Leveraging Technique and the Leveraging Graph. *Journal of Guidance, Control, and Dynamics*, 33(2):463–475, March 2010.

[25] N.J. Strange, S. Campagnola, and R.P. Russell. Leveraging Flybys of Low Mass Moons to Enable an Enceladus Orbiter. *AAS/AIAA Astrodynamics Specialist Conference*, Aug. 2009. Paper AAS 09-435.

[26] J.R. Brophy et al. Asteroid Retrieval Feasibility Study. Keck Institute for Space Studies Final Report, 2011. `http://www.kiss.caltech.edu/study/asteroid/asteroid_final_report.pdf`.

[27] J.R. Brophy, L. Friedman, and F. Culick. Asteroid Retrieval Feasibility. In *Aerospace Conference, 2012 IEEE*, March 2012.

[28] N.J. Strange, D.F. Landau, J.M. Longuski, and P. Chodas. Identification of Retrievable Asteroids with the Tisserand Criterion. *AIAA/AAS Astrodynamics Specialist Conference*, Aug. 2014. Paper AIAA 2014-4458.

[29] N.J. Strange, D.F. Landau, J.M. Longuski, and P. Chodas. Redirection of Asteroids onto Earth-Mars Cyclers. *AAS Spaceflight Mechanics Meeting*, Jan. 2015. Paper AAS 15-462.

[30] R.F. Luidens and B.A. Miller. Efficient Planetary Parking Orbits with Examples for Mars. *NASA TN D-3220*, Jan. 1966.

[31] J.M. Deerwester, J.F. McLaughlin, and J.F. Wolfe. Earth-Departure Plane Change and Launch Window Considerations for Interplanetary Missions. *Journal of Spacecraft*, 3(2):169–174, 1966.

[32] D.F. Landau, J.M. Longuski, and P.A. Penzo. Method for Parking-Orbit Reorientation for Human Missions to Mars. *Journal of Spacecraft and Rockets*, 42(3):517–522, 2005.

[33] N.J. Strange, D.F. Landau, J.M. Longuski, and P. Chodas. Design of Initial Inclination Reduction Sequence for Uranian Gravity-Assist Tours. *AAS/AIAA Astrodynamics Specialist Conference*, Aug. 2013. Paper AAS 13-801.

[34] B.B. Buffington and N.J. Strange. Science-Driven Design of Enceladus Flyby Geometry. *International Astronautical Congress*, Oct. 2006. Paper IAC-06-C1.6.05.

[35] W. Kizner. A Method of Describing Miss Distance for Lunar and Interplanetary Trajectories. External Publication No. 674, Jet Propulsion Laboratory, California Institute of Technology, 1969.

[36] K.W. Kloster, A.E. Petropoulos, and J.M. Longuski. Europa Orbiter Tour Design with Io Gravity Assists. *Acta Astronautica*, 68(7):931–946, 2011.

[37] S. Campagnola and R.P. Russell. The Endgame Problem Part 2: The Multi-Body Technique and the T-P Graph. *Journal of Guidance, Control and Dynamics*, 33(2):476–486, 2010.

[38] N. Strange, T. Spilker, D. Landau, T. Lam, D. Lyons, and J. Guzman. Mission Design for the Titan Saturn System Mission Concept. *AAS/AIAA Astrodynamics Specialist Conference*, Aug. 2009. Paper AAS 09-356.

[39] S. Campagnola, N.J. Strange, and R.P. Russell. A Fast Tour Design Method Using Non-Tangent V-Infinity Leveraging Transfers. *Celestial Mechanics and Dynamical Astronomy*, 108(2):165–186, 2010.

[40] D. Landau, J. Dankanich, N. Strange, J. Bellerose, P. Llanos, and M. Tantardini. Trajectories to Nab a NEA (Near Earth Asteroid). *AAS Spaceflight Mechanics Meeting*, Feb. 2013. Paper AAS 13-409.

[41] N. Strange, D. Landau, T. McElrath, G. Lantoine, T. Lam, M. McGuire, L. Burke, M. Martini, and J. Dankanich. Overview of Mission Design for NASA Asteroid Redirect Robotic Mission Concept. *International Electric Propulsion Conference*, Oct. 2013. Paper IEPC-2013-321.

[42] D. Mazanek, R. Merrill, S. Belbin, D. Reeves, B. Naasz, P. Abell, and K. Earle. Asteroid Redirect Robotic Mission: Robotic Boulder Capture Option Overview. *AIAA SPACE Forum and Exposition*, Aug. 2014. Paper AIAA-2014-4432.

[43] G.K. O'Neill. The Colonoization of Space. *Physics Today*, 27(9):32–40, Sept. 1974.

[44] B.T. O'Leary. Mass Driver Retrieval of Earth-Approaching Aseroids. *Princeton/AIAA Conference on Space Manufacturing Facilities*, May 1977. Paper AIAA 77-528.

[45] B.T. O'Leary. Mining the Apollo and Amor Asteroids. *Science*, 197(4301):363–366, July 1977.

[46] B.T. O'Leary. Asteroid Prospecting and Retrieval. *Princeton/AIAA Conference on Space Manufacturing Facilities*, May 1979. Paper AIAA 79-1432.

[47] C.E. Singer. Collisional Orbital Change of Asteroid Materials. *Princeton/AIAA Conference on Space Manufacturing Facilities*, May 1979. Paper AIAA 79-1434.

[48] J. Pearson. Asteroid Retrieval by Rotary Rocket. *AIAA Aerospace Sciences Meeting*, Jan. 1980. Paper AIAA 80-0166.

[49] K.R. Erickson. Optimal Architecture for an Asteroid Mining Mission: Equipment Details and Integration. *AIAA SPACE Forum and Exposition*, Sept. 2006. Paper AIAA 2006-7504.

[50] N.J. Strange, R.G. Merrill, D.F. Landau, B.D. Drake, J.R. Brophy, and R.R. Hofer. Human Missions to Phobos and Deimos Using Combined Chemical and Solar Electric Propulsion. *AIAA/ASME/SAE/ASEE Joint Propulsion Conference & Exhibit*, July 2011. Paper AIAA 2011-5663.

[51] H.W. Price, R. Woolley, N.J. Strange, and J.D. Baker. Human Missions to Mars Orbit, Phobos, and Mars Surface Using 100-kWe-Class Solar Electric Propulsion. *AIAA SPACE 2014 Conference and Exposition*, Aug. 2014. Paper AIAA 2014-4436.

[52] C. Bombardelli and J. Peláez. Ion Beam Shepherd for Asteroid Deflection. *Journal of Guidance, Control, and Dynamics*, 34(4):1270–1272, 2011.

[53] P. Lubin, G.B. Hughes, J. Bible, J. Bublitz, J. Arriola, C. Motta, J. Suen, I. Johansson, J. Riley, N. Sarvian, et al. Toward Directed Energy Planetary Defense. *Optical Engineering*, 53(2):025103–025103, 2014.

[54] T.P. McElrath, G. Lantoine, D. Landau, D. Grebow, N. Strange, R. Wilson, and J. Sims. Using Gravity Assists in the Earth-Moon System as a Gateway to the Solar System. *Global Space Exploration Conference*, May 2012. Paper GLEX-2012.05.5.2x12358.

[55] M. Mommert, J.L. Hora, D. Farnocchia, S.R. Chesley, D. Vokrouhlickỳ, D.E. Trilling, M. Mueller, A.W. Harris, H.A. Smith, and G.G. Fazio. Constraining the Physical Properties of Near-Earth Object 2009 BD. *The Astrophysical Journal*, 786(2):148, 2014.

[56] D.V. Byrnes, J.M. Longuski, and B. Aldrin. Cycler Orbit Between Earth and Mars. *Journal of Spacecraft and Rockets*, 30(3):334–336, 1993.

[57] T.T. McConaghy, D.F. Landau, C.H. Yam, and J.M. Longuski. Notable Two-Synodic-Period Earth-Mars Cycler. *Journal of Spacecraft and Rockets*, 43(2):456–465, 2006.

[58] *Vision and Voyages for Planetary Science in the Decade 2013-2022*. National Academies Press, 2011.

[59] D.F. Landau, T. Lam, and N.J. Strange. Broad Search and Optimization of Solar Electric Propulsion Trajectories to Uranus and Neptune. *AAS/AIAA Astrodynamics Specialist Conference*, Aug. 2009. AAS Paper 09-428.

[60] A. Heaton and J.M. Longuski. Feasibility of a Galileo-Style Tour of the Uranian Satellites. *Journal of Spacecraft and Rockets*, 40(4):591–596, 2003.

[61] J. McAdams, C. Scott, Y. Guo, J. Dankanich, and R. Russell. Conceptual Mission Design of a Polar Uranus Orbiter and Satellite Tour. *Space Flight Mechanics Conference*, Feb. 2011. AAS Paper 11-188.

[62] N. Bowditch. *The American Practical Navigator*. National Imagery and Mapping Agency, Bethesda, MD., 2002 bicentennial edition, 2002.

[63] B. Buffington, N. Strange, and J. Smith. Overview of the Cassini Extended Mission Trajectory. *AIAA/AAS Astrodynamics Specialist Conference*, Aug. 2008. Paper AIAA 2008-6752.

[64] J. Smith and B. Buffington. Overview of the Cassini Solstice Mission Trajectory. *AAS/AIAA Astrodynamics Specialist Conference*, Aug. 2009. Paper AAS 09-351.

[65] S. Campagnola, B.B. Buffington, and A.E. Petropoulos. Jovian Tour Design for Orbiter and Lander Missions to Europa. *Acta Astronautica*, 100:68–81, 2014.

[66] Brent Buffington. Trajectory Design Concept for the Proposed Europa Clipper Mission. *AIAA/AAS Astrodynamics Specialist Conference*, Aug. 2014. Paper AIAA 2014-4105.

[67] T.P. McElrath, S. Campagnola, and N.J. Strange. Riding the Banzai Pipeline at Jupiter: Balancing Low Delta-V and Low Radiation to Reach Europa. *AIAA/AAS Astrodynamics Specialist Conference*, Aug. 2012. Paper AIAA 2012-4809.

[68] Jupiter System Observer Mission Study: Final Report. JPL D-41284, 2007. `http://www.lpi.usra.edu/opag/jso_final_report.pdf`.

[69] S. Campagnola, A. Boutonnet, J. Schoenmaekers, D. Grebow, A. Petropoulos, and R. Russell. Tisserand-Leveraging Transfers. *Journal of Guidance, Control, and Dynamics*, 37(4):1202–1210, March 2014.

[70] S. Campagnola and Y. Kawakatsu. Jupiter Magnetospheric Orbiter: Trajectory Design in the Jovian System. *Journal of Spacecraft and Rockets*, 49(2):318–324, March 2012.

VITA

VITA

Nathan Strange grew up exploring the wooded hills and hollows of Southern Indiana. His childhood love of exploration grew into an interest in spaceflight and a dream of someday working on robotic probes exploring the Solar System. Nathan began high school in the small town of Shoals, IN, but was accepted into the Indiana Academy for Science Mathematics & Humanities in Muncie, IN for his Junior and Senior years of high school.

After the graduating from the Academy in 1993, Nathan went to Purdue University where he earned B.S. degrees in both Physics and Aerospace Engineering in 1997 and an M.S. degree in Aerospace Engineering in 2000 with Prof. James Longuski as his advisor. After graduation, Nathan got his dream job at NASA's Jet Propulsion Laboratory (JPL). He began his career on the navigation team for the Cassini-Huygens mission to Saturn and was part of the task force that figured out how to recover the Huygens mission after a problem was found with its relay radio, ensuring that the probe successfully made the first-ever landing on Saturn's moon Titan.

In 2007, Nathan transitioned from the Cassini project to work on several mission studies and proposals. Most notably, Nathan was part of a Keck Institute for Space Studies (KISS) workshop that found it was possible to redirect a small asteroid into an orbit around the Moon using high power Solar Electric Propulsion (SEP). NASA was excited by this result and decided to implement the Asteroid Redirect Robotic Mission (ARRM) concept. Nathan now leads the ARRM Mission Design team. He also is part of NASA studies investigating mission architectures for affordable human Mars missions using the high-power SEP technologies that would be developed by ARRM. With luck (and Congressional approval), these studies could lead to human Mars missions in the 2030s.

Nathan began pursuing a Ph.D. in Aerospace Engineering remotely from Purdue University with Prof. Jim Longuski in 2009. In his career, Nathan has authored or co-authored over 40 conference papers and 8 journal articles and co-wrote an article for Scientific American ("This Way to Mars", Dec. 2011). He has received two NASA Exceptional Achievement Medals and JPL's Lew Allen award for his research in gravity-assist trajectory design.

On the way to all of his space adventures, Nathan met the love of his life the first weekend after he moved to Los Angeles, and together they have four children. Whenever the opportunity arises, the Strange Family likes to explore California and America's West on camping and road trip adventures.